Lehrstuhl für Umformtechnik und Gießereiwesen
Fakultät Maschinenwesen
Technische Universität München

TUM

Formability Consideration in Bead Optimization to stiffen Deep Drawn Parts

Wan-Gi Cha

Vollständiger Abdruck der von der Fakultät für Maschinenwesen
der Technischen Universität München zur Erlangung des akademischen
Grades eines Doktor-Ingenieurs (Dr.-Ing.) genehmigten Dissertation.

Vorsitzender:

>   *Prof. Dr.-Ing. Michael Zäh*

Prüfer der Dissertation:

>   1. *Prof. Dr.-Ing. Wolfram Volk*

>   2. *Prof. Dr.-Ing. Dr. h.c. Albert Albers*

Die Dissertation wurde am *14.01.2019* bei der Technischen
Universität München eingereicht und durch die Fakultät für
Maschinenwesen am *24.04.2019* angenommen.

Vorwort

Die vorliegende Arbeit entstand während meiner Tätigkeit als wissenschaftlicher Mitarbeiter am Lehrstuhl für Umformtechnik und Gießereiwesen (utg) der Technischen Universität München.

Mein besonderer Dank gilt meinem Doktorvater Herrn Prof. Dr.-Ing. Wolfram Volk, Ordinarius für Umformtechnik und Gießereiwesen der Technischen Universität München, für das mir entgegengebrachte Vertrauen und für die persönliche Förderung, für die stets wohlwollende Unterstützung bei der Durchführung dieser Arbeit.

Herrn Prof. Dr.-Ing. Albert Albers, Ordinarius für Produktentwicklung des Karlsruher Instituts für Technologie, danke ich für sein Interesse und für die Übernahme des Koreferats sowie Herrn Prof. Dr.-Ing. Michael Zäh, Ordinarius für Werkzeugmaschinen und Betriebswissenschaften der Technischen Universität München, für die Übernahme des Prüfungsvorsitzes.

Bei allen Mitarbeitern des Lehrstuhls bedanke ich mich für ihre freundliche, sprachliche und kulturelle sowie fachliche Unterstützung. Besonders bin ich Herrn Dr.-Ing. Roland Golle und Herrn Tobias Hammer, Christian Gaber, Matthias Eder, Maximilian Gruber, Simon Vitzthum, Hannes Weiss, Christoph Hartmann, Frau Annika Weinschenk zum Dank verpflichtet.

Diese Dissertation basiert auf Ergebnissen des öffentlich geförderten Projektes „Numerische Sickenoptimierung zur Versteifung bombierter Blechgeometrien unter Berücksichtigung des nichtlinearen Formänderungsvermögens mithilfe eines gekoppelten Algorithmus". Deutsche Forschungsgemeinschaft (DFG) sei für die finanzielle Unterstützung herzlich gedankt. Weiterhin bedanke ich mich bei meiner Projektpartnerin Frau Sabrina Müller vom Institut für Produktentwicklung des Karlsruher Instituts für Technologie für die angenehme Zusammenarbeit.

Mein ganz besonderer Dank gilt meiner Familie und meinen Freunden für ihren andauernden und bedingungslosen Rückhalt. Danken möchte ich vor allem meiner Ehefrau Yewon, die mich in jeder Weise unterstützt hat. Diese Arbeit widme ich meinen Eltern, die mir durch ihre uneingeschränkte Unterstützung und Förderung meinen beruflichen Werdegang ermöglicht haben.

München, im Januar 2019

Wan-Gi Cha

Abstract

This thesis deals with a formability consideration in the bead optimization. The formability should be analyzed by simulation techniques in order to connect it with the bead optimization procedure. The anisotropic material behavior and the nonlinear deformation history are considered since sheet metal parts usually undergo the deep drawing as a preforming and the bead forming as a subsequent forming during their manufacture. The advanced anisotropic yield function Yld2000-2d with the non-associated flow rule achieves accurate simulation of the anisotropic material behavior of the sheet metal. The forming limit prediction model named Generalized Forming Limit Concept (GFLC) also predicts the accurate forming limit under any loading changes. Based on that, the initial bead height can be suggested after the preforming. This can efficiently improve the design of the optimal bead geometries inconsideration of the manufacturability.

Kurzfassung

Diese Arbeit behandelt die Berücksichtigung der Herstellbarkeit bei der Sickenoptimierung. Die Herstellbarkeit sollte durch Simulationstechniken zur Verbindung mit dem Sickenoptimierungsablauf analysiert werden. Das anisotrope Werkstoffverhalten und die nichtlineare Verformungsgeschichte werden berücksichtigt, da Blechteile während ihrer Herstellung einen Tiefziehprozess als Vorformung und einer Sickenformung als Nachformung durchlaufen. Die fortgeschrittene anisotrope Fließfunktion Yld2000-2d mit der nicht-assoziierten Fließregel ermöglicht die akkurate Simulation des anisotropen Werkstoffverhaltens der Blechteile. Das Vorhersagensmodell für die Umformgrenze namens Generalized Forming Limit Concept (GFLC) prognostiziertauch die genaue Umformgrenze unter jeder Belastungsänderung. Basierend darauf kann die anfängliche Sickenhöhe nach der Vorformung vorgeschlagen werden. Hierdurch kann die optimale Sickengeometrie unter der Berücksichtigung der Herstellbarkeit effizienter gestaltet werden.

Contents

List of symbols

Symbols	Unit	Meaning
$\ddot{\mathbf{u}}$	mm	Acceleration vector
θ	°	Angle
a_s	°	Angle of bead geometry
$\bar{\varepsilon}$	-	Effective strain
F, G, H, L, M, and N	-	Anisotropic parameter for Hill48
$\mathbf{L}'$ and $\mathbf{L}''$	-	Anisotropic parameter vectors for Yld2000-2d
$\tilde{\mathbf{u}}$	mm	Approximate displacement vector
I	mm^4	Area moment of inertia
A_l	mm^2	Area of upper bead
A_l	mm^2	Area of lower bead
$\mathbf{q}$	N/mm^2	Back stress vector
c, d, h, p, and M	-	Barlat89 parameter
f_{B89}	N/mm^2	Barlat89 yield function
φ	-	Bead rate
$\mathbf{f}_{body}$	N	Body force vector
$\mathbf{b}$	N/mm^3	Body force vector per volume
$\partial\Omega$	-	Boundary of domain
$\partial\Omega_u$	-	Boundary of domain for Dirichlet
$\partial\Omega_t$	-	Boundary of domain for Neumann
$\boldsymbol{\sigma}$	N/mm^2	Cauchy stress tensor
r_b	-	Coefficient of biaxial anisotropy
f_{nh}	-	Coefficient of geometrical non-homogeneity
s_{ij}	N/mm^2	Components of deviatoric stress tensor
$\mathbf{u}_0$	mm	Constant displacement vector
λ_{cor}	-	Corrected strain path length ratio
Δt_{krit}	sec	Critical time increment
$(n+1)$	-	Current state
$\mathbf{B}$	1/mm	Displacement differentiation matrix

Symbols	Unit	Meaning
$\mathbf{u}$	mm	Displacement vector
e_1	mm	Distance of gravity line from upper width
e_2	mm	Distance of gravity line from lower width
e_3	mm	Distance of gravity line from middle of height
Ω	-	Domain
$\bar{\varepsilon}^p$	-	Effective plastic strain
$\dot{\bar{\varepsilon}}^p$	1/sec	Effective plastic strain rate
$\bar{\varepsilon}$	-	Effective strain
$\bar{\sigma}$	N/mm^2	Effective stress
$\mathbf{C}^e$	N/mm^2	Elastic tangent modulus
$\hat{\mathbf{u}}^e$	mm	Elemental displacement vector
a	-	Exponent
$\mathbf{f}_{ext}$	N	External force vector
F^{bead}	-	Formability (GFLC value)
F^{lim}	-	Forming limit (= 1 for GFLC)
h_s	mm	Height of bead geometry
h	mm	Height of bead geometry
f_{Hill48}	N/mm^2	Hill48 yield function
ξ	-	Horizontal axis of isoparametric formulation
Δ	-	Increment
S_0	N/mm^2	Initial stress for Hochett-Sherby
σ_0	N/mm^2	Initial yield stress
σ^{iso}	N/mm^2	Isotropic hardening stress
λ	N/mm^2	Lame-constant
r_θ	-	Lankford coefficient depending on angle θ
$\mathbf{M}$	ton	Mass matrix
m	-	Material constant
$\mathbf{D}$	N/mm^2	Material tangent modulus
L_{min}	mm	Minimum element length
$\dot{\gamma}$	-	Plastic multiplier

Symbols	Unit	Meaning
$\dot{\boldsymbol{\varepsilon}}^p$	1/sec	Plastic strain rate tensor
$\boldsymbol{\varepsilon}^p$	-	Plastic strain tensor
P	N/mm²	Potential function
$X'_{1,2}$ and $X''_{1,2}$	N/mm²	principal values of linear transformation
r_s	mm	Radius of bead geometry
(n)	-	Reference state
f^{safe}	-	Safe factor
S_{sat}	N/mm²	Saturated stress
$\mathbf{N}$	-	Shape function matrix
G	N/mm²	Shear modulus
S_{sy}	N/mm²	Shear yield stress
H	N/mm²	slope of the flow stress
$\mathbf{K}$	N/mm	Stiffness matrix
K^{bead}	N/mm²	Stiffness of bead-formed part
ε_t	-	Strain in thickness direction
ε_w	-	Strain in width direction
λ_{post}	-	Strain path length ratio of post-forming
λ_{pre}	-	Strain path length ratio of pre-forming
β	-	Strain ratio
K	N/mm²	Strength coefficient
S	mm²	Surface of domain
$\mathbf{t}$	N/mm²	Surface traction
K^{obj}	N/mm²	Target stiffness
t	mm	Thickness
Δt	sec	Time increment
$\dot{\boldsymbol{\varepsilon}}$		Total strain rate tensor
$\boldsymbol{\varepsilon}$	-	Total strain tensor
b_p	mm	Total width of bead geometry
$\mathbf{n}$	-	Unit normal vector/ Unit normal for potential
$\mathbf{m}$	-	Unit normal vector of yield function

Symbols	Unit	Meaning
b_o	mm	Upper width of bead geometry
ζ	-	Vertical axis of isoparametric formulation
$\delta\mathbf{u}$	mm	Virtual displacement vector
V	mm^3	Volume of domain
σ_v	N/mm^2	Von Mises stress
c_d	mm/sec	Wave speed
Φ	-	Yield condition
σ_y	N/mm^2	Yield stress
ϕ_p	N/mm^2	Yld2000-2d potential function
ϕ_y	N/mm^2	Yld2000-2d yield function

List of abbreviation

Abbreviation	Meaning
AFR	Associated flow rule
BCC	Body centered cubic
CO_2	Carbon dioxide
utg	Chair of metal forming and casting
CAD	Computer-aided design
CCP	Convex cutting-plane
eMMFC	Enhanced Modified Maximum Force Criterion
FCC	Face centered cubic
FFT	Fast Fourier Transformation
FEM	Finite Element Method
FLC	Forming Limit Curve
FLD	Forming Limit Diagram
FLSD	Forming Limit Stress Diagram
FLPW	Forming Limit Plastic Work
GFLC	Generalized Forming Limit Concept
GTN	Gurson–Tvergaard–Needleman
IPEK	Institute of Production Engineering
KIT	Karlsruhe Institute for Technology
NVH	Noise, vibration, and harshness
Non-AFR	Non-associated flow rule
MMFC	Modified Maximum Force Criterion
OC	Optimality Criteria
PDE	Partial differential equation
PEPS	Polar effective plastic strain diagram
TUM	Technical University of Munich
VUMAT	User subroutine for Abaqus/explicit

1   Introduction

For decades, researchers have been trying to reduce the weight of machine parts. In particular, a development of the lightweight technology has been the focus of the automobile industry. Carbon dioxide (CO_2) emissions from internal combustion engines cause a global warming, and the lightweight technology is a means of reducing CO_2 emissions (Goede, 2009, Heuss et al., 2012). It is not only to pave the way for an efficient use of the finite fuel, but also to lighten the running performance. In recent years, the production and the use of electric vehicles is on the increase. Even though the problem of the CO_2 emission disappears due to the use of electric vehicles, it is pointed out that the driving distance of the electric vehicles is relatively short compared to that of the internal combustion engines. The vehicle weight reduction can be carried out so as to increase the driving distance even a little.

To achieve the weight reduction, a concept design is implemented (Schmidt and Puri, 2000). Depending on the purpose and the design, the number of parts and their shape and size are determined. The weight of the product is roughly determined by determining the body structure, the parts for each function, and the number of joints between the parts.
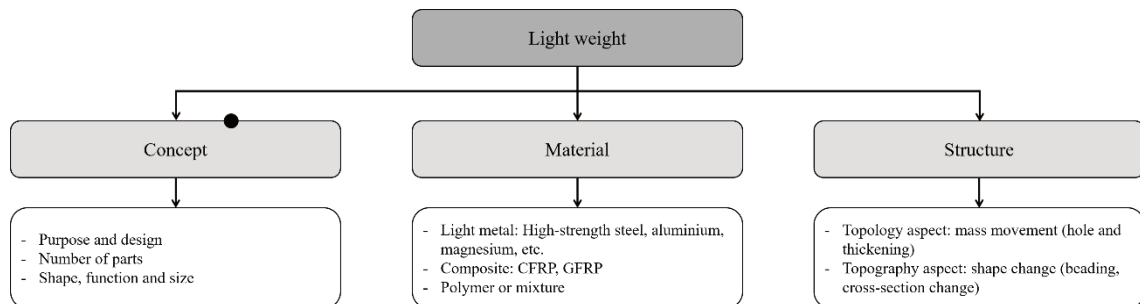
Figure 1.1: Strategies for light weight automobile

Next, the weight reduction can be achieved by using appropriate materials and designing a suitable structure (Schmidt and Puri, 2000). Lightweight and durable materials are used to reduce weight. For example, aluminum, high-strength steel, carbon fiber, composite materials, or mixtures are used. The lightweight materials can have expensive costs in 50% to 500% more than steels (Heuss et al., 2012). It was tried to reduce the cost of the carbon fiber by a recycling, but it still offers 20 to 30 percent a higher component cost than the steels (ELG Carbon Fibre Ltd., 2017). This is the most classical and the widely used lightweight method and it is also based on the technology to understand the mechanical properties of each material. When using

the mixed materials, the techniques of joining different materials should also be taken into consideration.

On the structural side, one way of increasing the stiffness of the part is by changing its geometry. Since the stiffness of the part increases with a thickness, the weight of a particular part can be reduced by reducing it to the thickness that has the minimum stiffness satisfying the stiffness condition if the maximum stiffness exceeds the stiffness criteria based on a safety or a stability. The precondition for this method is to know the space a part can occupy and the stiffness against any load condition. There are two types of optimization methods: topology, which uses the addition and the subtraction of materials, and topography, which uses a shape changes (Harzheim and Lieven, 2007). The difference in the method is that the material forming method used varies greatly. The optimization of the topology approach can increase or decrease the volume of the structure by increasing or reducing the material thickness. As a result, the thickness variation of the parts can be significant, and punching techniques for forging or punching a bulk forming process are mainly required. The topography optimization, on the other hand, changes the shape by inserting a regular bead into a part. This method is suitable for sheet metal parts with an almost constant thickness. For this purpose, a bending or a stretching method is used. However, as the part geometry becomes complicated to satisfy the design conditions, the forming becomes a challenge without causing material failures. This research focuses on a method to insert a bead into a sheet metal part as the shape change of the topography aspect to increase the specific stiffness.

For all of these lightweight methods, parts must ultimately be manufactured in production processes. Process parameters or geometries can be modified and optimized even if a part is manufactured with defect. A number of parameters can be investigated until a process condition to actually manufacture a complex target shape is determined. A material flow under various lubrication conditions can be investigated (Dietrich and Tschätsch, 2013). On a rough surface with an insufficient amount of a lubricating oil, a frictional force increases, so the material do not flow well in tools in deep drawing. As a result, an unexpected early fracture of the material occurs. A blank holding force also has a large effect on the material flow (Dietrich and Tschätsch, 2013). If the blank holding force is too large, a fracture may be occurred, and if the blank holding force is too small, a wrinkle defect may appear. In addition, a higher forming speed and a temperature positively affect the material formability (Fritz and Schulze, 2004). If the formability of parts is not satisfied under various forming process conditions, influences of the part geometry should also be investigated. If the corner radius is too small to be sharp, or if

the depth or height of the drawing is too large, there are chances that the part with extreme geometry constraints may have the significantly reduced formability. The material limitation in the forming process must be also taken into account. The mechanical properties according to each material affect differently on constraints of a part geometry. A proper selection and understanding of the material behavior are needed to manufacture parts. In the forming technology, it is needed to consider various cases regarding to processes, geometries and materials to accurately find the optimal production condition.

An experimental study can be prepared and carried out to investigate parameter influences on the production quality. For that, various tools with different geometries, various process conditions will be studied. However, only the experimental study is not proper to the optimization performance. The optimization requires at least numerous iteration although investigating some parameters. The experiment spends a lot of cost and time, moreover, hardly give a quantitative index for the optimization. For the reason, the numerical simulation is used to check a manufacturability and to efficiently find an optimal condition under various cases in the forming technology. The finite element method (FEM) is used to find a mathematical approximate solution using the plasticity theory. The FEM can solve complex nonlinear materials and geometries by dividing them into several linear elements and establishing linear simultaneous equations. A great advantage of using the FEM is that the simultaneous equations made by linearizing the nonlinear equations transforms complex partial differential equations (PDEs) into mechanical iterative equations. This allows complex problems to be solved quickly and repetitively using a computer. The plasticity theory expresses the irreversible deformation of metal materials by external forces or energies. In order to analyze the material behavior, the plastic behavior of materials is expressed as a single continuum and approximated with a mathematical model. Such a model is called a yield function or a yield locus, and von Mises (von Mises, 1913) is a representative example to describe an isotropic plastic deformation. By using this model, the stress due to the plastic deformation of the material can be calculated with the hardening model. Material yield functions are determined using the FEM.

Although stresses can be calculated efficiently by the forming simulation, it is not sufficient to accurately predict the forming limit. The formability can be determined based on thinning. Alternatively, the forming limit diagram (FLD) may determine a material failure. Although these methods are relatively simple, they are more effective when deformed under a constant load condition; otherwise, they are generally different from deformations in practical processes. When making actual parts, a continuous process with various load conditions is carried out rather than a one-step process with a simple part geometry mostly under a constant load

condition. The strain state after the continuous process may be nonlinear strain paths. The analysis of the forming limit under the nonlinear loading conditions should be required. The stress or strain values were analyzed to predict the forming limit under the nonlinear strain paths with inherent methods of the stress diagram (Stoughton, 2000), the polar effective strain diagram (Stoughton and Yoon, 2012) and the strain-based method (Volk et al., 2012).

These models have different material parameters that are determined using different types of material tests. Usually, the tests that can express tensile, compressive, and shear strain are performed to numerically determine the material properties. Under the various material deformation conditions, the stress, the strain, the Lankford coefficient (or r-value), etc. The anisotropy expression is derived and used to define the various parameters mentioned above. As a concrete sheet test method, a uniaxial tensile test, a bulge test and a Nakazima test are usually used. The uniaxial tensile and the bulge tests are used to determine the stress and the r-values calculated from the strains, and the Nakazima test is used to determine the necking or the fracture strain at the various deformation states using various initial specimen geometries. Since these measurements determine the parameters of the material models required for the analysis, a high accuracy of the test and measurement is presupposed.

The FEM and the optimization skill have been already used in the bead optimization regarding to material formability (Majić, 2014). The study showed that the optimal bead location to stiffen a sheet metal part can be determined along the direction of major bending stress. Furthermore, the bead geometry was considered in the formability by the conventional FLD. The conventional FLD inaccurately predict the material failure in different loading paths. It means that an actual bead part manufactured from multi-stage forming has not been considered in the bead optimization. Therefore, other method is required to improve the prediction accuracy in any forming case.

This research will deal with the formability consideration in the bead optimization to stiffen deep drawn parts by using the FEM, since the existing bead optimization techniques have not considered the part manufacturability. Furthermore, the efficient optimization procedure for the bead forming is suggested with a database that set an initial bead geometry. A study of the bead optimization considering the material formability is motivated. The FEM, a material model, a prediction model for the forming limit, and a sensitivity analysis are summarized. Explanations of the test machines and a measuring equipment are introduced to understand the experimental procedures. The material tests to identify the parameters of the material model are performed. The determined models are validated by comparing them with the measured values of the

material tests. A method to determine optimal bead locations has been developed by the Institute of Production Engineering (IPEK), Karlsruhe Institute of Technology (KIT). Thus, the optimal bead locations that maximize the stiffness of sheet parts are determined based on an optimization criterion by cooperation with IPEK. Influences of the bead geometries on the formability and the stiffness are investigated with the FE simulation. To validate the reliability of these analysis results, one representative case is selected to design a structure of the bead tool and to perform the bead forming in the experiment. The material model is validated by comparing the calculated and measured strains of the preformed and the bead formed part. The prediction model for the forming limit and the FE simulation for the stiffness are validated by the material failure and the loading tests, respectively.

2   State of art

2.1   Bead geometry

One of the ways to increase the stiffness of sheet parts is to insert bead geometries. The insertion of the bead improves not only the stiffness, but also the material behavior for noise and vibration. The cross-section of the bead geometry can be optimized according to purposes to satisfy a target stiffness or noise. As shown in the Figure 2.1, representative types of the bead geometry can be classified into four types of box, trapezoidal, triangle, and round.

| Box | Trapezoidal | Round | Triangle |
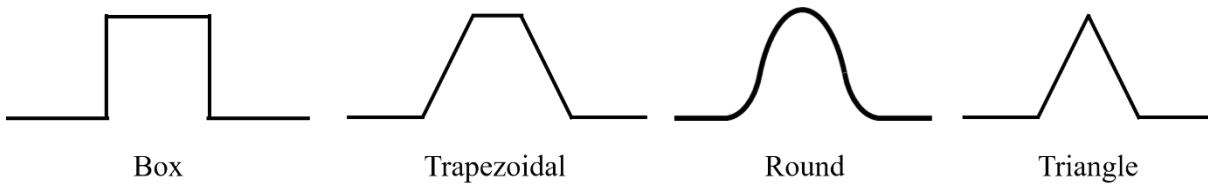
Figure 2.1: Cross-sections of representative bead geometries

The box bead has the highest stiffness for a vertical load, and the triangle bead has the lowest. However, the bead geometry should be chosen to account for the high stiffness of a part under a certain load condition (Majić, 2014).
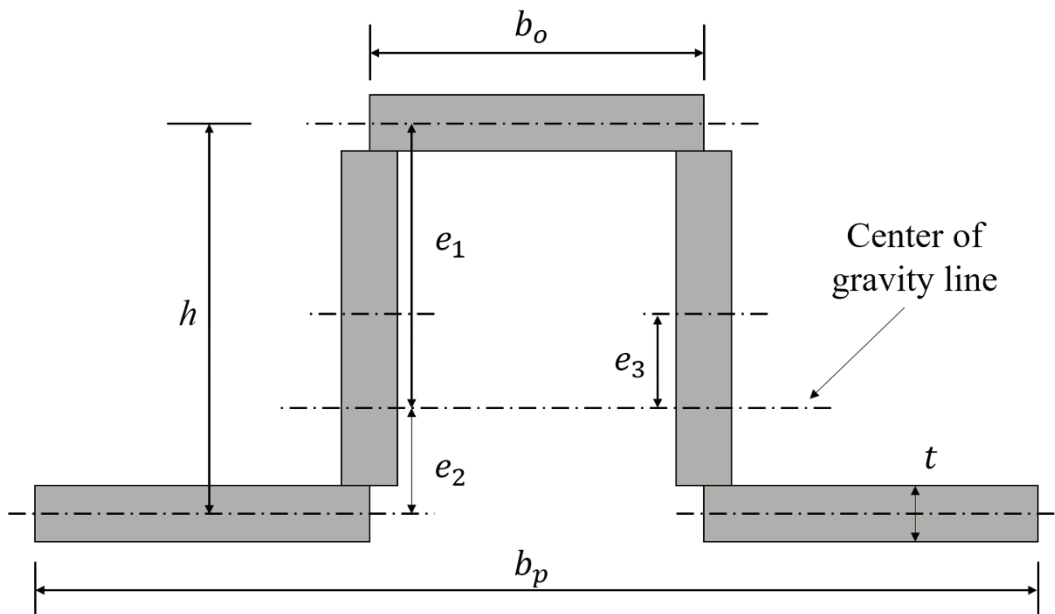
Figure 2.2: Simple box bead (Emmrich, 2005)

The stiffness of sheet metal parts is generally highly resistant to deflection and increases by the increase in the area moment of inertia. The bead geometry moves weight line of the sheet and increases the area moment of inertia based on the Steiner's theorem. Especially, the bead height

has a great influence on that increases the stiffness of sheets. It was already investigated that the stiffness increase is strongly dependent on the bead height (Emmrich, 2005). The area moment of inertia I can be expressed by the following Equation 2.1 based on the simple box bead as shown in Figure 2.2.

$$I = \frac{b_p t^3}{12} + 2\frac{t(h-t)^3}{12} + e_1^2 t b_o + e_2^2(b_p - b_o) + 2e_3^2 t(h-t) \qquad \text{Equation 2.1}$$

Here b_o, b_p, h, and t are the upper width, the total width, the height, and the thickness of the bead geometry, respectively. e_1, e_2, and e_3 are defined as the distance of gravity line from the upper width, the lower width, and the middle of height, respectively.

It is clear from Equation 2.1 that increasing the thickness can increase the area inertia moment. On the one hand, the thickness increase is not meaningful to stiffen sheet metal parts, since it increases the weight of the parts. The heavy parts are an unexpected result and a critical problem for the strategy of the lightweight. On the other hand, the bead height has also the great influence on the area moment of inertia. The increase in the bead height increases the area moment of inertia and the stiffness of sheet parts exponentially. If the increased stiffness is large than the target stiffness, the part weight can be reduced using a sheet with a lower thickness. Therefore, the height of the bead geometry is the main parameter in the bead optimization to achieve the lightweight of the sheet parts.

The bead rate was defined as ratio of the area of the upper bead A_u to the area of the lower bead A_l to find an optimal width of the bead geometry based on the box bead as shown in Figure 2.2. The definition of the bead rate φ is expressed by the following (Emmrich, 2005).

$$\varphi = \frac{A_u}{A_l} = \frac{b_o}{b_p - b_o}. \qquad \text{Equation 2.2}$$

When the bead rate is equal to 1, the effect of the stiffening is maximized (Emmrich, 2005), indicating that the upper and the lower widths have the same value. Therefore, the width of the bead geometry is optimized based on the bead rate.

With the box bead, the influence of the bead geometry was introduced. However, the flank angle of 90° may not be produced in practice in the aspect of the manufacturability. The local deformation increases with a large flank angle and it can lead to cracks. The flank angle between 60 and 70 can be selected generally (Schwarz, 2002). Furthermore, the flank angle of the bead geometry mainly influence the strength but not the stiffness (Herrmann, 1997). The flank angle is not the main control parameter for maximizing the stiffness of the part.

When the bead forming in practice is performed, the flank angle has to be set smaller than 90 degrees in order to improve the bead formability. Thus, it is not easy to determine the bead geometry in the above manner, but it can be confirmed that the bead height has the greatest influence on the increase in the stiffness. Therefore, in order to effectively increase the stiffness of the sheet part by the bead geometry, the bead optimization strategy is to increase the bead height as much as possible within the producible limit.

2.2   Algorithm of bead optimization

Empirical methods to design beads for stiffening thin-walled sheet metal parts have been developed in numerous studies from the 1950s to the mid-1990s. With the rapid development of a computer technology in the 1990's, as well as increasing demands on lighter and stiffer sheet metal structures, FEM-based simulation programs have been increasingly used. The work of (Bendsøe and Kikuchi, 1998) provided the basic study for numerous developments of processes whose common feature is the formation of an objective function, which is minimized by means of their analytically or approximately determined sensitivities. A method for an optimal bead pattern was developed using the topology optimization in the FE-simulation with a bead-and-shell element, in order to improve a stiffness and a NVH (noise, vibration, and harshness) performance of the metal sheet. This method creates a beam element at each edge of the shell element and removes the low-density beam elements by the topology optimization. The remaining beam elements are thus determined to be the optimized the bead locations (Yang et al., 1996). (Luo and Gea, 1998) optimized the bead locations with an energy-based optimization of the orientation of orthotropic materials. Since 1999, Altair Engineering Inc., Troy, USA, has been offering topography optimization within OptiStruct optimization software (Altair, 2000). The geometry of the FE model is modified using shape-base vectors, which represent a local node shifting of the structure. The OC-algorithm (Optimality Criteria) developed by Emmrich (Emmrich, 2005) in 2004 is based on the evaluation of the bending load of the sheet metal structure and is implemented in the commercial optimization software TOSCA (FE-DESIGN GmbH, Karlsruhe) as module TOSCA Structure.bead (TOSCA, 2009). In the OC-algorithm, the beads are aligned in the direction of the greatest bending stress (Majić, 2014). The bead geometries are formed along the bead path generated based on the major bending stress trajectories. Nodes on the trajectories are shifted to form the designed bead geometry. The bead forming by the node shift fulfills only the geometrical requirement and does not take the material behavior into account. The main advantages of this method are the

short calculation time and the easier interpretability of the bead patterns. Thereafter, the numerical optimization methods for the bead design to improve NVH performance and stiffness of sheet parts have been improved in the efficiency and the stability (Maressa et al., 2010, Leiva, 2011, Bilik et al., 2012).

The optimization methods for a bead design have been developed so far, and efficiency and stability have also been continuously improved. The bead locations and geometries determined by the bead optimization have to be applied in actual sheet metal parts. For this, a production process for bead forming has to be required. When constraints are considered in the process, the bead locations or geometries are usually modified. The material formability was considered in bead optimization using FLC, but it did not involve the influence of the practical continuous processes on the formability (Krönauer et al., 2010 and Albers et al., 2010). An optimization process was developed to automate a bead generation for sheet metal stiffening and one-step inverse forming simulation for formability evaluation. The lager bead widths were suggested as a solution to improve the manufacturability without optimal stiffening effect (Majić et al., 2013).

In conclusion, the material formability in complex deformation histories was not considered in the bead optimizations having the optimal stiffening effect.

2.3 Finite Element Method (FEM)

The FEM is the most widely used method among the current numerical methods to solve engineering problems. Its greatest strength is that the nonlinear second-order PDEs can be replaced by linear simultaneous equations, which can be easily solved. Because of the nonlinear properties of geometry and materials in ordinary engineering problems, it is almost impossible to obtain the solutions of the nonlinear second order PDEs from the real problems. FEM transforms the nonlinear geometry into the combination of linear geometries through a geometric discretization, and the nonlinear material behavior can be approximated to the real solution by an iterative numerical processing and a gradual approach. The linear simultaneous equations system created by this method makes a mechanical iterative calculation possible. In other words, by using a computer that can do the fastest calculation, no matter how complex and vast the problems, we obtain the solution you want within a few hours to days. Due to the recent advances in the computational computation speed, the availability and importance of the FEM is increasing, and analytical methods in the virtual world are likewise more frequently selected than an experimental engineering design and a problem solving.

2.3.1 Weak form

The linear moment balance gives the equilibrium equation for the material deformation as follows (Reddy, 1993):

$$\text{div } \boldsymbol{\sigma} + \mathbf{b} = \rho \ddot{\mathbf{u}} \text{ in } \Omega, \qquad \textit{Equation 2.3}$$

where $\boldsymbol{\sigma}$ is a tensor of the Cauchy stress, $\ddot{\mathbf{u}}$ is the second derivative of a displacement over time and physically means the acceleration, ρ is the mass density, Ω is a domain and $\mathbf{b}$ is a body force vector. The stress is symmetric due to the balance of angular momentum (Lubarda, 2000). A weak form can be constructed by multiplying an appropriate arbitrary function, which has the same free indices as in the set of governing equations. The virtual work is a weak form in which the arbitrary function is a virtual displacement $\delta\mathbf{u}$ (Zienkiewicz et al., 2014). By this, the following form is obtained:

$$\int_{\Omega} \left(\text{div } \boldsymbol{\sigma} + \mathbf{b} - \rho \ddot{\mathbf{u}}\right) \cdot \delta\mathbf{u} \, dV = 0, \qquad \textit{Equation 2.4}$$

where V is the volume of the domain. By the divergence theorem and the symmetric stress tensor, the volume integral form can be transformed into the surface integral form as shown in the following equations:

$$\text{div } (\boldsymbol{\sigma}\delta\mathbf{u}) = \boldsymbol{\sigma} \cdot \text{grad } \delta\mathbf{u} + \text{div } \boldsymbol{\sigma} \cdot \delta\mathbf{u}, \qquad \textit{Equation 2.5}$$

$$\int_{\Omega} \text{div } (\boldsymbol{\sigma} \cdot \delta\mathbf{u}) dV = \int_{\partial\Omega} (\boldsymbol{\sigma}\delta\mathbf{u}) \cdot \mathbf{n} dS = \int_{\partial\Omega} (\boldsymbol{\sigma}\mathbf{n}) \cdot \delta\mathbf{u} dS, \qquad \textit{Equation 2.6}$$

where S is the surface on the domain. The virtual work can be represented by inserting the transformed term of div $(\boldsymbol{\sigma}\delta\mathbf{u})$ as

$$\int_{\Omega} \boldsymbol{\sigma} \cdot \text{grad } \delta\mathbf{u} dV + \int_{\Omega} \rho \ddot{\mathbf{u}} \cdot \delta\mathbf{u} dV = \int_{\Omega} \mathbf{b} \cdot \delta\mathbf{u} dV + \int_{\partial\Omega} (\boldsymbol{\sigma}\mathbf{n}) \cdot \delta\mathbf{u} dS. \qquad \textit{Equation 2.7}$$

The left-hand side is the virtual inner work and the right-hand side is the virtual outer work. It is shown that it is transformed into a weak form of integral expression in a PDE. This allows equations for material deformation problems to be solved into linear simultaneous equations, allowing nonlinear solutions of complex materials and geometries to be similarly obtained.

2.3.2 Boundary condition

The boundary condition is divided into two kinds. One is the Neumann boundary condition (force boundary condition) and the other is the Dirichlet boundary condition (displacement boundary condition) (Reddy, 1993).

The Neumann boundary condition is represented as

$$\boldsymbol{\sigma}\mathbf{n} = \mathbf{t} \text{ on } \partial\Omega_t, \qquad\qquad \textit{Equation 2.8}$$

where $\mathbf{n}$ has the components of the normal vector on boundary, $\mathbf{t}$ is the surface traction, and $\partial\Omega_t$ is the force boundary of the domain. The Dirichlet boundary condition is represented as

$$\mathbf{u} = \mathbf{u}_0 \text{ on } \partial\Omega_u, \qquad\qquad \textit{Equation 2.9}$$

where $\mathbf{u}_0$ is the constant displacement vector, and $\partial\Omega_u$ is the displacement boundary of the domain. At any location of the boundary $\partial\Omega$, only one kind of boundary condition exists (Reddy, 1993). This rule is expressed as

$$\partial\Omega = \partial\Omega_u + \partial\Omega_t. \qquad\qquad \textit{Equation 2.10}$$

2.3.3 Discretization

The description of laws of physics for space- and time-dependent problems is generally expressed in terms of PDEs. For the complex geometries, these PDEs cannot be solved with analytical methods. Industrial parts in a practice has complex geometries like lines, complex curves, convex or concave surfaces. The discretization method approximates the PDEs with numerical model equations that can be solved. This complex geometry can be transformed into a combination of linear geometries by the discretization method in order to solve the problem with the nonlinear geometries.

A displacement u that depends on the material stiffness and the forces can be approximated by an approximate displacement ũ in the forming. The approximate displacement can be expressed using a shape function *N* as follows (Reddy, 1993):

$$\mathbf{u} \approx \tilde{\mathbf{u}} = \sum_{i=1}^{n} N_i \hat{u}_i^e = [N_1, \quad \cdots, \quad N_n(\mathrm{x})] \begin{bmatrix} \hat{u}_1 \\ \vdots \\ \hat{u}_n \end{bmatrix} = \mathbf{N}\hat{\mathbf{u}}^e, \qquad \textit{Equation 2.11}$$

where $\hat{\mathbf{u}}^e$ is the elemental displacements. The shape function depends on the number of nodes per element, the element types, and the space dimensions. For example, the triangular and/or

quadrilateral elements are usually used in two dimensions. The tetrahedral and/or the brick elements are usually used in three dimensions. A quadrilateral element can have four-node or nine-nodes and their shape function can be a linear or a quadratic function, respectively (Zienkiewicz et al., 2014). The following equation shows the shape function of the quadrilateral element in the isotropic formulation as shown in Figure 2.3:

$$N_1 = \tfrac{1}{4}(1 - \xi)(1 - \zeta), N_2 = \tfrac{1}{4}(1 + \xi)(1 - \zeta),$$
$$N_3 = \tfrac{1}{4}(1 + \xi)(1 + \zeta), N_4 = \tfrac{1}{4}(1 - \xi)(1 + \zeta).$$

Equation 2.12
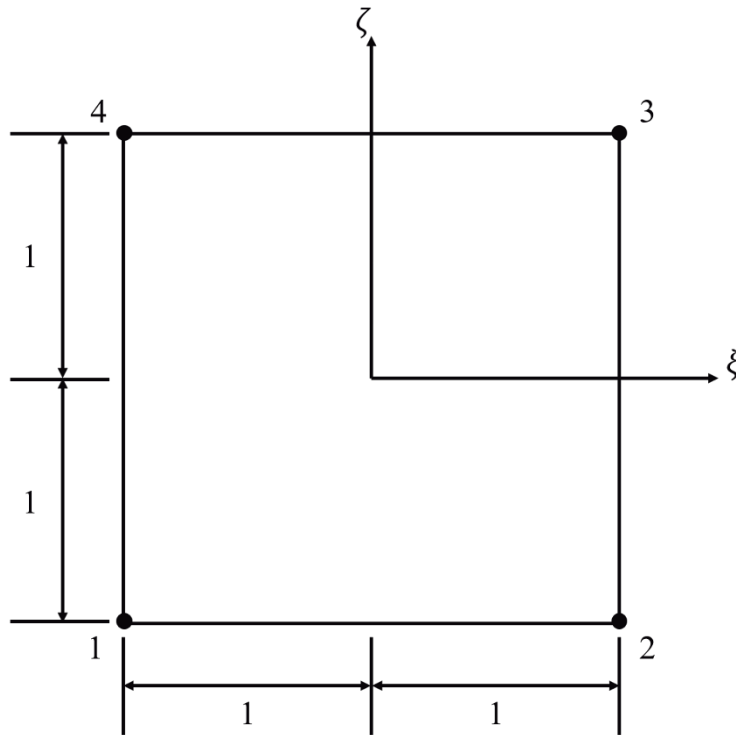
Figure 2.3: The coordinates for a quadrilateral and node numbering for four nodes in isotropic formulation

The isoparametric formulation leads to the simplification of the necessary integration. The Gauss-quadrature algorithm usually integrates in the isotropic formulation (Reddy, 1993). The deformation of the sheet metal follows the plane stress condition that assumes a negligible stress in the thickness direction. Because of this, the shell element with the same formulation as the quadrilateral element is used in the forming simulation with the sheet metal. Since the thickness change is considered, the strain in the thickness direction is calculated by the linear elasticity in the elastic deformation or by the volume constant in the plastic deformation.

2.3.4 Finite element model

The finite element model is built in a matrix form from the weak form with the approximate displacement as follows:

$$\delta \hat{\mathbf{u}} \left[\int_{\Omega} \mathbf{DB\hat{u}} \cdot \mathbf{B} dV + \int_{\Omega} \mathbf{N} \rho \ddot{\hat{\mathbf{u}}} \cdot \mathbf{N} dV = \int_{\Omega} \mathbf{b} \cdot \mathbf{N} dV + \int_{\partial\Omega} \mathbf{t} \cdot \mathbf{N} dS \right], \qquad \text{Equation } 2.13$$

where $\mathbf{D}$ is the tangent modulus obtained from the constitutive law, and $\mathbf{B}$ is the displacement differentiation matrix. Equation 2.13 can be simplified as follows.

$$\int_{\Omega} \mathbf{B}^{\mathrm{T}} \mathbf{DB} \, dV \, \hat{\mathbf{u}} + \int_{\Omega} \mathbf{N}^{\mathrm{T}} \mathbf{N} \rho dV \, \ddot{\hat{\mathbf{u}}} = \int_{\Omega} \mathbf{N}^{\mathrm{T}} \mathbf{b} dV + \int_{\partial\Omega} \mathbf{N}^{\mathrm{T}} \mathbf{t} dS, \qquad \text{Equation } 2.14$$

$$\mathbf{K\hat{u}} + \mathbf{M}\ddot{\hat{\mathbf{u}}} = \mathbf{f}_{body} + \mathbf{f}_{ext}, \qquad \text{Equation } 2.15$$

where $\mathbf{K}$ and $\mathbf{M}$ are the stiffness matrix and the mass matrix depending on the material, respectively, and, $\mathbf{f}_{body}$ and $\mathbf{f}_{ext}$ are the body and the external force, respectively.

The matrix form of the linear simultaneous equations can be solved by the inverse of the stiffness matrix. The solution is carried out using a computer. For this reason, FEM approximates the complex PDEs, and the developed computer solves it rapidly.

2.3.5 Simulation type and solver

The simulation type in the material deformation can be divided into several types according to the physical cases. One is the static simulation used to predict the static deformation by the external force without the rigid body motion. The mass matrix $\mathbf{M}$ in the Equation 2.14 is treated as a zero matrix. The displacements are calculated with the stiffness matrix $\mathbf{K}$ in the static simulation. The static simulation is usually applied usually for the structure analysis to predict a stiffness. Another is the dynamic simulation that describes the rigid body motion and the inertia effect considering the mass matrix $\mathbf{M}$ in the Equation 2.15. The deformation and the rigid body motion can be simulated over time. The last is the quasi-static type that calculates the static deformations over time.

The FEM solving has the two methods mathematically. The implicit method is carried out by the iterative procedure like the Newton-Raphson method to converge the solution with a convergence criterion. Thus, the equilibrium is satisfied with the converged solution per time

step. The time step can be given relatively more than that of the explicit method. However, high nonlinear problems or contact problems often lead to the fact that the solution is not converged. In contrast, the explicit method gives the solution in most problems, since the explicit method do not consider the convergence and the equilibrium. The stable criterion for the time step is used to guarantee the accuracy of the solution. The stable criterion is expressed in the following. (Belytschko et al., 2000):

$$\Delta t \leq \Delta t_{krit} \approx \frac{L_{min}}{c_d}, \qquad\qquad \textit{Equation 2.16}$$

$$c_d = \sqrt{\frac{\lambda + 2G}{\rho}}, \qquad\qquad \textit{Equation 2.17}$$

where Δt is the time step or time increment and Δt_{krit} is the critical time step. The time step should not exceed the critical time step. L_{min} is the minimum element length and c_d is the wave speed calculated of a Lame constant λ, a shear modulus G, and a density ρ (Belytschko et al., 2000).

The die or the punch with the blanking holder in the drawing process moves to deform the sheet. The sheet has also the deformation and the rigid body motion by the contact with the tools. Thus, the forming simulation should consider the effects of the time and the mass by the dynamic/explicit method.

2.4 Metal plasticity

A yield function is needed to describe the permanent deformation of the material in the forming process simulation. In particular, the anisotropic yielding function is used in the sheet metal forming simulation, because the sheet metal has a planar anisotropy by the rolling process. This chapter introduces mathematical representations of the plastic deformation, various yield function models, and the material flow laws in the continuum state.

2.4.1 Yield condition

The plastic deformation is irreversible because the material deformation due to the load does not return to the original shape even when the load is removed. Conversely, when the load is restored to its original shape, the reversible deformation is called an elastic deformation. If the external force such as a load is smaller than the yield stress, which is the internal stress of the

material, an elastic deformation occurs. If it is equal to the internal stress, a plastic deformation occurs. This is a simple explanation of the elastic and plastic deformation. The yielding condition indicates that the internal stress and the external force of the material are the same (Simo and Hughes, 1998). Mathematically, it is expressed as

$$\Phi(\boldsymbol{\sigma}, \sigma_y) = \bar{\sigma}(\boldsymbol{\sigma}) - \sigma_y(\bar{\varepsilon}^p) = 0, \qquad \textit{Equation 2.18}$$

where Φ is the yield condition equation. $\bar{\sigma}$ is the effective stress of the yield function, which is a function of a Cauchy stress tensor $\boldsymbol{\sigma}$ and is calculated as a scalar value by a deformation under external loading. σ_y is a yield stress or flow stress, which is a function of an equivalent plastic strain $\bar{\varepsilon}^p$. When the effective stress reaches the yield stress, the material has the plastic deformation. σ_y is generally determined from the uniaxial yield stress. When the effective stress is lower than the yield stress, it is called the elastic deformation and satisfies the following:

$$\bar{\sigma}(\boldsymbol{\sigma}) < \sigma_y(\bar{\varepsilon}^p). \qquad \textit{Equation 2.19}$$

The important thing is that any stress states should not exceed the current yield stress and is called plastically admissible stresses. In other words, the internal stress of the material cannot be larger than the external force. The constraint on this is expressed as

$$\Phi(\boldsymbol{\sigma}, \sigma_y) \leq 0. \qquad \textit{Equation 2.20}$$

The yielding conditions should only be considered when an elastic stress, an unloading, and a plastic yield occur. Three cases can be expressed as shown in Figure 2.4, where the elastic region in the uniaxial state, the plastic load, and the elastic strain are expressed as the yield stress for the strain.

$$\text{if } \Phi(\boldsymbol{\sigma}, \sigma_y) < 0 \implies \dot{\bar{\varepsilon}}^p = 0, \qquad \textit{Equation 2.21}$$

$$\text{if } \Phi(\boldsymbol{\sigma}, \sigma_y) = 0 \implies \begin{cases} \dot{\bar{\varepsilon}}^p = 0 & \text{for elastic unloading,} \\ \dot{\bar{\varepsilon}}^p \neq 0 & \text{for plastic loading.} \end{cases} \qquad \textit{Equation 2.22}$$
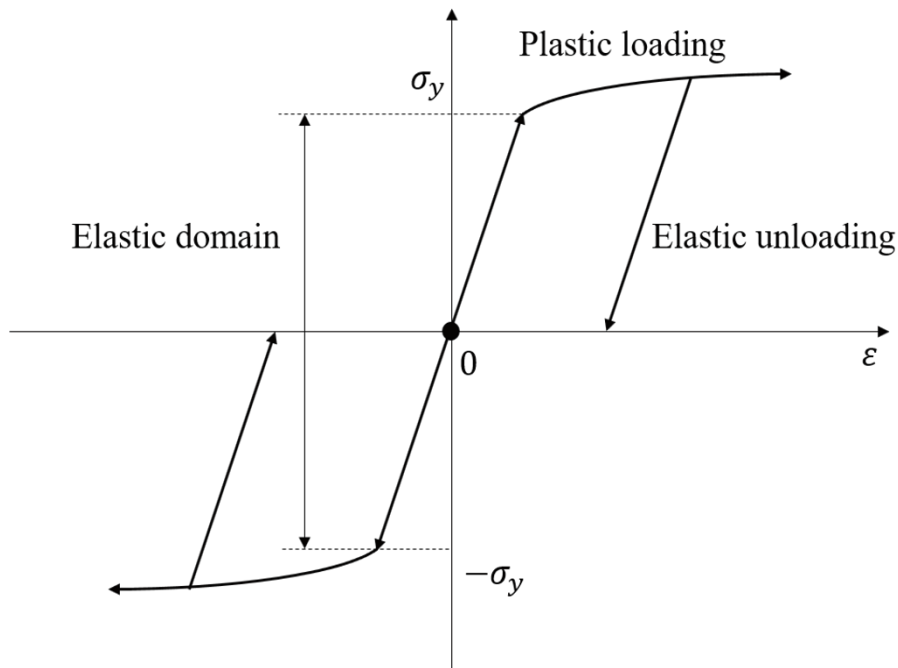
Figure 2.4: Description of elastic and plastic deformation under loading and unloading

2.4.2 Flow rule

The flow rule can be expressed as an Equation 2.23 in relation to a plastic strain rate tensor as the product of the direction of a plastic strain rate $\frac{\partial P}{\partial \boldsymbol{\sigma}}$ and a plastic multiplier $\dot{\gamma}$ under the plastic load:

$$\dot{\boldsymbol{\varepsilon}}^p = \dot{\gamma}\frac{\partial P}{\partial \boldsymbol{\sigma}}, \qquad\qquad Equation\ 2.23$$

where $\dot{\boldsymbol{\varepsilon}}^p$ is the plastic strain rate tensor, and $\boldsymbol{\sigma}$ is the Cauchy stress tensor. $\dot{\gamma}$ is the plastic multiplier and always has a positive value. P is involved in the direction of the plastic strain rate and is called the potential function. $\frac{\partial P}{\partial \boldsymbol{\sigma}}$ is the directional vector of the yield stress as a partial derivative of the potential function for the stress tensor, and its size is 1. If the potential function is not defined separately and the yield function is used, it is called the associated flow rule (AFR). In the AFR, the normal vector of the continuous, the differentiable yield function determines the direction of the plastic strain rate.

The AFR generally exhibits an anisotropic material behavior in single-phase materials and polycrystalline materials. However, the AFR concept has been shown by various investigations to be an anisotropic representation of high anisotropic materials. For example, the AA48-T4 and AA2090-T3 materials were not well calculated for the AFR-based anisotropic yield model

Hill48 with *r*-values and yield stresses. Yld2000-2d and Hill48 did not accurately represent the material behavior for *r*-values and yield stresses of AA2090-T3 (Park and Chung, 2012). The need for a non-associated flow rule (non-AFR) has increased for high anisotropic material representations. It has been known that a plastic deformation generally does not depend on hydrostatic stress (Hill, 1948). However, a hydrostatic stress has been found to affect plastic deformation, and the non-AFR should be used to express it (Stoughton and Yoon, 2014). The importance of the non-AFR concepts that have not been previously considered in the development of metal materials, measurement techniques, and computational capabilities is increasing.

The non-AFR, as the name suggests, defines the plastic potential function differently than the yield function, unlike the AFR. The difference between the yield function and the potential function is determined by the normal vector of the potential function, not by the normal vector of the yield function. The potential function, which is different from the yield function in non-AFR, can be used in conjunction with the formula of the yield function or any other type of function. When the potential function borrows the same form as the yield function, the empirical values required to determine the coefficients of the function are different. The coefficients of the potential function are usually determined on the basis of *r*-values and the coefficients of the yield function are determined based on the stress (Safaei et al., 2014).

The AFR and the non-AFR are introduced and they have a great influence on determining the direction of the plastic strain rate. Considering this, we try to predict the expression of material anisotropy with high accuracy, which has a significant influence on expressing the behavior of a thin sheet material.

2.4.3 Hardening model

As a deformation progress, the lattice rotation appears by the potential slip, and the phenomenon accumulates and becomes an obstacle to the next deformation. Thus, the resistance to dislocation slip increases during plastic deformation. When the load is removed during plastic deformation, the increased yield stress becomes the new yield stress (Cardoso and Yoon, 2009). It is said that a work hardening is caused by a plastic work and an increasing of a material strength. It is also referred to as a strain hardening because a plastic strain is increased by the plastic work.

The hardening behavior can be expressed by a hardening model. Different hardening models are used for different hardening phenomena. The isotropic hardening is that the yield surface

simply expands in a size while retaining its shape during a plastic deformation. It is reasonably used in process analysis where the direction of the load does not change (Chung et al., 2005). The hardening behavior when the direction of the load is changed cannot be rightly represented by the isotropic hardening model. The hardening in a cyclic loading, reversed loading, and spring back can be represented by a kinematic hardening, because the kinematic hardening model is able to express the change in a yield surface by changing the loading direction by moving the yielding surface with a variable called the back-stress **q**. However, only the kinematic hardening model underestimates the stress from the reversed load. Only the isotropic hardening model gives a higher stress in the same case. Thus, a combination hardening with the isotropic and the kinematic hardening is proposed. The yield surface can have expansion and translation, and the ratio of the combinations is determined experimentally. The hardening models described are shown in Figure 2.5.
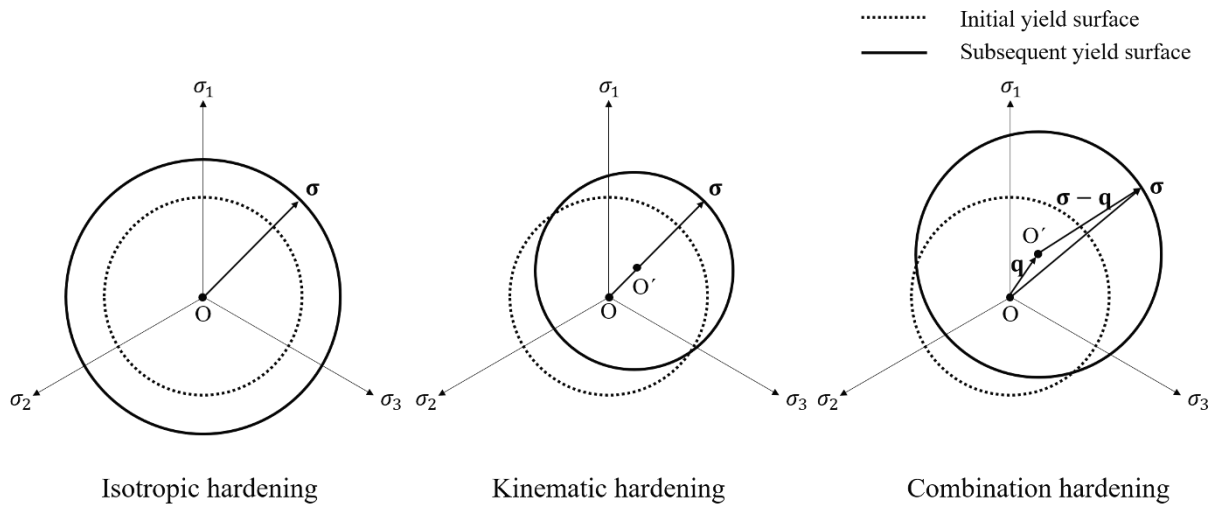
Figure 2.5: Description of hardening models

Following are the models for expressing isotropic hardening:

Ludwik
$$\sigma^{iso} = \sigma_0 + K\bar{\varepsilon}^{p^n},$$
Equation 2.24

Hollomon
$$\sigma^{iso} = K\bar{\varepsilon}^{p^n},$$
Equation 2.25

Swift
$$\sigma^{iso} = K(\bar{\varepsilon}_0 + \bar{\varepsilon}^p)^n,$$
Equation 2.26

Hockett-Sherby
$$\sigma^{iso} = S_{sat} - (S_{sat} - S_0)\exp(-m\bar{\varepsilon}^{p^n}),$$
Equation 2.27

where σ^{iso} is an isotropic hardening stress, σ_0 is an initial yield stress, K is a strength coefficient, n is a strain hardening exponent, S_{sat} is a saturated stress, S_0 is an initial stress for Hockett-Sherby, and m is a material constant describing typical hardening behavior. The parameters in the hardening model equations are generally fitted to the flow stress determined by the experiment. The flow stress from the uniaxial tensile test is usually used as reference to fit the hardening model. The uniaxial flow stresses of sheet metals are obtained up to an elongation of about 20 % without material instability like necking. Only the homogeneous flow stress can be used to fit the isotropic hardening model that do not consider the material softening. The hardening behavior over the elongation of 20 % is extrapolated depending on the selection of the hardening model. In order to obtain the actual material hardening curve over the elongation of 20 %, the bulge test can be used with the membrane theory (DIN EN ISO 16808, 2014). Even if the flow curve in longer elongation is measured, one hardening model can express an analytical flow curve with some error. The different hardening models can be combined by the interpolation to express the accurate flow curve. Therefore, the isotropic hardening models can be accurately selected and combined based on the biaxial flow stress from the bulge test.

Several kinematic hardening models are Prager (Prager, 1958) and Ziegler (Ziegler, 1959), which are linear models and have limitations describing the nonlinear hardening behavior, and the Armstrong-Frederick (Armstrong and Frederick, 1966), and the Chaboche models (Chaboche, 1986) for considering nonlinearity. (Yoshida and Uemori, 2002) announced the two-surface models to predict a very accurate elastic recovery, but the high complexity of implementation and parameter optimization is required to use this model. They can be used as combination hardening models mainly to calculate the elastic recovery in a reversed loading condition.

2.4.4 Isotropic yield function

The isotropic yield function describes the yielding in all directions of the yield surface. Tresca and von Mises are referred to the oldest yield functions. Tresca yield function (Tresca, 1864) is the theory due to maximum shear stress. This is expressed by the following equation.

$$\frac{1}{2}\max(|\sigma_1 - \sigma_2|, |\sigma_2 - \sigma_3|, |\sigma_3 - \sigma_1|) = S_{sy} = \frac{1}{2}S_y \qquad \textit{Equation 2.28}$$

where S_{sy} is a shear yield stress, and S_y is a tensile yield stress. The Tresca model has a hexagonal shape in the 3D principal stress space. The disadvantage is the vertex of the Tresca

yield surface. This does not guarantee the yield of the material as a unique value in the numerical analysis.

The von Mises model (von Mises, 1913) is widely used as an isotropic yield function so far and referred to as the representative isotropic model. The yielding of ductile materials begins with reaching the second invariant of deviatoric stress based on the von Mises. This is mathematically expressed as follows:

$$\sigma_v = \sqrt{\frac{3}{2} s_{ij} s_{ij}}, \qquad \qquad \textit{Equation 2.29}$$

where s_{ij} are the components of deviatoric stress. It is known that the yielding only depends on the deviatoric stress, not on the hydrostatic stress based on the theory. Taylor and Quinney investigated the yield stresses of a copper, an aluminum, and a mild steel by the material test and announced that the von Mises model has more accuracy of the material yielding than the Tresca model (Taylor and Quinney, 1931).

Hershey firstly introduced a non-quadratic formulation of the yield criterion as the following (Hershey, 1954).

$$(\sigma_1 - \sigma_2)^a + (\sigma_2 - \sigma_3)^a + (\sigma_3 - \sigma_1)^a = 2\sigma_y{}^a, \qquad \textit{Equation 2.30}$$

where σ_y and a are an uniaxial yield stress and an exponent, repectively. For $a = 2$, the Hershey model has the same condition with the von Mises model. For $a = 1$ or $a \rightarrow \infty$, it is translated to the Tresca model. Exponent a is determined from the crystallographic structure of the material. The Hershey model is more flexible than the von Mises and Tresca model with the exponent a. The isotropic yield function is effective when predicting plastic deformation at the bulk forming, but there is a limit to expressing the yield of the thin metal sheet produced by the rolling process because thin sheets have different anisotropies at the yield point depending on the rolling direction.

2.4.5 Anisotropy

Sheet metals have an anisotropic material behavior due to the rolling process. The anisotropic property exhibits the symmetric characteristic with respect to three orthogonal planes and is called the orthotropic anisotropy. In general, the orientation of the sheet metals has three directions: the rolling direction (RD), the transverse direction (TD), and the normal direction (ND).

In order to define the anisotropic property quantitatively, the anisotropy coefficient or the Lankford coefficient was presented as a ratio of strain in the width direction ε_w to strain in the thickness direction ε_t (Lankford et al., 1950). The definition is expressed in the following equation:

$$r_\theta = \frac{\varepsilon_w}{\varepsilon_t},$$
<div align="right">*Equation 2.31*</div>

where θ is the angle to a rolling direction, because the Lankford coefficient depends on the in-plane direction. The tensile specimen is cut having its longitudinal axis inclined with respect to the rolling direction and is carried out in the uniaxial tensile test to determine the Lankford coefficient. The width direction can be different from the transverse direction.

The anisotropic material behavior was detected under equivalent biaxial loading (Banabic and Wagner, 2002, Barlat et al., 2003). (Barlat et al., 2003) called the quantitative expression as the coefficient of the biaxial anisotropy r_b. The coefficient of the biaxial anisotropy is defined as

$$r_b = \frac{\varepsilon_{22}}{\varepsilon_{11}},$$
<div align="right">*Equation 2.32*</div>

where ε_{11} and ε_{22} are the major and minor strain on the elliptic surface, respectively.

2.4.6 Anisotropic yield function

Since the thin sheet is produced by the rolling process, it necessarily has a different yielding property depending on the direction different from the rolling direction. An anisotropic yield function was developed to account for this property, and Hill first published an anisotropic yield function (so-called Hill48) in the von Mises function to a quadratic function in 1948 (Hill, 1948). This yield function expresses the anisotropy with three orthogonal symmetry planes. Hill48 is expressed by the following equation:

$$2f_{Hill48}(\sigma_{ij}) \equiv F(\sigma_{22} - \sigma_{33})^2 + G(\sigma_{33} - \sigma_{11})^2 + H(\sigma_{11} - \sigma_{22})^2 + 2L\sigma_{23}^2 + 2M\sigma_{31}^2 + 2N\sigma_{12}^2 = 1,$$
<div align="right">*Equation 2.33*</div>

where f_{Hill48} is the Hill48 yield function and F, G, H, L, M, and N are the material constants. Axis 1 is usually the rolling direction, 2 is transverse to the rolling direction, and 3 is collinear with the normal direction. Since the sheet has a property of plane stress ($\sigma_{33} = \sigma_{31} = \sigma_{23} = 0$), Hill48 can be modified in the 2D plane stress as the follows:

$$2f(\sigma_{ij}) \equiv (G + H)\sigma_{11}^2 - 2H\sigma_{11}\sigma_{22} + (H + F)\sigma_{22}^2 + 2N\sigma_{12}^2 = 1. \quad \textit{Equation 2.34}$$

For a numerical analysis with Hill48 to determine the material parameters and a flow stress in one direction, Lankford coefficients (anisotropic coefficients) r_0, r_{45}, and r_{90} are required. The flow stress is usually determined from the uniaxial tensile test in the rolling direction. The relationship between r_0, r_{45}, r_{90}, and F, G, H follows the following rules:

$$r_0 = \frac{H}{G}, \qquad\qquad\qquad \textit{Equation 2.35}$$

$$r_{45} = \frac{N}{F + G} - \frac{1}{2}, \qquad\qquad \textit{Equation 2.36}$$

$$r_{90} = \frac{H}{F}. \qquad\qquad\qquad \textit{Equation 2.37}$$

Hill48, which can be determined by the material parameters with a relatively small number of experiments, is reasonably well represented in a mild steel compared to those used in the experiment (Hill, 1948). However, it does not coincide much with other materials, especially aluminums or its alloys.

To overcome the limitations of Hill48, it has been developed as a yield function of Hill79 (Hill, 1979) and Hill90 (Hill, 1990). Hill90 overcomes the limitations of the previous models and has relatively a high flexibility to demonstrate a similar material behavior in various materials. However, since the formulation is not user-friendly, it is difficult to use the same for the numerical analysis and it is not efficient because of a high computational cost (Banabic, 2010). Hersford, Barlat, Banabic, and others have published their yield functions in an equation designed from Hershey models in a different system from the Hill models. Typically, Barlat and Lian proposed Barlat89 as a planar anisotropic yield function (Barlat and Lian, 1989). The function is expressed in Equations 2.38, 2.39 and 2.40:

$$f_{B89} = c|k_1 + k_2|^M + c|k_1 - k_2|^M + d|2k_2|^M = 2\sigma_e^M. \qquad \textit{Equation 2.38}$$

Here k_1 and k_2 are given by

$$k_1 = \frac{\sigma_{11} + h\sigma_{22}}{2}, \qquad\qquad \textit{Equation 2.39}$$

$$k_2 = \left[\left(\frac{\sigma_{11} - h\sigma_{22}}{2}\right)^2 + p^2\sigma_{12}^2\right]^{1/2}, \qquad\qquad \textit{Equation 2.40}$$

where c, d, h, p, and M are the material parameters. M is approximately determined by 6 for BCC materials and 8 for FCC materials, respectively. c, d, and h are identified based on the Lankford coefficients r_0 and r_{90} by the following equations:

$$c = 2 - d = 2 - 2\sqrt{\frac{r_0}{1 + r_0} \cdot \frac{r_{90}}{1 + r_{90}}}, \qquad\qquad \textit{Equation 2.41}$$

$$h = \sqrt{\frac{r_0}{1 + r_0} \cdot \frac{1 + r_{90}}{r_{90}}}, \qquad\qquad \textit{Equation 2.42}$$

where p is calculated by a numerical procedure. Barlat89 predicts the material behavior of the aluminum rather than a simple and strong anisotropic, requiring only four material constants. However, in order to obtain the material constant p, a nonlinear equation is solved. And the materials with the strong anisotropy and biaxial stress prediction generally do not agree.

For a continuous improvement, Barlat91, Barlat94, and Barlat96 have since been announced. Among them, Barlat96 shows a good agreement on the anisotropy coefficient and the stress in the uniaxial direction in the plastic material behavior of the aluminum alloy. However, the convexity of the yield function is not guaranteed, and the limitations that the derivative cannot be obtained analytically remain. (Barlat et al., 2003)

In order to secure the limitations so far, Barlat published Yld2000-2d on plane stress (Barlat et al., 2003). The yield function is defined by a linear transformation. This function requires a total of eight material constants, 3 uniaxial yield stresses, 3 anisotropic coefficients, a biaxial yield stress, and a biaxial anisotropic coefficient, to determine them. To obtain the eight material constants, the nonlinear equations must be solved and the procedure is given in Appendix 11.1. Yld2000-2d proved the convexity of the yield function by overcoming the disadvantages of the previous Barlat96 (Barlat et al., 2003).

Banabic et al. (Banabic et al., 2000) proposed own yield function named BBC2000 modified based on the isotropic yield function Hershey. BBC2000 and Yld2000-2d were compared with

Yld2000-2d and experimental measurements in normalized stresses and *r*-values according to angles from the rolling direction. The both yield functions analyzed accurate distribution of the *r*-values, but Yld2000-2d could predict more accurate distribution of the normalized stresses than BBC2000. The yield function was improved in order to take the biaxial anisotropic coefficient into account as follows (Banabic et al., 2005):

$$\sigma = [\alpha(\Gamma + \Psi)^{2k} + \alpha(\Gamma - \Psi)^{2k} + (1 - \alpha)(2\Lambda)^{2k}], \qquad Equation\ 2.43$$

where k ($\geq$ 1) and $0 \leq \alpha \leq 1$ are the material parameters. Γ, Ψ, and Λ are expressed as follows:

$$\Gamma = \frac{\sigma_{11} + M\sigma_{22}}{2}, \qquad Equation\ 2.44$$

$$\Psi = \sqrt{\left(\frac{N\sigma_{11} - M\sigma_{22}}{2}\right)^2 + Q^2\sigma_{12}\sigma_{21}}, \qquad Equation\ 2.45$$

$$\Lambda = \sqrt{\left(\frac{R\sigma_{11} - S\sigma_{22}}{2}\right)^2 + T^2\sigma_{12}\sigma_{21}}, \qquad Equation\ 2.46$$

where *M*, *N*, *P*, *Q*, *R*, *S* and *T* are also the material parameters.

BBC2005 comparing Yld2000-2d also needs eight material characteristics: 0°, 45°, and 90° uniaxial stresses and *r*-values, a biaxial stress, and a biaxial *r*-value. It was proved that the yield function Yld2000-2d and BBC2003 are the same, when $\alpha = 0.5$ (Barlat et al., 2006).

Yld2000-2d was expanded to a three-dimensional yield function in 2005 under the name Barlat2004-18p (Barlat et al., 2005). A total of 18 material constants were required to increase the complexity of the function. Therefore, the uniaxial stresses and anisotropy coefficients in seven directions must be measured. In addition, two simple shear stresses are required for the biaxial stress, the biaxial anisotropy, and four additional out-of-plane directions. Barlat2004-18p are difficult to use and too complex, and earing in the prediction of the parts produced in the cup drawing shows a high degree of accuracy in comparison with the experimental than the previous models (Yoon et al., 2007).

2.5 Deep drawing process

The bead forming follows the deep drawing process according to DIN 8584-3. In the deep drawing process, a thin sheet metal is drawn into a concave shaped tool. Three tools, a punch,

a blanking holder, and a die, are used for this purpose, and a schematic procedure for the deep drawing process with the three tools is shown in Figure 2.6. In addition, the deep drawing is carried out using the active media and the active energy instead of mechanical tools. The active media includes a gas or a fluid, and the active energy is applied to the electrohydraulic or the electromagnetic forming. It is possible to increase a dimensional accuracy or to avoid contact problems without the mechanical tools, but the conditions of using the active media and the energy are difficult, such as being a magnetic or requiring a very large capacitor.
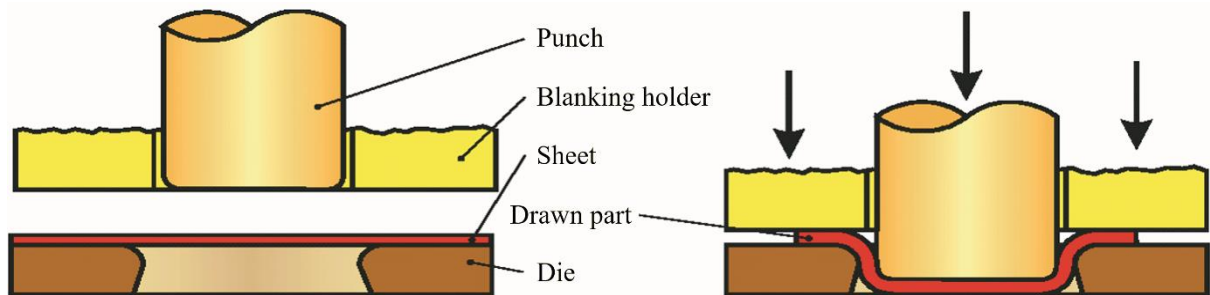
Figure 2.6: Deep drawing process with tools (Schuler, 1996)

2.6 Forming limit model

A deformation failure of the material during a sheet metal forming should be avoided. The deformation failure in the sheet metal forming has a local instability and a fracture. The local instability, called necking, is apparently not a problem with the shape of the part, but it significantly reduces the strength of the part. The fracture is developed from instability, which is why the object shape cannot be made due to the separation of materials. In order to analytically identify these failures, an additional model is needed to predict the local instability and fracture of the material as well as the yield function that can represent the plastic deformation of the metal. Most of them are used to predict the forming limit by using the internal values of the material, that is, strain and stress. It is used as a criterion for predicting the forming limit by the internal variable values at the time of material failure or by calculating the damage by a combination of internal variables by a specific principle and estimating the forming limit of the material by accumulated damage. In the former case, strain-based FLD and stress-based FLSD are representative examples. In the latter case, there are Cockcroft-Latham and Gurson models as damage models. Damage models are mainly used to predict material failure through damage accumulation rather than local instability. Therefore, this chapter examines various types of modeling prediction models for predicting the forming limits of metal sheet materials.

2.6.1 Strain-based model

2.6.1.1 Forming limit diagram

A curve has the maximum main strain values at material failure in FLD. This was first invented by Keeler (Keeler, 1961) and Goodwin (Goodwin, 1968). This concept requires major strains and minor strains at the material instability or the fracture. Normally, the values of the limit strain obtained from various planar deformation states, from the uniaxial tension to the biaxial tension, of the thin metal sheet form the forming limit curve (FLC). The Nakazima test is typically performed to obtain the limit principal strains. The Nakazima test draws a rectangular sample of various widths with a hemispherical punch and a circular die. The shape of the specimen conforms to the ISO12004 standard, and the punch diameter is recommended to be 100 mm. The punch draws the specimen, and the strain can be measured through the optical measuring system or the strain gauge until the fracture. In addition to the Marciniak test, the tensile test and the bulge test, a variety of deformations can be expressed through a tester to determine the state, but now through the Nakazima test to make FLD is the standard.

In the Nakazima test, it is challenging to obtain the limit strain at the point of necking when the plate is deformed until it breaks. This is because it is not easy to determine the exact limit strain value because the section from the material to the fracture after the necking is much shorter than the plastic strain section. Thus, several methods have been introduced to determine the limit strain. We introduced a decision method based on interpolation of the limiting strain called the three circle method developed by (Bragard et al., 1972). Once the material breaks, the strain values around the fracture center on the cross-section of the plane including the fracture are internally divided. The maximum value of the subdivided line is defined as the limit strain. In 1975, Hecker (Hecker, 1975) published another method of defining the limit strain. After the fracture, the surrounding oval shape was classified into three types: circle, fracture, quadrilateral due to the effect of necking or breaking, and triangle shape is classified as safe. However, with the development of the optical measurement system thereafter, the limit strains have appeared in a way different than before. It is known that the strain rate rapidly increases after the necking. A characterization point is defined where the strain rate changes rapidly over time as the strain measurement becomes possible in the real time. The intersection of the slope of the constant strain rate before the necking and the slope of the abruptly increased the strain rate is defined as the characterization point. The strain at this point is determined as the limit strain (Volk and Hora, 2011). Owing to the development of the optical measurement system,

Nakazima introduced a limit strain measurement method using a real-time interpolation. (Nakazima and Kikuma, 1967) This defines the marginal disease rate similar to that introduced by (Bragard et al., 1972).

Recently, a method using a camera is mainly used, and two methods of measuring a limit strain using a time graph versus a strain rate versus a limit strain measuring method based on an interpolation of a peripheral strain according to a position are used. These methods have been developed with several commercial tools, and ARAMIS is typically used (DIN EN ISO 12004-2).

The FLC is used to check material failure in advance in order to produce the parts in safely. This allows investigating the range in which parts are safely produced in deep drawing. In addition, it can assist in a process design by identifying where a necking or a fracture occurs frequently. It is possible to know which a limit strain occurs in a certain region. Four typical deformation states in a deep drawing are shown with the FLC for the necking and the crack in Figure 2.7. Deformation paths (1) - (4) are called the ideal deep drawing, the uniaxial tension, the plane strain, and the biaxial tension, respectively.

(1)	$\varphi_1 = -\varphi_2$	$\longrightarrow$	Ideal deep drawing
(2)	$\varphi_1 = -2\varphi_2$	$\longrightarrow$	Uniaxial tension
(3)	$\varphi_2 = 0$	$\longrightarrow$	Plane strain tension
(4)	$\varphi_1 = \varphi_2$	$\longrightarrow$	Biaxial tension
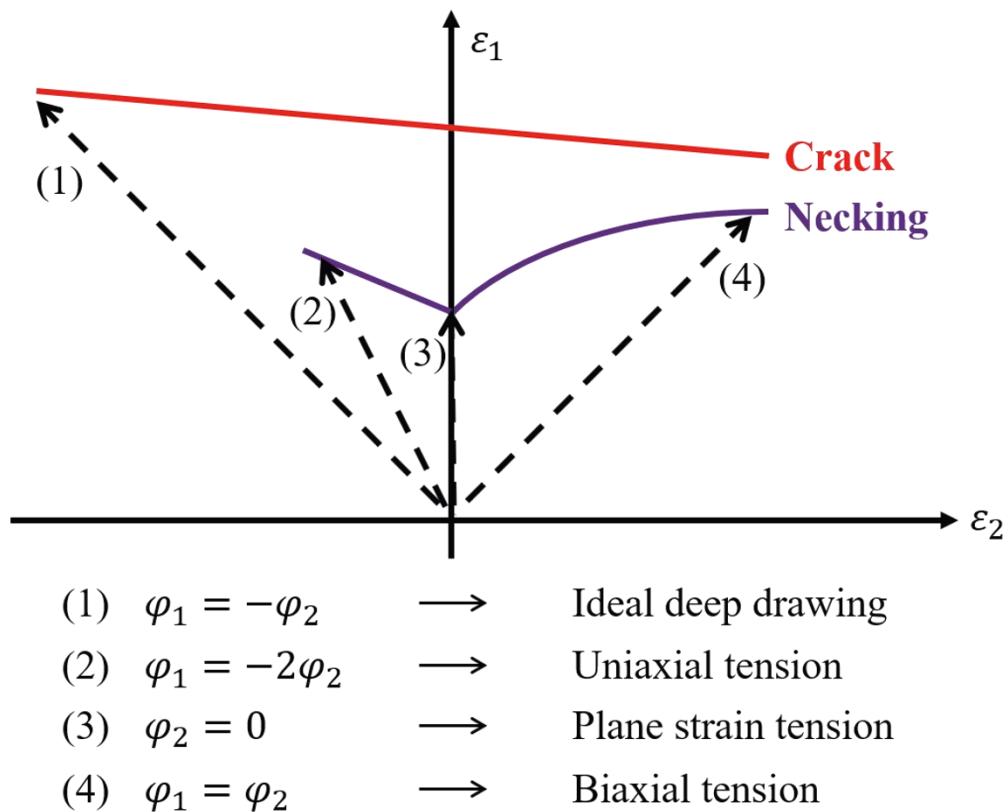
Figure 2.7: representative forming states in forming limit diagram

The FLD determined as above has the greatest advantage and can easily measure the material characteristics required for the experiment. Therefore, no additional numerical model is needed, so it is easy to identify the formability and improve the process conditions by a simple comparison after measuring the strain of the part. Unfortunately, the FLD cannot take into account nonlinear deformation paths. Therefore, it is difficult to predict the forming limit of a part made of a various deformation history by the FLD.

2.6.1.2 Generalized Forming Limit Concept

The traditional FLC is used to determine the forming limit of the material. However, the drawback of the traditional FLC is that it cannot predict the forming limit with almost the same linear and unbroken strain paths (Volk et al., 2012). Most of the automobile parts of the metal sheet are manufactured in many forming operations with the nonlinear strain paths. Generalized Forming Limit Concept (GFLC) was developed to overcome the limitations of the traditional FLC and to consider nonlinear strain paths. The GFLC has a posteriori material failure evaluation, which is the characteristic of the FLC, so it can be easily used in practice by the strain measurement.

To predict material failure in the GFLC, the failure behaviors are described in bilinear loading conditions as a function of a true strain ratio ($\beta = \varepsilon_2/\varepsilon_1$) and a true strain length $l(\beta)$ at a pre- and a post-forming based on the experimental data for the GFLC as shown in Figure 2.8.
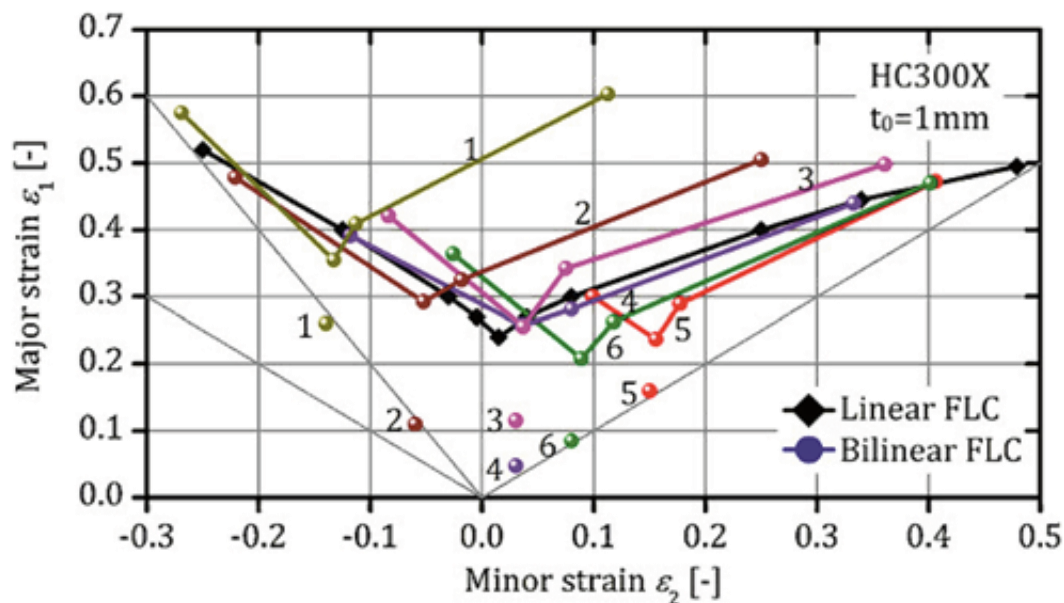
Figure 2.8: Experimental FLD for bilinear strain paths and six different pre-strains (Volk et al., 2012)

Six different pre-deformations are carried out under the uniaxial, the plane-strain, and the equibiaxial tensile states with the two different forming degrees. Six subsequent FLC from each pre-deformation are generated to determine the GFLC data for one material. The FLC of the linear strain path is obtained as a reference data. The unique strain length $l(\beta)$ is calculated by each strain ratio ($\beta = \varepsilon_2/\varepsilon_1$) at the beginning of the instability. The strain path length ratio λ_{pre} and λ_{post} of the pre- and post-forming are calculated corresponding to the strain ratio β_{pre} and β_{post}, respectively. In this way, a metamodel of the total strain path length ratio λ is built by the following equation:

$$\lambda = f\left(l_{pre}, \beta_{pre}, l_{post}, \beta_{post}\right)$$

$$= \lambda_{pre} + \lambda_{post} = \frac{l_{pre}(\beta_{pre})}{l_{FLC}(\beta_{pre})} + \frac{l_{post}(\beta_{post})}{l_{FLC}(\beta_{post})}. \qquad \textit{Equation 2.47}$$

Figure 2.9 shows an exemplary example for the parameterization of a bilinear strain path with the biaxial pre-forming.
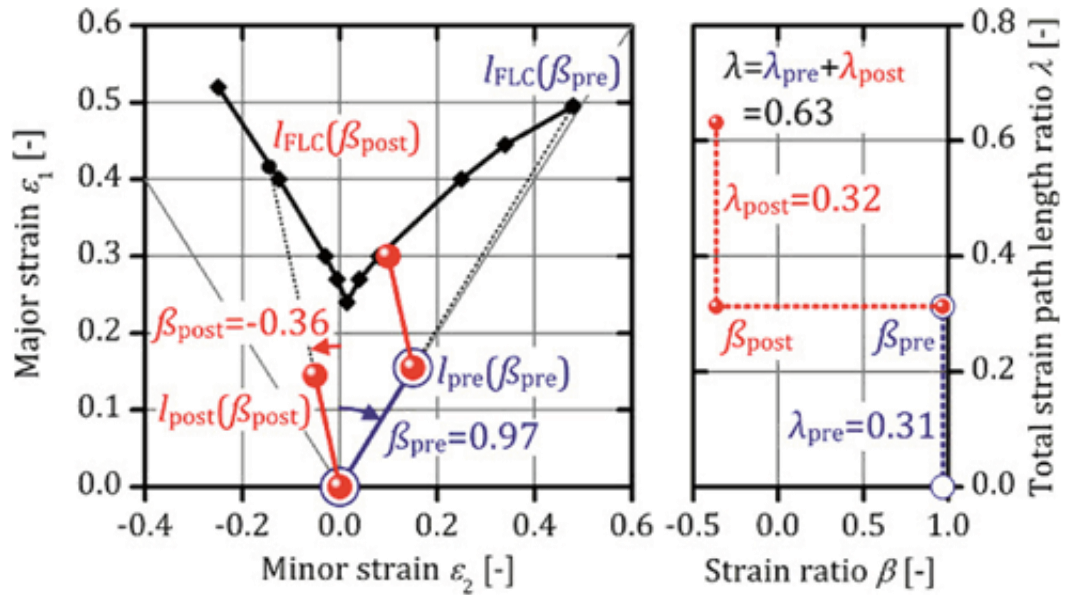
Figure 2.9: : Parameterization of a bilinear strain path with biaxial pre-forming ($\varepsilon_1 = 0.18$, $\varepsilon_2 = 0.167$, $\beta_{pre} = 0.97$) and uniaxial post-forming ($\varepsilon_1 = 0.12$, $\varepsilon_2 = 0.04$, $\beta_{post} = 0.36$) (Volk et al., 2012)

Based on the isotropic approximation using the transformation for the four-node Lagrange element of the FEM, the meta-modeling is carried out. The phenomenological approach for the bilinear deformation histories can be extended to arbitrary nonlinear deformation histories consisting of an unlimited number of individual strain increments. The "corrected" strain path

length ratio λ_{cor} is adopted as the following equation in order to that λ reaches always 1 (Volk and Suh, 2013):

$$\lambda_{cor} = \lambda_{pre} + \lambda_{dif} = \lambda_{pre} + \{1 - (\lambda_{pre} + \lambda_{post})\}$$
$$= 1 - \lambda_{post}.$$

Equation 2.48
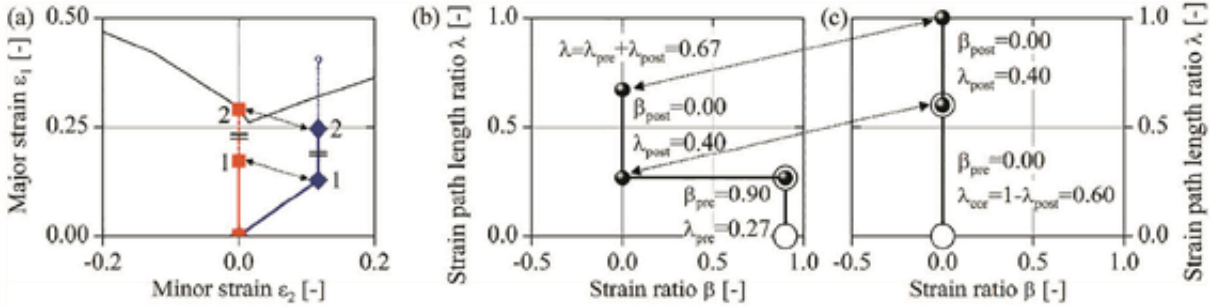
Figure 2.10: : Application of principle of equivalent pre-forming and modified parameterization with the fixed λ of 1: (a) equivalent pre-strain and post-strain in the plane strain direction at β_{pre}=0.90, λ_{pre}=0.27, β_{post}=0.00 and λ_{post}=0.40, (b) existing parameterization of bi-linear deformation history, (c) its linearization with a corrected strain path length ratio λ_{cor} (Volk and Suh, 2013)

It was investigated that the GFLC had a good agreement with an experimental local necking from various nonlinear strain paths generated by a cruciform specimen and a draw bead tool on a sheet metal testing machine, while the FLC had large errors (Jocham et al., 2017). The disadvantage of the GFLC is that the number of experiments required to make GFLC data of one material is more than the number of material tests required for the FLC or other forming limit models. The GFLC is a forming limit criterion based on the experimental strain measurements without an influence of material models. Therefore, it gives reliable results and is useful to evaluate the forming limit only with the strains in practice.

2.6.1.3 Analytical methods for FLC

The FLC is usually obtained through experiments. However, there are methods to obtain the FLC analytically instead of the experimental method. These are largely divided into two categories. Theories have been developed assuming that one is a homogeneous deformation and the other is a non-homogeneous deformation.

Assuming the homogeneous deformation, the Swift (Swift, 1952) and Hill (Hill, 1952) theories were constructed by dividing them into a diffusion necking and a local necking, respectively. Considère (Considère, 1885) confirmed that the load began to decrease from the necking, and the maximum force in the tensile test was indicated as the starting point of the necking. From

this, it is said that if the strain is equal to the hardening coefficient in the Ludwik-Holloman strain hardening equation, the necking begins. Swift extends from the uniaxial tension to the biaxial tension and allows for the calculation of the limit strain by the partial derivative of the yield function and the stress component for the stress component, and is defined by the Swift's model (Swift, 1952).

Hora and Tong proposed a model named 'Modified Maximum Force Criterion' (MMFC) based on the Considère's maximum force criterion (Hora et al., 1994). The derivation of a homogeneous stress condition and a strain rate ratio are used to predict the localized necking. The MMFC model can be used in any yield function with the stress ratio, equivalent stress and strain. Afterwards, an enhanced MMFC (eMMFC) model was announced in order to take into account the influence of a bending curvature and a sheet thickness (Hora et al., 2003). Some terms like curvature, thickness, young's modulus and other empirical parameters are added to the MMFC formula. The eMMFC model has advantages that are the assumption of the homogeneous stress and the consideration for the non-linear strain path. However, the prediction of the eMMFC model is dependent on the selection of a yield function and can need a numerical optimization to identify the empirical parameters for a new material.

The Swift's model is mainly valid for the diffusion necking, and a Hill's model was devised to calculate the limit strain at local necking. The yield function for the stress component and the Hill's model are made with the partial differentiation and hardening coefficients. Unlike the Swift's model, the Hill's model considers hardening coefficients. Thereafter, it was proposed by Stören and Rice to predict the occurrence of the localized necking in biaxial stretched plates (Stören and Rice, 1975). A vertex on the subsequent yield surface based on the J2 plasticity theory (Simo and Hughes, 1998) becomes more pointed during a deformation and causes a bifurcation from the uniform deformation. By the above methods, it is possible to predict the instability from the uniform deformation in the range of the uniaxial to the biaxial tension, and to calculate the limit strains.

The non-homogeneous deformation occurs due to the difference in the thickness of one material. A new model was proposed by (Marciniak and Kuczynski, 1967), analyzing the necking process of the material with different thicknesses, and is called the M-K model (Marciniak and Kuczynski, 1967). The schematic geometry for the M-K model is shown in Figure 2.11. The different thicknesses are referred to as regions A and B, respectively, and the region B has a lesser thickness than the region A. The interface of the two regions is perpendicular to the major direction 1 for the M-K model. The ratio of the thickness of one

specimen to another is called the coefficient of a geometrical non-homogeneity f_{nh}, and its value is ≤ 1.

Principal strains of $\varepsilon_1^{(A)}$ and $\varepsilon_1^{(B)}$ are obtained from the regions A and B, respectively, of different thicknesses under a biaxial deformation. As the deformation progresses, $\varepsilon_1^{(B)}$ increases close to infinity and the value of $\varepsilon_1^{(A)}$ at this time is designated as the limit strain. The M-K model is a valid method in the region where the minor strain ε_2 is positive. Hutchinson and Neale extended the M-K model to be used in regions where the minor strain ε_2 is negative and is called the H-N model (Hutchinson and Neale, 1979). By varying the angle of the interface between the two regions, the limit strains were calculated in all regions of the FLC. For the M-K and H-N models, the limit strain is calculated using the difference in thickness, and the value of the limit strain depends on the coefficient of geometrical non-homogeneity f_{nh}. The larger f_{nh}, the higher FLC is drawn (Chung et al., 2014). The FLC is also calculated differently depending on the hardening model and strain rate, as well as the anisotropic yielding function and parameters.
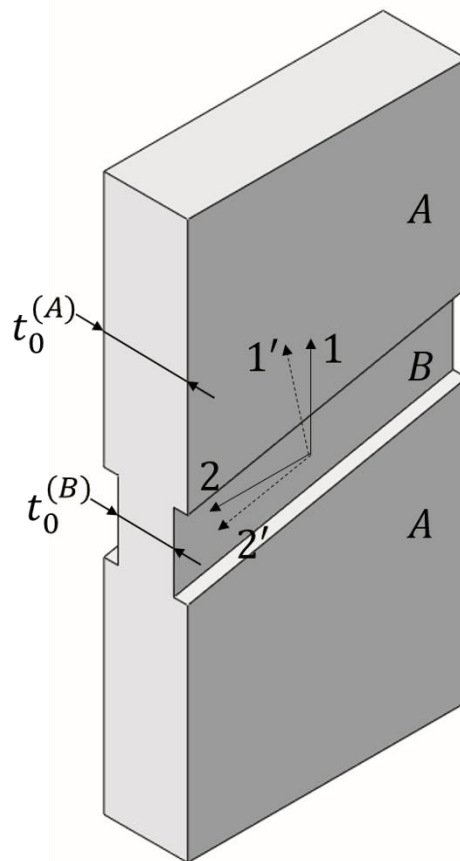
Figure 2.11:Simplified sheet with different thicknesses for M-K and H-N models

The analytical methods have continued to expand and evolve. The M-K model was combined with a general anisotropic yield criterion proposed by Karafillis and Boyce to calculate an analytical forming limit (Cao et al., 2000). The analytical forming limits were in a good agreement with an experimental FLC. The Stören and Rice bifurcation method attempts to determine a more general and improved FLD. For this, the left-hand side of the FLC can be obtained closer to the experimental value than the original model by using the optimization technique (Jaamialahmadi et al., 2012). Limit strains calculated by bifurcation analysis were well predicted in a biaxial stretching state for the rate-independent crystal plasticity model (Yoshida et al., 2012).

The theoretical FLCs can be obtained by the analytical methods. The theoretically obtained limit strains are sensitive to the strain path. In addition, it is difficult to obtain the limit strain values constantly by the user's selected yielding function or initial value.

2.6.1.4 Other prediction models for forming limit

FLC cannot accurately predict the material necking under nonlinear strain paths. The equivalent plastic strain limit is defined as the stress ratio of the stress ratio to predict the forming limit of the material regardless of the change in load paths (Yoshida et al., 2005). The only internal variable that can have a strain history under the assumption of isotropic material and isotropic hardening is the equivalent plastic strain. Thus, the necking can be predicted regardless of the strain path. A new strain-based forming limit criterion was proposed to predict the forming limit without getting affected by the nonlinear load path based on the equivalent plastic strain and the material flow direction at the end of forming (Zeng et al. 2008). The material flow direction is defined as the ratio of the principal strain rates. A polar diagram of the effective plastic strain $\bar{\varepsilon}_p$ was also proposed with the angle defined as the arctangent of the ratio of the principal strain rates $\dot{\varepsilon}_1$ and $\dot{\varepsilon}_2$ (Stoughton and Yoon, 2012). The polar diagram is called polar effective plastic strain diagram (PEPS). For various nonlinear strain paths, the PEPS is also insensitive. The related equations for the PEPS are expressed as the following.

$$(y, x) = (\bar{\varepsilon}^p \cos(\theta) , \bar{\varepsilon}^p \sin(\theta)) \qquad \qquad Equation\ 2.49$$

Where

$$\theta = \tan^{-1}(\dot{\varepsilon}_1, \dot{\varepsilon}_2) \qquad \qquad Equation\ 2.50$$

This model has an advantage to appeal the similar shape in comparison to that of the conventional FLC. Therefore, the directions of the uniaxial strain, plane strain, and equibiaxial

strain in the polar diagram are the same as those in the conventional FLC. It is easy to understand and easy to interpret the forming limit. Another advantage is that the stress-strain relationship is not necessary because of the strain-based forming limit. Since then, the PEPS implemented in commercial tools has been used in the tensile tests, automotive doorframes and beverage cans to confirm the reliability of nonlinear deformation paths (Dick et al., 2016).

Based on the plastic work that is calculated by a strain and stress, the fracture criterion was proposed considering nonlinear load paths (Clift et al., 1990). The criterion called Forming Limit Plastic Work (FLPW) was sometimes used as a predictor of forming limits independent of nonlinear deformation (Chung et al., 2014). The FLPW was extended to a criterion based on the plastic deformation energy for the prediction of the forming limit independent of various loads (Chen et al., 2010). This was used to confirm the forming limit of the automobile parts. The criterion based on the plastic deformation energy was also applied to limit strain prediction under the bilinear strain path. The FLPW can predict the forming limit under the bilinear strain path but has a difficulty to consider the stress-strain relation, since the stress is also needed to calculate plastic work for the FLPW.

Other strain-based methods to predict the forming limit under the bilinear strain path were also introduced, but they require the material model and theoretical understanding to calculate their own parameters. The prediction results can be differently obtained.

2.6.2 Stress-based model

In order to overcome the limitations of the FLC, which cannot predict the nonlinear path mentioned above, stress-based prediction of the forming limit was proposed by (Arrieux et al. 1981). Since then, stress-based criteria have rarely been mentioned for some time, and Stoughton announced again the need for stress-based criteria with computing speed and dynamic code development in FEM (Stoughton, 2000). Stoughton calculated the principal stresses of the material failure from the Hill quadratic and non-quadratic, and the Hosford's non-quadratic anisotropic model (Hosford, 1972) with the power law of hardening model. The calculation for the limit stresses takes the limit strains of FLC as input. Moreover, it can account into the pre-strains. Figure 2.12 shows how FLCs change depending on various pre-strains.

The dashed lines emanating from the origin show the pre-strain path for each condition, with the second leg showing the plane strain path of the secondary forming operation to the associated FLC. The FLCs with pre-strains are translated into principal stress plane to plot a FLSD. Figure 2.13 shows the independency of the FLSD on the pre-strains.
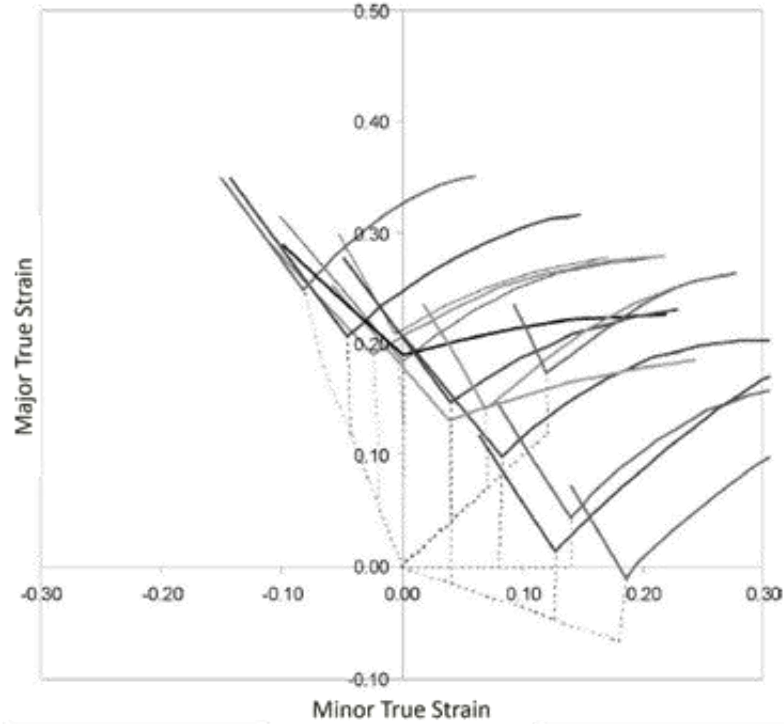
Figure 2.12: Dependency of FLCs after prestrain to several levels of strain in uniaxial, plane strain, and equibiaxial conditions (Stoughton and Zhu, 2004)
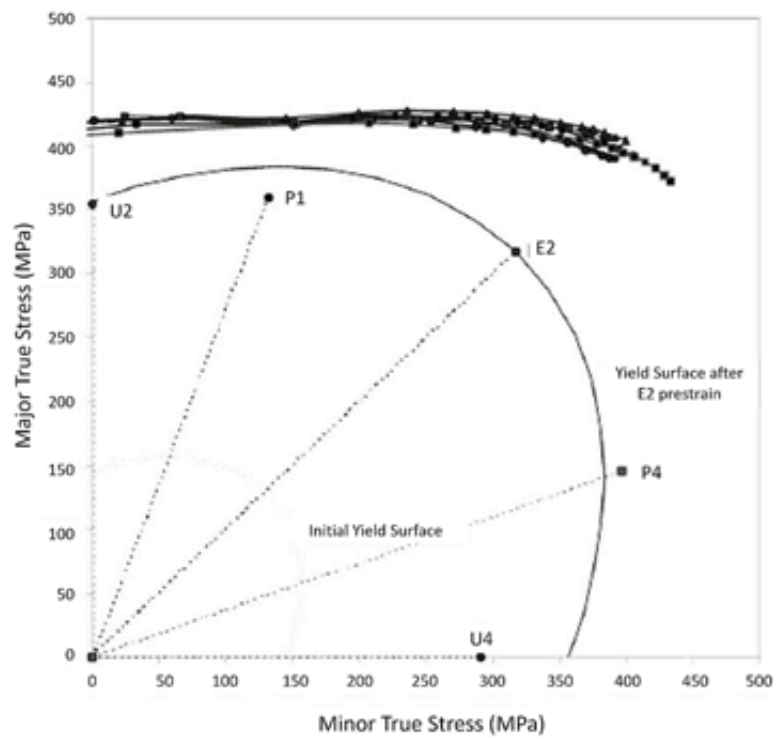
Figure 2.13: Yield surfaces depending on prestrain and path independency of FLSD using Hill's in-plane isotropic model with r = 0.58 (Stoughton and Zhu, 2004)

The limit stresses overlap in a similar region, which means that the FLSD can give coincident prediction of material failure under consideration of nonlinear deformation paths.

If the limit strain is not experimentally determined, the limit strain is obtained from the model that predicts the forming limit and translated to the stress space. From the Swift, Hill, Stören and Rice in the bifurcation analysis, or the M-K model as the damage model, the limit strain is calculated, and the FLSD is obtained by translating to the stress space (Stoughton and Zhu, 2004).

When complex models are used, a FLSD can be obtained with the FEM. The FLSD determined from Hill48 and an experimental FLC showed higher accuracy than predicting a material failure of the traditional FLC in the forming analysis of the automotive panel with the FEM (Chen et al., 2007). The M-K model, which can calculate the limit strains of a FLC, was used to obtain a FLSD for prediction of necking in the hydroforming process, in which a nonlinear loading path is shown (Hashemi, 2009). The FLSD generated using the M-K model predicted well the forming limit independent on combined loading with and without unloading (Yoshida et al., 2007). It was shown that a FLSD can be obtained using the GTN model to predict the nonlinear deformation of AA5052-O1. A FLC was also obtained and compared with the FLSD, and it was experimentally confirmed that the FLSD can consider nonlinear deformation (Min et al., 2011). A FLSD from Yld2000-2d and the Swift hardening model predicted more accurate forming limit of AHS steels than the FLSD from others (Panich et al., 2013). The FLSD was dependent not only on hardening and yield models, but also on material tests (Werber et al., 2013). This shows that the FLSD was significantly affected by the material models. An extended FLSD is proposed as another type of the FLSD. This plotted the FLSD in a plane that does not show limit stresses in the principal stress plane but has both hydrostatic stress and effective stress. This model is useful for use in processes such as a hydroforming where the pressure in the thickness direction is strong, depending on the thickness variation (Hashemi, 2014). The necking time by combining the finite element simulation with a ductile fracture criteria, named Cockcroft and Latham, was calculated, and a FLSD was created using the calculated strains at the necking (Kolasangiani et al., 2015). A forming limit stress calculation was simplified by the sheet thickness and a parameter Z that calculated using the ultimate tensile strength and uniform elongation from the uniaxial tensile test (Levi and van Tyne, 2016). This method calculated the forming limit stresses close to the FLSD based on the experimental FLD. The FLSD is used to predict the forming limits, taking into account various nonlinear loads and deformations. However, a complex formulas and a numerical analysis to determine the FLSD

could be required to improve accuracy of forming limit prediction. The FLSD strongly depends on the user's understanding of the model, the material tests, and the material models. It is difficult directly to validate the FLSD with the experiment because it is hard to measure the stress.

2.6.3 Conclusion

The many methods have been devised to overcome the inaccuracies of the traditional linear FLC predicting a material failures in nonlinear load paths. The analytical methods reduce the number of tests, but the complexity of the implementation is dependent on the model accuracy. The methods of predicting the material failures in nonlinear load paths in stressed space also depend on the material models, but it also lacks a direct model validation due to difficulties of the stress measurement. The GFLC is a material-model-independent, a strain-based prediction method that requires a relatively large number of experiments, but it is possible to directly validate the model by strain measurements. Thus, the material failures can be predicted with a higher accuracy and reliability than other different models. For this reason, in this study, the GFLC is used to predict the material forming limit in the bead forming where nonlinear load paths occur.

3   Objective

The location and the geometry of the bead are the decisive factors to effectively increase the stiffness of the sheet metal parts by the bead insertion. Numerical algorithms have been developed to optimize these effects in the last few decades, but they have not optimized geometries that take a material formability into account. A prediction model of the material forming limit can be additionally used in the forming simulation to predict the material forming limits in the deep drawing and the bead forming. Therefore, the purpose of this study is to provide a simulation technique that can guarantee the formability of the bead-formed parts while considering the forming limit of the material in bead optimization according to the bead locations and geometries to maximize stiffness. Firstly, the bead optimization procedure and required elements are arranged regarding to stiffening and formability. In this simulation technique, a forming history of the deep drawn parts should be considered to optimize the bead geometries considering the manufacturability. In general, the forming history in the deep drawing and the bead forming is nonlinear. Generalized Forming Limit Concept (GFLC) is used in this study as a forming limit model to consider the nonlinear forming history. The GFLC receives the major and the minor strains after each forming step as input values. The anisotropic yield model Yld2000-2d is used to describe the material behavior of the thin sheet metal as accurate as possible. This makes it possible to calculate the near realistic strain distribution and history and to improve the reliability of the forming limit prediction of the GFLC. The tension, bulge, and Nakazima tests are carried out to obtain the material characteristics in order to use the material model. The bead tools are constructed based on the trajectories determined by a stress distribution under a pin loading on the preformed part. The influence of the bead geometries on the formability and stiffness with the prepared models to reveal the relationship between the formability and stiffness. The database is created based on the relation of influential parameters to formability to guess an initial bead geometry for the effective optimization. The deep drawing as the preforming and the bead forming as the subsequent forming are experimentally performed to validate the reliability of the numerical studies with the simulation models. The bead tools are manufactured based on the determined bead locations and geometries. The strain values, the material failure, and the load-displacement curves in experiments are compared with the results of the simulation model. If the compared results show a good agreement, the numerical technique for the formability consideration is reliably established in the bead optimization. This research flow is summarized as a diagram in Figure 3.1.
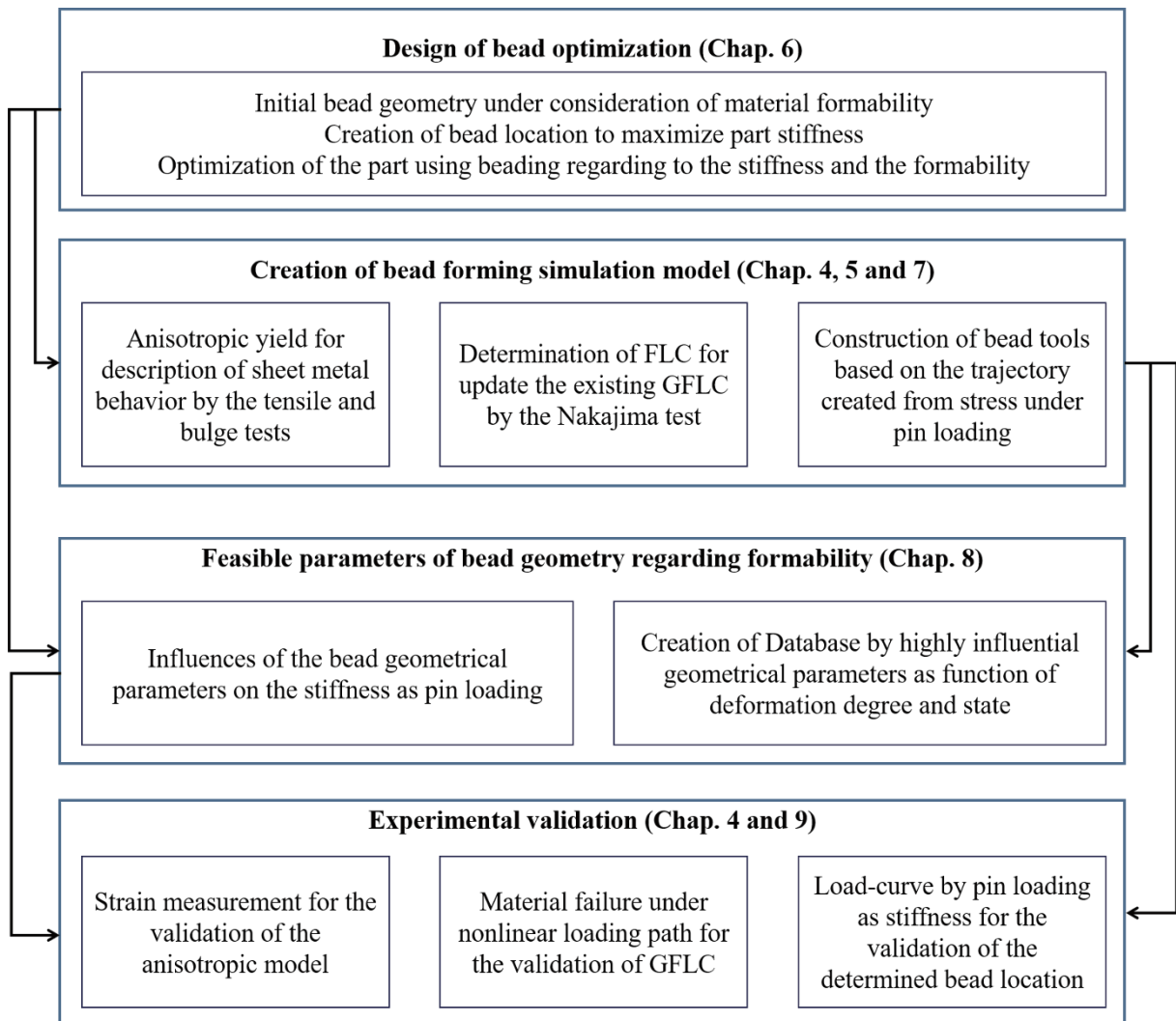
Figure 3.1: Diagram for research flow

4   Test facilities and measuring equipment

This section introduces experimental machines and measuring devices used in this study. In this study, the forming analysis is required to develop the bead optimization program. To use this, the material parameters that determine the parameters of the material model should be measured. The machines for the tension and bulge test are explained first. In addition, specimens for the material tests and the devices for measuring the strain of the deformed parts are introduced. Finally, a press machine is introduced that allows the parts to be formed directly.

4.1   Universal test machine

A universal test machine is used to determine the mechanical properties of the material. Quasi-static uniaxial tensile loads are used to obtain the stress values and the anisotropy coefficients, which are the material values required to determine the yield function. Equipment Typ 1484 / DUPS-M from Zwick GmbH & Co. KG. KG, Ulm is used as shown in Figure 4.1.

Figure 4.1: Universal test machine 200 kN

It operates up to a maximum load of 200 kN and can be deformed by the control of a displacement, speed, and the load unit. In order to measure the stress and strain, the tactile measuring equipment is necessary to measure the deformation in the direction of length and width. This is because, in the plastic deformation of metal, the deformation amount in the tensile direction and the width direction is measured using the property that the volume does not change, so that all the orthogonal deformations in three directions can be known. This allows the calculation of a true stress and strain as well as an engineering stress and strain. It also makes the measurement of the Lankford coefficient possible.

4.2   Sheet metal testing machine

The GFLC model is used for formability prediction. The conventional FLD is required first as experimental input data to use this model. In addition, the FLD should be made in a subsequent forming after a preforming of the uniaxial tension, plane strain, and equibiaxial tension. In this study, utg has the GFLC data of AA6016 and HC260LAD materials. However, the existing GFLC data is updated by replacing only the FLD with newly purchased material. To do this, a BUP-1000 machine as shown in Figure 4.2 is used to enable the FLD creation.

Figure 4.2: BUP-1000 with ARAMIS

The maximum deformation load and blank holding force up to 1000 kN is possible and enables a plane deformation of metal plates such as the Nakazima, Marciniak, and bulge test. A stroke, and load can be measured, and strains can be measured by combining with ARAMIS optical measurement system.

4.3   ARAMIS optical measurement system

The Nakazima test is typically performed to generate the FLD of the sheet material as shown in Figure 4.2. This test requires that the hemispherical punch draws samples with varying widths and measures the principal strain at the top center of the sample that is deformed into hemispheres. To do this, we use the non-contact optical 3D deformation measurement system GOM ARAMIS. The ARAMIS analyzes the deformation of the material surface under static and dynamic loads. The surface of the sample to be measured is sprayed so that any black dots can be placed on a white background. Two cameras take pictures of the stereoscopic 3D objects during the experiment at regular time intervals. It is recognized that the pattern of the sample surface changes and the strain position is measured and analyzed. We can calculate the strain and thickness changes by using the measured location values and analyze the limit strain for the FLD creation.

4.4   ARGUS

The ARGUS measurement system allows for the measurement and analysis of deformation results on the surface of the part as shown in Figure 4.3. High-resolution images capturing formed parts are evaluated with the ARGUS software. A point detection algorithm and mathematical calibration calculations automatically calculate precise models of light sections, camera position and lens distortion. This corresponds to a structure in which the 3D object coordinates of the component surface are aligned on a finely resolved network and applied to the semi-finished products. The network reflects the surface of the formed part.

From the 3D coordinates of the object point, the main strain and the negative strain, which are actual results of the shape change, are calculated. In addition, the sheet thickness is calculated taking into account the component geometry and the rules of plasticity theory. An optimization of the analytical model and comparative verification can be performed in practice. It can also find limit strain areas or suggest solutions to complex deformation problems. The strain measurement range is from 0.5 % to 300 % and the strain accuracy is up to 0.2 %. The

measurement range is from 100 mm^2 to m^2. In order to use the ARGUS, a recognizable pattern on the surface of the formed part must be printed and electrolytic marking is used for this purpose. The ARGUS compares the pattern changes before and after the forming of the parts to analyze the strain.
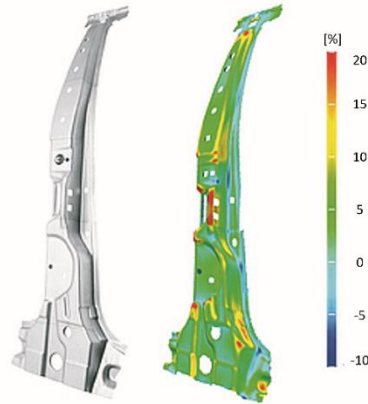
Figure 4.3: B-pillar example of ARGUS usage for strain measurement

4.5 Electrolytic marking

Products with an electrically conductive surface can be marked with the EU CLASSIC 300 devices of ÖSTLING GmbH. The marking is made by a current pulse, which is passed through the embossing of the template. This creates an exact image on the product to be marked. The surface shape of the product is arbitrary. The template used has an A3 size with a circle of 1 mm diameter and a spacing of 2 mm. This pattern is semi-permanently engraved on the surface of the test material and is used to measure strain using the ARGUS system. The electrolyte fluid 72 was used for this study through a specimen test by ÖSTLING GmbH for the electrical marking. This marking method is useful for measuring the amount of a deformation even after the bead forming on both sides because there is no influence of the lubricant used to lower the friction during the forming.
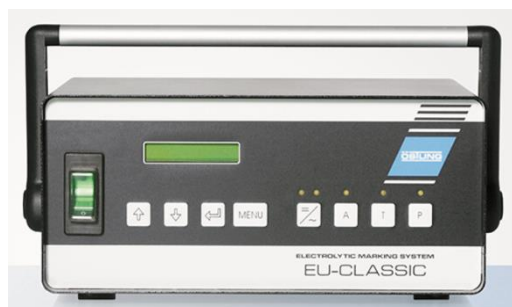
Figure 4.4: EU CLASSIC 300, ÖSTLING GmbH

4.6 Hydraulic press

An experimental validation is necessary to verify the forming analysis model used in the bead optimization program. The forming analysis model analyzes the deep drawing which is the preforming and the bead forming which is the post-forming. In order to perform these two processes, we need a hydraulic press to move the die and to create the selected part shape as an example. The Diffenbacher hydraulic press held in the utg as shown in Figure 4.5 is suitable for the purpose described and is used to manufacture the selected sample shape. The press has a maximum forming load of 3200 kN, a maximum blanking holding force of 1250 kN, a maximum stroke of 250 mm, and a working width of 1250 $\times$ 950 mm².

Figure 4.5: Diffenbacher hydraulic press

5   Test materials

Steels and aluminums are mainly used in sheet metals. Still, the steels have relatively high strength and ductility and are easy to form into complex design. In addition, the steels are an important material for manufacturing parts with high strengths. The aluminums have a lower strength and ductility than the steels, but it has a third of the steels density and plays a major role in a weight reduction in the automotive and aircraft industry. These two materials are considered to be the main materials in the automobile production. Among the various steels and aluminums, HX260LAD and AA6016 have no high strength compared to high-strength steels, e.g., DP steels and high ductility. They can be deformed without excessive load. For this reason, the two materials are suitable for confirming a reinforcement effect by the bead forming in an academic study. The two sheet metals have same thickness of 1 mm. The test materials are used in the material tests to identify the material parameters for the forming simulation, and in experimental validation to produce the parts by the preforming and the bead forming. The test materials are summarized in Table 5.1.

Table 5.1 Overview of test materials

Designation	Material standard	Sheet thickness [mm]
AA6016	DIN EN 573-3	1.00
HX260LAD	DIN EN 10292	1.00

Section 5.1 explains the general mechanical characteristics of the test materials. Section 5.2 explains the determination of the flow stress, which describes the isotropic hardening and obtains the directional stresses by material tests. Chapter 5.3 explains how to determine the Lankford coefficients for identifying the parameters of the material model. Section 5.4 describes the material test to obtain FLCs. The obtained results from the material tests will be used for the forming simulation and validation.

5.1   General mechanical characteristic

The 6016 aluminum (AA6016) is a 6000-series aluminum alloy (DIN EN 573-3, 2009). This involves a significant alloying with both magnesium and silicon, and the alloy is developed for a primary forming into products. The 6016 is the Aluminum Association (AA) designation for

this material. In European standards, it will typically be given as EN AW-6016. A96016 is the UNS number. Additionally, the EN chemical designation is AlSi1.2Mg0.4.

The mechanical property of the AA6016 has a density of 2.7 g/cm^3 and Young's modulus of 69 GPa, yield strength between 110 and 210 MPa, tensile strength between 200 and 280 MPa, and elongation between 11 and 27 % until fracture.

Ac-120, Ac-121, Ac122, and Ac-140 are a kind of AA6016. They are divided into a magnesium content and copper content. The Ac-120 and Ac-121 have approximately 0.4 wt% magnesium. The Ac-120 is a commonly used material, and the Ac-121 has improved bendability compared to the Ac-120. The Ac-122 and Ac-140 contain approximately 0.6 and 0.5 wt%, respectively. The Ac-122 and Ac-140 do not contain copper in common and had high strength. The general information of chemical composition of the AA6016 is shown in Table 5.2.

Table 5.2 Chemical composition of AA6016 (unit: by wt%)

	Si	Fe	Cu	Mn	Mg	Cr	Zn	Ti	Residuals
Max.	1.5	0.5	0.2	0.2	0.6	0.1	0.2	0.15	0.15
Min.	1.0	-	-	-	0.25	-	-	-	-

The detailed name of the test steel is HX260LAD + Z100MBO that is usually used for cold forming and has good formability in relation to high guaranteed yield strength. The steel HX260LAD belongs to the high-strength low-alloy (HSLA) steels that have a name of HC or HX according to the European standards (EN 10268: 2006 +A1 and 2013, EN 10346:2009). The HSLA has low carbon content (0.05 to 0.25% C) and manganese content up to 2.0%.

The zinc (Z) coating has a composition consisting almost entirely of zinc (>99 %) and is lead free, resulting in finely crystallized zinc spangle that meets high requirements for a visual appearance. Z100 of the name has a minimum total coating mass of 100 g/m^2 at both surfaces and a coating thickness of 7 μm per surface. The steel was rerolled with improved surface according to MB of the name. Furthermore, the test material was oiled as surface treatment, and a contact of the test steel with tools can basically be affected by undesired frictional defects such as scratch. The steel HX260LAD has a density of 7.8 g/cm^3 and Young's modulus of 210 GPa, yield strength between 260 and 330 MPa, tensile strength between 350 and 430 MPa, and elongation until fracture more than 26 %.

HX260LAD contains carbon, silicon, phosphorus, manganese, sulfur, titanium, niobium, and aluminum. The chemical compositions are summarized in Table 5.3.

Table 5.3 Chemical composition of HX260LAD (unit: by wt%)

	C	Si	Mn	P	S	Ti	Nb	Al
Max.	0.110	0.500	1.00	0.030	0.025	0.150	0.09	-
Min.	-	-	-	-	-	-	-	0.015

HC260LAD is not used as test material in the research but was used to generate GFLC data. As HC260LAD also belongs to HSLA, HC260LAD has similar chemical composition of HX260LAD as shown in Table 5.4. Only difference between HX260LAD and HC260LAD is the rolling condition. HX260LAD is not specified and HC260LAD is cold rolled steel. This difference can lead to the different formability. The mechanical properties of HC260LAD also are Young's modulus between 240 and 310 MPa, tensile strength between 340 and 420 MPa and elongation more than 27 %.

Table 5.4 Chemical composition of HC260LAD (unit: by wt%)

	C	Si	Mn	P	S	Ti	Nb	Al
Max.	0.100	0.500	0.60	0.025	0.025	0.150	0.09	-
Min.	-	-	-	-	-	-	-	0.015

The general material information of the test materials AA6016, HX260LAD and the used material HC260LAD is summarized. The steels HX- and HC260LAD show similar properties, however, the both material behaviors can be dependent on a delivery date, manufacturer and different additional process. Therefore, it is needed to identify the actual mechanical characteristic by experiments.

5.2 Flow stress

In order to know the isotropic hardening behavior of the sheet metal, the flow stress is obtained from the uniaxial tensile test or the bulge test. The uniaxial tensile test is performed based on (DIN EN ISO 6892-1, 2014). The tensile specimens are produced by a milling with H-type in (DIN 50125, 2004). The tensile specimens are prepared from 0° to 90° by 15° from the rolling direction. The deformation is measured in the length and width direction using a tactile extensometer. The deformation in the thickness direction can be calculated according to the volume constant during the plastic deformation. Thus, the true stress and the true strain are

calculated to determine the flow stress curve by the program TestXpert. These data are used as material characteristic values to use the anisotropic yield function.

The biaxial tensile flow stress is measured by the bulge test with the optical measurement system ARAMIS (DIN EN ISO 16808, 2014). There are two relevant meanings for measuring the biaxial tensile flow stress. One is to use a biaxial anisotropic coefficient as a material characteristic values for the anisotropic yield model Yld2000-2d (Barlat et al., 2003) used in this study. The other is to confirm the material behavior for a more elongation than the flow stress from the uniaxial tensile test. In the uniaxial tensile test, the flow curve of the steel up to an elongation of 20% is obtained and the subsequent behavior is calculated by an extrapolation (Volk et al., 2011). However, when the sheet is deformed in the plane direction by a certain pressure or load in the thickness direction, it is possible to make a deformation larger than the deformation by the uniaxial tensile test. Therefore, the flow curve of the material in the more elongation can be measured. The biaxial tensile stress curves for each material are shown in Figures 5.1 and 5.2, respectively.
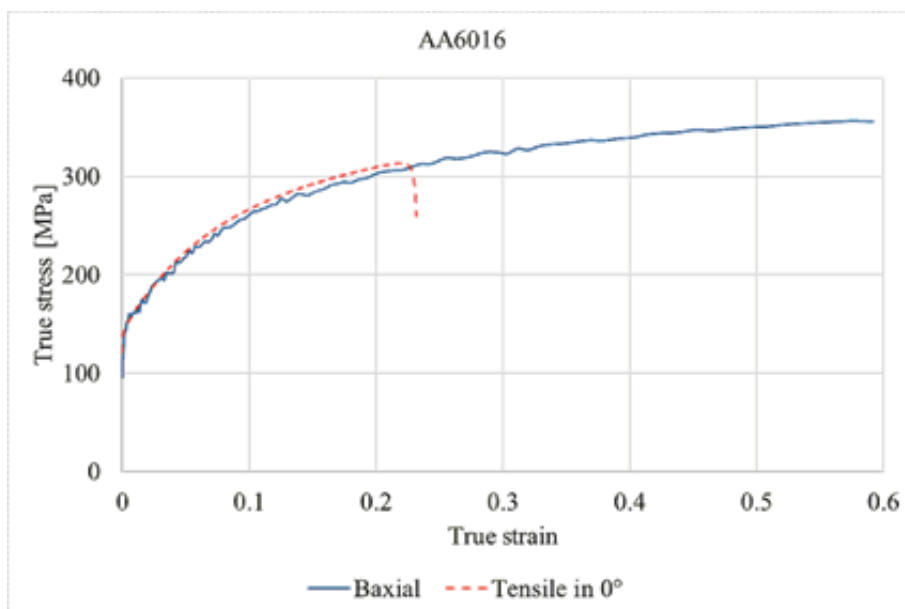
Figure 5.1: Flow stresses determined from the uniaxial tensile test with the specimen in the tensile direction of 0° and the bulge test for AA6016
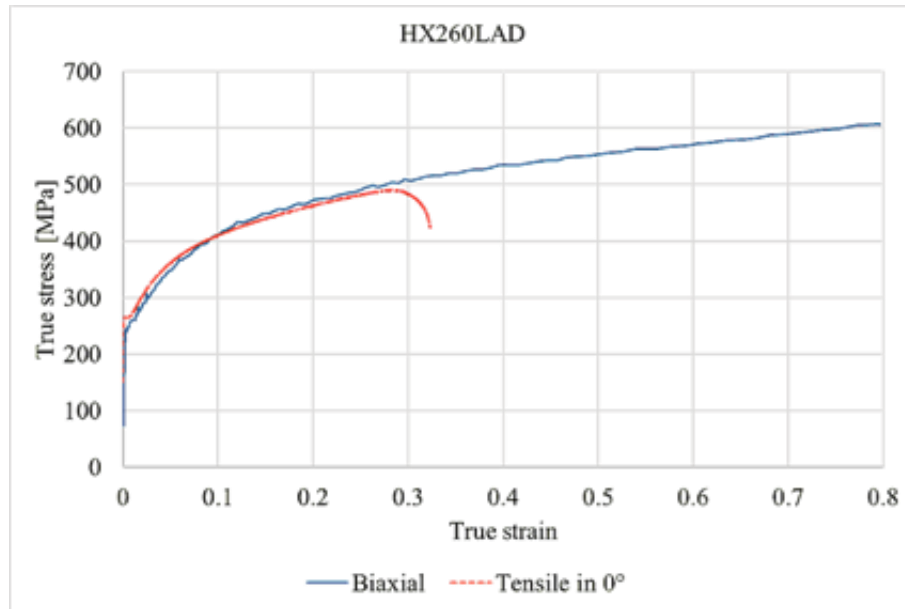
Figure 5.2: Flow stresses determined from the uniaxial tensile test with the specimen in the tensile direction of 0° and the bulge test for HX260LAD

The flow stress equations that agreed with the biaxial stress curves determined for ease of use in the numerical model are set. In order to flexibly match the experimental values, the flow stress equation was determined by a combination of Swift with the curve to increase and Hockett-Sherby with the curve to converge. The fitting curves are shown in the figure. The equation and the determined coefficients are as follows:

$$\sigma_{HC260LAD} = 675.2(0.0051 + \varepsilon^p)^{0.199} \ [MPa], \qquad \textit{Equation 5.1}$$

$$\sigma_{AA6016} = 0.1[412.8(0.0059 + \varepsilon^p)^{0.21}]$$
$$+0.9[369.5 - (369.6 - 146)\exp(-4.12\varepsilon^{p\,0.75})] \ [MPa]. \qquad \textit{Equation 5.2}$$

The stress values at 10% elongation for each direction are shown in Table 5.3. It is used as a material characteristic values to determine the parameters of the anisotropic yield function.

Table 5.3 Summary of normalized stresses for each material

	σ_0	σ_{15}	σ_{30}	σ_{45}	σ_{60}	σ_{75}	σ_{90}	σ_b
AA6016	1.000	0.960	0.949	0.970	0.972	0.980	0.977	1.003
HX260LAD	1.000	1.009	1.034	1.041	1.042	1.019	1.006	1.014

The flow stresses in different directions of the uniaxial and the biaxial tension are measured for the two test materials by the uniaxial and bulge tests, respectively. The stress measurements for these material behaviors are used to express the hardening and anisotropic properties of the sheet metal deformation.

5.3 Lankford coefficients

In the uniaxial tension and biaxial tension tests, not only a flow stress but also an anisotropic material behavior can be identified. The uniaxial tension test measures the anisotropy coefficient called the Lankford coefficient. This coefficient is defined as the ratio of the plastic strain to the transverse direction and the plastic strain to the thickness direction with respect to the tensile direction according to Equation 2.26.

Since the volume of the material does not change during the plastic deformation, a strain in the thickness direction can be calculated by measuring a strain in the tensile direction and a strain in the width direction. It is possible to measure all the strains in three orthogonal directions. A total of the seven directional specimens were produced up to 90° from 0° to 15° in the rolling direction. The prepared specimens were uniaxial stretched using the universal test machine, Zwick, and the anisotropy coefficients for each tensile direction were measured for the tensile strain according to the Lankford coefficient definition. Table 5.3 shows the Lankford coefficients by the tensile directions.

When the plate is deformed by the same load along both orthogonal axes on a plane, the amount of a deformation is not the same for the both axes. That is, anisotropic properties are exhibited even in a biaxial stretched state. In order to quantitatively express the behavior of these materials, the concept called biaxial anisotropy is defined. (Barlat et al., 2003) The mathematical definition is expressed as the ratio of strain to the both axes under the same load. One direction generally corresponds to the rolling direction, and the two directions refer to the vertical direction to the rolling direction. A disc compression test or bulge test may be used to maintain the same load or balanced biaxial stress state. In this study, the biaxial anisotropy coefficient was measured using the bulge test. The bulge test was carried out on the basis of (DIN EN ISO 16808, 2014) and the strain measured by the ARAMIS used to obtain the biaxial flow stress can be determined. The biaxial anisotropy coefficients calculated from the measured strain are plotted together with the uniaxial anisotropy factor in Table 5.4. All anisotropic coefficients were used as a reference for the equivalent strain of 0.1.

Table 5.5 Summary of normalized stresses for each material

	r_0	r_{15}	r_{30}	r_{45}	r_{60}	r_{75}	r_{90}	r_b
AA6016	1.29	1.14	1.01	0.95	1.03	1.38	1.58	0.80
HX260LAD	0.82	0.73	0.58	0.48	0.56	0.65	0.72	1.13

5.4 Forming limit curve

In order to predict the forming limit using the GFLC, a linear FLC is used as input. For each material, the FLC was performed according to the standard (DIN EN ISO 12004-1, 2008, DIN EN ISO 12004-2, 2008). For the Nakazima test, a sheet metal test machine BUP-1000, Zwick GmbH was used. The ARAMIS was used to measure the strain over time during the test. The punch speed was set at 1 mm/s and the blank holding force was set to 400 kN. The sample of the Nakazima specimen used is shown in the Figure 5.3.
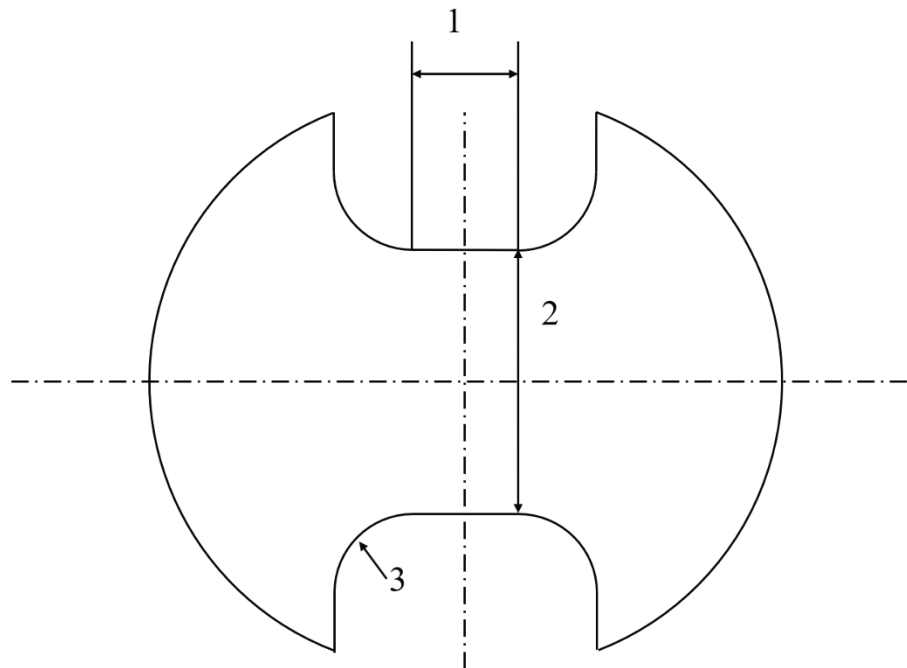
Figure 5.3: Geometry of Nakazima speciemen sample (DIN EN ISO12004-2)

In the figure 5.3, 1 is the length of the groove, 2 is the width of the cutting part, and 3 is the fillet radius, 20-30 mm. To measure the limit strain at various strain states, the width corresponding to 2 of the specimen shape was varied. The Nakazima specimens were used in seven different widths of 30, 50, 60, 90, 125, 150, and 235 mm and the specimens were

fabricated by a laser cutting. The specimens were sprayed with random black spots on a white background on the surface to be measured by the ARAMIS for an accurate measurement.

The limit strain, at which the local necking occurs, is determined based on the change of strain rate (Volk and Hora, 2011). The method is based on the observation that the beginning of the necking is accompanied by a considerable increase in the strain rate. According to this method the start necking point corresponds to the dramatic changes in the strain-rate versus time variation (characteristic point). This point could be determined by the intersection of the two straight lines corresponding to the first and the last sector of the curve (Figure 5.4). The strain-rate evolutions are automatically determined by the images analysis.
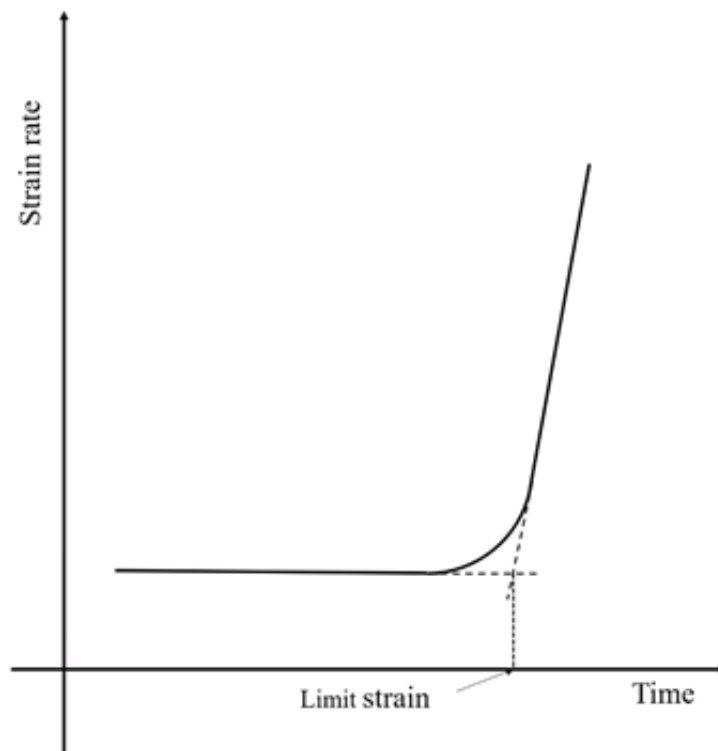
Figure 5.4: Strain-rate versus time

6   Bead optimization

In order to develop the bead optimization program under considering the material formability, the procedure for the bead optimization is built as shown in Figure 6.1. The process consists of modules in order to develop the systematic program.
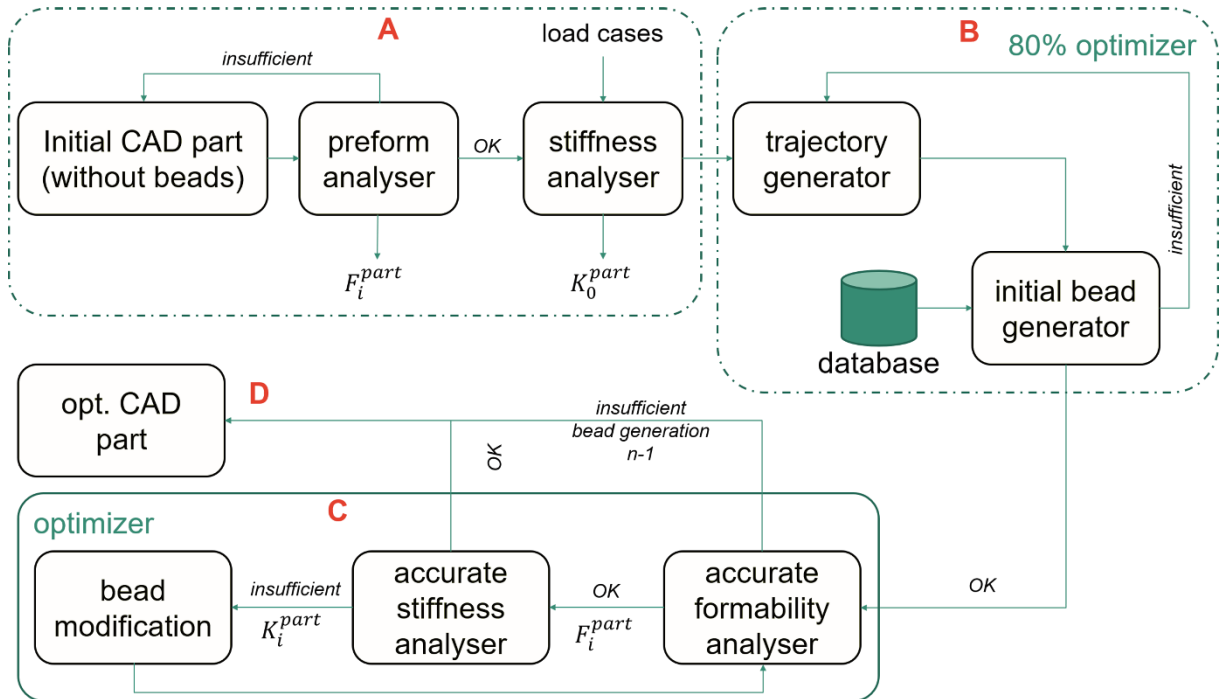
Figure 6.1: Procedure diagram for the bead optimization

First, the CAD file of the part designed without the bead is input at the CAD part. In the preforming analyzer, the blank is preformed to the designed part by the forming simulation. In addition, the basic feasibility of the preformed part as the GFLC value of the part F_i^{part}. If the basic feasibility is insufficient, the initial geometry of the part is modified and the feasibility of the part F_i^{part} is iteratively calculated. The preformed part otherwise goes to the stiffness analyzer. The stiffness analyzer carries out the forming simulation for the user-defined load case. The load case can be a vertical loading, bending, torsion and others depending on a required stiffness. The A-stage gives the feasibility F_i^{part} of the preformed part without beads, the initial analyzed stiffness of the part K_0^{part}, and the internal variables like coordinates, strains, stresses to the B-stage. The stress distribution results from the stiffness analyzer are used to generate the trajectory that is the optimal bead locations induced from the major bending stress vectors. The initial bead geometry on the generated bead location is modeled based on the database that takes the strain distribution from the preform analyzer in the A-stage. The relationship between the material formability and the bead geometry prepares the database in

advance. The initial bead geometry is close to the forming limit of at least up to 80 % level. The B-stage transfers the optimal bead locations and the initial bead geometries to the C-stage. The bead forming simulation and the forming limit analysis with the determined bead location and geometry are then carried out in an accurate formability analyzer. The accurate formability analyzer carries out the bead-forming simulation and the forming limit analysis with the optimal bead locations and geometries and calculates the feasibility F_i^{part}. If F_i^{part} is less than the forming limit F^{lim}, the stiffness of the bead-formed part K_i^{part} is confirmed by the user-defined load case at the accurate stiffness analyser. If the feasibility and stiffness of the bead-formed part satisfies the defined convergence criterion, the C-stage outputs the optimized part to the D-stage. The program ends the optimization process at the D-stage. If not, the bead geometry is modified and the stiffness and formability analyzed again until the criteria are satisfied.

The program has two convergence criteria. One is the target stiffness K^{target} defined by the user and the other is the forming limit F^{lim} according to the material. The criteria follow the Kuhn-Tucker condition. One of the both criteria should be satisfied, and the detailed conditions are described in the following equations (Cha et al., 2018):

$$\left(K^{target} - K_i^{part}\right)\left(F_i^{part} - f^{safe}F^{lim}\right) = 0, \qquad \text{\textit{Equation 6.1}}$$

$$\left(K^{target} \geq K_i^{part}\right), \qquad \text{\textit{Equation 6.2}}$$

$$\left(F_i^{part} \leq f^{safe}F^{lim}\right). \qquad \text{\textit{Equation 6.3}}$$

where f^{safe} is the safety factor and can set the forming limit criterion to 80 or 90 % considering statistic errors.

When a K_i^{part} is less than or equal to the K^{target}, the maximum stiffness of the K_i^{part} is resulted satisfying the Equation 6.3. When a K_i^{part} is more than or equal to the K^{target}, the minimum feasibility of the F_i^{part} is resulted satisfying that the K_i^{part} is equal to the K^{target}. The convergence criteria can be expressed in the following Equation 6.4 (Cha et al., 2018):

$$if \begin{cases} K^{target} \geq K_i^{part} : \max\{K_i^{part} | F_i^{part} \leq f^{safe}F^{lim}\} \\ K^{target} \leq K_i^{part} : \min\{F_i^{part} | K^{target} = K_i^{part}\} \end{cases}. \qquad \text{\textit{Equation 6.4}}$$

Here K^{part} and K^{target} are the analyzed stiffness and the target stiffness of the bead-formed part, respectively. If the user already knows the stiffness value with the unit of N/mm or kN/mm, the user can defines the K^{target} as the stiffness value. If not, the user gives the scale factor how the target stiffness is more than the stiffness of the preformed part in the stiffness analyzer. The second criterion consists of the F^{part}, f^{safe}, and F^{lim} that are the formability, safety factor and material forming limit of the bead-formed part, respectively. The F^{bead} is the calculated value of the GFLC depending on the material. The F^{lim} has the GFLC value of 1.0 for any materials. Since the initial bead geometry can have approximately 80 % of the formability, the f^{safe} has a value between 0.8 and 1.0. Therefore, the formability criterion depends on the material and the f^{safe}.

A forming simulation model is needed to be prepared for preforming, bead forming, and stiffness analysis in order to perform the aforementioned optimization. A material model and an FE-model are used for this. Generalized Forming Limit Concept (GFLC) is used for formability analysis. This model accurately determines the formability of the sheet metal forming considering the strain history with a nonlinear path than the conventional linear FLC. A database to suggest the initial bead geometry is prepared in advance by means of the sensitivity analysis with the simulation.

7   Forming simulation model

For the bead optimization, a forming simulation model capable of the preforming, the bead forming, and the stiffness analysis is required. The model for the formability prediction is used to prepare the database in the bead optimization to give the initial bead geometry, and to predict the formability of a determined bead position and geometry. Based on the calculated stress distribution after the preforming and the stiffness analysis, the bead path to maximize the stiffness is determined, and the bead geometry is determined from the strain distribution after the preforming to the forming limit before the bead forming. Therefore, it is required that the forming simulation model should accurately provide the stresses and strains as input values to the next step necessary for the bead optimization.

The material model plays a major role in the accuracy of stresses and strains. The test materials are thin sheet metals with anisotropy. This is because the material has planar anisotropic properties, and an anisotropic yield model capable of expressing it is required. There are several anisotropic yield functions, among which the Yld2000-2d model is selected. The Yld2000-2d was developed not only for steel, but also for the aluminum alloy sheet (Barlat et al. 2003), so it is suitable for analyzing the test materials AA6016 and HX260LAD used in this study. This tries to improve the accuracy of the forming analysis model by considering the non-AFR, which can express the strong anisotropic material behavior more flexibly. The implementation for the Yld2000-2d is described to use in the commercial FE-Software Abaqus mentioned in Section 7.1.

The GFLC model for the analysis of the formability requires history of major and minor strain in all processes. (Volk et al. 2012) have generated the GFLC data for AA6016 and HC260LAD. However, the materials used in this study are HX260LAD and AA6016. HC260LAD and HX260LAD are the same series of materials, but there is only a difference. In addition, AA6016 used has an aging effect over time as it produces the GFLC data. The GFLC model, which is retained to efficiently reflect changes in the same system or materials with aging effects, must be updated. The GFLC requires materials with two types of preparation: linear FLC and nonlinear strain paths. However, only the linear FLC is updated to that of the current material so that the determined GFLC is corrected. The GFLC model modification according to the general FLC test results for the test materials for this is described in Section 7.2. The updated GFLC is also introduced because of the differences with the linear FLC. Later, an experimental validation confirms the accuracy and flexibility of the GFLC.

The anisotropic yield function is implemented as a user-defined subroutine to the finite element model in Abaqus. The finite element model includes geometries of the dies and specimens, and boundary conditions considering preforming, bead forming or load case for the stiffness analysis. The GFLC for the forming limit prediction is used in conjunction with the Abaqus program, and such descriptions are mentioned in Section 7.3. When all of the above procedures are fulfilled, the establishment of the simulation models satisfying the requirements of this study is completed.

7.1 Material model

The anisotropic material model for the forming simulation is introduced. The model has two versions of the AFR and non-AFR, respectively, and then it is implemented in the commercial FEM software using a stress integration algorithm. The verification is carried out by comparing the theoretical and experimental values. In addition, it is also compared with the anisotropic model in commercial tools to support the validity of the selected model.

7.1.1 Introduction of Yld2000-2d

The yield function Yld96 before the Yld2000-2d does not guarantees the proof of the convexity for the yield surface (Barlat et al. 2003). This is an important condition for solving plastic deformation by numerical analysis to obtain a unique solution. The Yld2000-2d overcame the proof of the convexity and improved the accuracy in the equibiaxial state. In addition, it is a model that can express the yield stress and anisotropy coefficient in rolling, diagonal, transverse and biaxial tensile stresses well. The Yld2000-2d yield function has a linear transformation of two unconditionally convex functions and a deviatoric stress tensor.

$$\phi_y = \left[\frac{1}{2}\left(\phi' + \phi''\right)\right]^{\frac{1}{a}},$$
Equation 7.1

where

$$\varphi' = |X_1' - X_2'|^a, \varphi'' = |2X_2'' + X_1''|^a + |2X_1'' + X_2''|^a,$$
Equation 7.2

where $X_{1,2}'$ and $X_{1,2}''$ are the principal values of linear transformation on the stress tensor. a is a material exponent and generally has a value of 6 for BCC and 8 for FCC, respectively, based on the crystallographic structure. The linear transformation of $\widetilde{\mathbf{X}}'$ and $\widetilde{\mathbf{X}}''$ can be made by the deviation function $\mathbf{s}$.

$$\begin{bmatrix} \tilde{X}'_{xx} \\ \tilde{X}'_{yy} \\ \tilde{X}'_{xy} \end{bmatrix} = \begin{bmatrix} C'_{11} & C'_{12} & 0 \\ C'_{21} & C'_{22} & 0 \\ 0 & 0 & C'_{66} \end{bmatrix} \begin{bmatrix} s_{xx} \\ s_{yy} \\ s_{xy} \end{bmatrix}, \qquad\qquad \textit{Equation 7.3}$$

$$\begin{bmatrix} \tilde{X}''_{xx} \\ \tilde{X}''_{yy} \\ \tilde{X}''_{xy} \end{bmatrix} = \begin{bmatrix} C''_{11} & C''_{12} & 0 \\ C''_{21} & C''_{22} & 0 \\ 0 & 0 & C''_{66} \end{bmatrix} \begin{bmatrix} s_{xx} \\ s_{yy} \\ s_{xy} \end{bmatrix}, \qquad\qquad \textit{Equation 7.4}$$

where $\mathbf{C}'$ and $\mathbf{C}''$ are linear transformation matrices. Alternatively, using the transformation $\mathbf{T}$, which transforms the deviation stress into Cauchy stress, the following relationship can be obtained:

$$\tilde{\mathbf{X}}' = \mathbf{C}'\mathbf{s} = \mathbf{C}'\mathbf{T}\boldsymbol{\sigma} = \mathbf{L}'\boldsymbol{\sigma}, \qquad\qquad \textit{Equation 7.5}$$

$$\tilde{\mathbf{X}}'' = \mathbf{C}''\mathbf{s} = \mathbf{C}''\mathbf{T}\boldsymbol{\sigma} = \mathbf{L}''\boldsymbol{\sigma}, \qquad\qquad \textit{Equation 7.6}$$

and

$$\mathbf{T} = \begin{bmatrix} 2/3 & -1/3 & 0 \\ -1/3 & 2/3 & 0 \\ 0 & 0 & 1 \end{bmatrix}. \qquad\qquad \textit{Equation 7.7}$$

The vectors $\tilde{\mathbf{X}}'$ and $\tilde{\mathbf{X}}''$ of the linear transformation can be directly related to the Cauchy stress tensor and the anisotropy parameters $\mathbf{L}'$ and $\mathbf{L}''$. The anisotropy parameters $\mathbf{L}'$ and $\mathbf{L}''$ can be expressed as:

$$\begin{bmatrix} L'_{11} \\ L'_{12} \\ L'_{21} \\ L'_{22} \\ L'_{66} \end{bmatrix} = \begin{bmatrix} 2/3 & 0 & 0 \\ -1/3 & 0 & 0 \\ 0 & -1/3 & 0 \\ 0 & 2/3 & 0 \\ 0 & 0 & 1 \end{bmatrix} \begin{bmatrix} \alpha_1 \\ \alpha_2 \\ \alpha_7 \end{bmatrix}, \qquad\qquad \textit{Equation 7.8}$$

$$\begin{bmatrix} L''_{11} \\ L''_{12} \\ L''_{21} \\ L''_{22} \\ L''_{66} \end{bmatrix} = \frac{1}{9} \begin{bmatrix} -2 & 2 & 8 & -2 & 0 \\ 1 & -4 & -4 & 4 & 0 \\ 4 & -4 & -4 & 1 & 0 \\ -2 & 8 & 2 & -2 & 0 \\ 0 & 0 & 0 & 9 & 9 \end{bmatrix} \begin{bmatrix} \alpha_3 \\ \alpha_4 \\ \alpha_5 \\ \alpha_6 \\ \alpha_8 \end{bmatrix}, \qquad\qquad \textit{Equation 7.9}$$

If the independent anisotropy parameters α_k (for k from 1 to 8) is all 1, the yield function can express the isotropic material behavior. The principal values of $\widetilde{\mathbf{X}}'$and $\widetilde{\mathbf{X}}''$ are expressed as follows.

$$X_1 = \frac{1}{2}\left(\tilde{X}_{xx} + \tilde{X}_{yy} + \sqrt{\Delta}\right),$$
Equation 7.10

$$X_2 = \frac{1}{2}\left(\tilde{X}_{xx} + \tilde{X}_{yy} - \sqrt{\Delta}\right),$$
Equation 7.11

$$\Delta = \left(\tilde{X}_{xx} - \tilde{X}_{yy}\right)^2 + 4\tilde{X}_{xy}^2.$$
Equation 7.12

Eight experimental results are required to determine the eight anisotropy parameters. The eight required experimental values are determined by the yield stress and Lankford coefficients of the rolling, diagonal, transverse, and biaxial tensile stress states. The anisotropic parameter identification procedure requires the use of the Newton-Raphson iteration with the measured eight experimental results. The identification procedure is described in Appendix 11.1.1.

7.1.2 Yld2000-2d with non-associated flow rule

So far, the Yld2000-2d has been briefly introduced based on the AFR. Here, the non-AFR is introduced to can express complicated anisotropy more precisely. In the non-AFR, the plastic potential function to determine the direction of the plastic strain rate and the yield function to determine the yield stress are defined differently. The direction of the plastic deformation rate in the non-AFR is also different from the vertical direction of the yield function in the AFR. The plastic strain rate by the flow rule is expressed by the following equation:

$$\dot{\boldsymbol{\varepsilon}}^p = \dot{\gamma}\frac{\partial \phi_p}{\partial \boldsymbol{\sigma}}$$
Equation 7.13

where ϕ_p is the plastic potential function of the Yld2000-2d. The potential function can have any formulations. In this study, the potential function has the same formulation of the yield function Yld2000-2d. The yield function and the potential function have different set of anisotropy parameters. Since the Yld2000-2d requires eight anisotropy parameters, the non-AFR version of the Yld2000-2d requires a total of 16 independent anisotropy parameters. In order to identify the parameters, the yield stresses and Lankford coefficients at every 15° from the rolling direction and the balanced biaxial state are measured from the uniaxial tensile test

and the bulge test. The measured directional yield stresses (σ_0, σ_{15}, σ_{30}, σ_{45}, σ_{60}, σ_{75}, σ_{90}, and σ_b) are used to identify the anisotropy parameters for the yield function. The measured directional Lankford coefficients (r_0, r_{15}, r_{30}, r_{45}, r_{60}, r_{75}, r_{90}, and r_b) are used to identify the anisotropy parameters for the potential function (Safaei et al., 2015). The yield function (ϕ_y) and the potential function (ϕ_p) are described in Equations 7.14 and 7.15, respectively:

$$\phi_y = \phi_y(\alpha_{1-8}),$$

Equation 7.14

$$\phi_p = \phi_p(\beta_{1-8}).$$

Equation 7.15

The 16 anisotropy parameters in Yld2000-2d with the non-AFR are optimized by minimizing an error function defined as the difference between the analytical and experimental values. The identification procedure is detailed in Appendix 11.1.2.

More anisotropic parameters of the non-AFR increase the complexity of the model, but the more complicated anisotropic materials can be expressed flexibly by the non-AFR. As a result, it is expected that materials having any anisotropic behavior can be expressed in a similar manner to the actual ones.

7.1.3 Stress integration algorithm for implementation of yield function

The commercial program used for the forming simulation in this study is Abaqus. Abaqus is a commercial FEM program that allows various simulation methods, compatibility with other programs, and user-defined subroutines. However, Abaqus does not have the yield function Yld2000-2d and needs an implementation of it using a user material subroutine written in FORTRAN. The user material subroutine VUMAT is used to implement Abaqus/Explicit. In order to do this, the stress integration algorithm is explained and applied to VUMAT (Dassault System, 2012).

The basic material model characteristic to represent the test material is elasto-plastic deformation. The problem of the elasto-plastic deformation is usually considered to be a strain-driven problem. The strain tensor is treated as the main variable and has the relationship with the stress tensor. The yielding is checked based on the stress tensor driven from the strain tensor. That is, the stress depends on the strain, and the yielding is determined in the stress space. If the relation can be expressed in a mathematically. First, it is assumed that the total strain can be expressed by the sum of the elastic strain and the plastic strain as shown in Equation 7.16:

$$\Delta \boldsymbol{\varepsilon} = \Delta \boldsymbol{\varepsilon}^e + \Delta \boldsymbol{\varepsilon}^p, \qquad \qquad \text{\textit{Equation 7.16}}$$

where Δ means an increment. The increment expression can be replaced by the rate. The two terms have no difference in infinitesimal deformation. In this study, all deformation in FEM is assumed as infinitesimal deformation. The superscripts *e* and *p* mean elastic and plastic, respectively. The definition of the elastic strain is described as follows:

$$\Delta \boldsymbol{\varepsilon}^e = \Delta \boldsymbol{\varepsilon} - \Delta \boldsymbol{\varepsilon}^p. \qquad \qquad \text{\textit{Equation 7.17}}$$

The plastic strain tensor is defined by the AFR as the relationship between the equivalent plastic strain increment $\Delta \boldsymbol{\varepsilon}^p$ and the plastic multiplier $\Delta \gamma$ as follows:

$$\Delta \boldsymbol{\varepsilon}^p = \Delta \gamma \frac{\partial \phi_y}{\partial \boldsymbol{\sigma}} = \Delta \gamma \mathbf{m}, \qquad \qquad \text{\textit{Equation 7.18}}$$

where $\mathbf{m}$ is the direction of the plastic strain increment and means the normal direction of the yield surface. The increment of the equivalent plastic strain $\Delta \bar{\varepsilon}^p$ according to the principle of plastic work equivalence $(\phi_y \Delta \bar{\varepsilon}^p = \boldsymbol{\sigma} : \Delta \boldsymbol{\varepsilon}^p)$ is expressed as follows:

$$\Delta \bar{\varepsilon}^p = \frac{\boldsymbol{\sigma} : \Delta \boldsymbol{\varepsilon}^p}{\phi_y(\boldsymbol{\sigma})} = \Delta \gamma \frac{\boldsymbol{\sigma} : \frac{\partial \phi_y}{\partial \boldsymbol{\sigma}}}{\phi_y(\boldsymbol{\sigma})} = \Delta \gamma \frac{\phi_y(\boldsymbol{\sigma})}{\phi_y(\boldsymbol{\sigma})} = \Delta \gamma. \qquad \text{\textit{Equation 7.19}}$$

To find the plastic strain tensor, the unknown plastic strain increment $\Delta \bar{\varepsilon}^p$ or the plastic multiplier $\Delta \gamma$ should be obtained, if the deformation is plastic. Prior to that, assume that the total strain increment is elastic, to determine whether if the strain is elastic or plastic, and calculate the stress as follows:

$$\boldsymbol{\sigma}^T = \boldsymbol{\sigma}^{(n)} + \mathbf{C}^e : \Delta \boldsymbol{\varepsilon}, \qquad \qquad \text{\textit{Equation 7.20}}$$

where (n) means the reference state. $\mathbf{C}^e$ is the elastic tangent modulus as fourth-order tensor. A trial stress tensor $\boldsymbol{\sigma}^T$ checks whether the material is yielded by the yield condition as follows.

$$\Phi^{(n+1)} = \phi_y(\boldsymbol{\sigma}^T) - \sigma_y\left(\bar{\varepsilon}^{p\,(n)}\right), \qquad \qquad \text{\textit{Equation 7.21}}$$

where $(n+1)$ is the current state. If $\Phi < 0$, the deformation is elastic. Therefore, $\boldsymbol{\sigma}^T$ replaces the current stress $\boldsymbol{\sigma}^{(n+1)}$. If $\Phi \geq 0$, it is determined as the plastic deformation. The stress and internal values are updated based on the plastic multiplier $\Delta \gamma$. When the plastic strain increment

is not zero, the stress increment and update are calculated as follows using the increment of the elastic strain.

$$
\begin{aligned}
\boldsymbol{\sigma}^{(n+1)} &= \boldsymbol{\sigma}^{(n)} + \mathbf{C}^e : \left(\Delta\boldsymbol{\varepsilon} - \Delta\boldsymbol{\varepsilon}^{p\,(n+1)} \right) \\
&= \boldsymbol{\sigma}^{(n)} + \mathbf{C}^e : \Delta\boldsymbol{\varepsilon} - \mathbf{C}^e : \Delta\boldsymbol{\varepsilon}^{p\,(n+1)} \\
&= \boldsymbol{\sigma}^T - \mathbf{C}^e : \Delta\boldsymbol{\varepsilon}^{p\,(n+1)} \\
&= \boldsymbol{\sigma}^T - \Delta\gamma^{(n+1)} \mathbf{C}^e \mathbf{m}^{(n+1)}.
\end{aligned}
\qquad \textit{Equation 7.22}
$$

The update of the current stress is applied to the yield condition in Equation 7.21. The expression is described as follows (Yoon et al., 2004):

$$
\Phi^{(n+1)} = \phi_y \left(\boldsymbol{\sigma}^T - \Delta\gamma^{(n+1)} \mathbf{C}^e \mathbf{m}^{(n+1)} \right) - \sigma_y \left(\bar{\varepsilon}^{p\,(n)} + \Delta\gamma^{(n+1)} \right) \geq 0. \qquad \textit{Equation 7.23}
$$

To calculate the unknown plastic multiplier $\Delta\gamma$, a stress integration algorithm is used. In general, Eulerian backward algorithm (Crisfield, 1991) is used. The Eulerian backward algorithm leads to high accuracy and quadratic convergence rate, but it also increases the complexity more when a complex model is applied. In addition, explicit computation show no significant difference from other algorithms in terms of accuracy (Safaei et al., 2015). The convex cutting-plane (CCP) algorithm (Ortiz and Simo, 1986), which is relatively easy to use and computationally simple, is adopted for this study. The explicit computation is only used in this study, so it does not matter in terms of accuracy. Ortiz and Simo proposed that the main goal of the CCP is bypassing the need for computing the gradients, which is usually calculated in the Eulerian backward algorithm. The CCP considers the relationship between the elastic predictor and the plastic corrector. However, since the stress integral is calculated externally, the CCP is called to proceed in a semi-explicit manner.

The yielding condition of the CCP algorithm is not different from the Equation 7.23. The yield condition notation at every iteration (k) can be written as

$$
\Phi_{(k)}^{(n+1)} = \phi_y \left(\boldsymbol{\sigma}_{(k)}^{(n+1)} \right) - \sigma_y \left(\bar{\varepsilon}^{p}\,_{(k)}^{(n+1)} \right). \qquad \textit{Equation 7.24}
$$

To obtain the plastic multiplier $\Delta\gamma$, the following relation is generated by the Newton-Raphson iteration scheme:

The derivative of the plastic multiplier increment for the yield condition is expressed by the chain rule as

$$\delta\gamma_{(k)}^{(n+1)} = -\frac{\Phi_{(k)}^{(n+1)}}{\left(\frac{\partial\Phi}{\partial\Delta\gamma}\right)_{(k)}^{(n+1)}}, \qquad \textit{Equation 7.25}$$

$$\left(\frac{\partial\Phi}{\partial\Delta\gamma}\right)_{(k)}^{(n+1)} = \left(\frac{\partial\Phi}{\partial\phi_y}\frac{\partial\phi_y}{\partial\boldsymbol{\sigma}}\frac{\partial\boldsymbol{\sigma}}{\partial\Delta\gamma} + \frac{\partial\Phi}{\partial\sigma_y}\frac{\partial\sigma_y}{\partial\bar{\varepsilon}^p}\frac{\partial\bar{\varepsilon}^p}{\partial\Delta\gamma}\right)_{(k)}^{(n+1)}, \qquad \textit{Equation 7.26}$$

where

$$\frac{\partial\Phi}{\partial\phi_y} = 1 \qquad \textit{Equation 7.26a}$$

$$\frac{\partial\phi_y}{\partial\boldsymbol{\sigma}} = \mathbf{m} \qquad \textit{Equation 7.26b}$$

$$\frac{\partial\boldsymbol{\sigma}}{\partial\Delta\gamma} = -\mathbf{C}^e\mathbf{m} \qquad \textit{Equation 7.26c}$$

$$\frac{\partial\Phi}{\partial\sigma_y} = -1 \qquad \textit{Equation 7.26d}$$

$$\frac{\partial\sigma_y}{\partial\bar{\varepsilon}^p} = H \qquad \textit{Equation 7.26e}$$

$$\frac{\partial\bar{\varepsilon}^p}{\partial\Delta\gamma} = 1 \qquad \textit{Equation 7.26f}$$

where H is the slope of the flow stress defined generally by the uniaxial tensile test. $\delta\gamma_{(k)}^{(n+1)}$ is obtained by inserting the above Equations 7.26a $-$ 7.26f into Equation 7.25:

$$\delta\gamma_{(k)}^{(n+1)} = \frac{\Phi_{(k)}^{(n+1)}}{\mathbf{m}_{(k)}^{(n+1)}\mathbf{C}^e\mathbf{m}_{(k)}^{(n+1)} + H_{(k)}^{(n+1)}}. \qquad \textit{Equation 7.27}$$

After the increment of the plastic multiplier is obtained, the stress and internal variables are updated in every iteration by the following:

$$\Delta\gamma^{(n+1)}_{(k+1)} = \Delta\gamma^{(n+1)}_{(k)} + \delta\gamma^{(n+1)}_{(k)},$$

Equation 7.28a

$$\boldsymbol{\varepsilon}^{p\,(n+1)}_{(k+1)} = \boldsymbol{\varepsilon}^{p\,(n+1)}_{(k)} + \delta\gamma^{(n+1)}_{(k)}\mathbf{m}^{(n+1)}_{(k)},$$

Equation 7.28b

$$\boldsymbol{\sigma}^{(n+1)}_{(k+1)} = \boldsymbol{\sigma}^{(n+1)}_{(k)} - \Delta\gamma^{(n+1)}_{(k)}\mathbf{C}^e\mathbf{m}^{(n+1)}_{(k)}.$$

Equation 7.28c

The iteration of the stress integration continues until the updated stress and internal variables satisfy the yield condition in Equation 7.24.

In the case of a non-AFR, the components of the plastic strain increment are determined by the normal direction of the potential function rather than the yield function. The flow rule for the non-AFR is expressed as follows:

$$\Delta\boldsymbol{\varepsilon}^p = \Delta\gamma\frac{\partial\phi_p}{\partial\boldsymbol{\sigma}} = \Delta\gamma\mathbf{n},$$

Equation 7.29

where $\mathbf{n}$ is the normal direction of the potential function and the direction vector for the plastic strain increment. Again, considering the principle of plastic work equivalence, the equivalent plastic strain increment is

$$\Delta\bar{\varepsilon}^p = \frac{\boldsymbol{\sigma}:\Delta\boldsymbol{\varepsilon}^p}{\phi_y(\boldsymbol{\sigma})} = \Delta\gamma\frac{\boldsymbol{\sigma}:\frac{\partial\phi_p}{\partial\boldsymbol{\sigma}}}{\phi_y(\boldsymbol{\sigma})} = \Delta\gamma\frac{\phi_p(\boldsymbol{\sigma})}{\phi_y(\boldsymbol{\sigma})} = \Delta\gamma h,$$

Equation 7.30

where h is the ratio of the potential function to the yield function. The equivalent plastic strain increment is not the same as the plastic multiplier increment in comparison to the associated flow rule. Therefore, the update of the current stress has a change:

$$\boldsymbol{\sigma}^{(n+1)} = \boldsymbol{\sigma}^T - \Delta\gamma^{(n+1)}\mathbf{C}^e\mathbf{n}^{(n+1)}.$$

Equation 7.31

By changing the update of the current stress, the equations for finding the change of plastic multiplier increment are also changed. The two partial differentials in Equations 7.26c and 7.26f are modified as follows:

$$\frac{\partial \boldsymbol{\sigma}}{\partial \Delta \gamma} = -\mathbf{C}^e \mathbf{n}, \qquad\qquad \textit{Equation 7.32a}$$

$$\frac{\partial \bar{\varepsilon}^p}{\partial \Delta \gamma} = h, \qquad\qquad \textit{Equation 7.32b}$$

In the case of the AFR, the formula for obtaining the change of plastic multiplier increment is finally obtained as follows:

$$\delta\gamma_{(k)}^{(n+1)} = \frac{\Phi_{(k)}^{(n+1)}}{\mathbf{m}_{(k)}^{(n+1)}\mathbf{C}^e\mathbf{n}_{(k)}^{(n+1)} + H_{(k)}^{(n+1)}h_{(k)}^{(n+1)}}. \qquad \textit{Equation 7.33}$$

After the change in plastic multiplier increment is obtained, the iterative updates of the stress and the internal variables are expressed as follows:

$$\Delta\gamma_{(k+1)}^{(n+1)} = \Delta\gamma_{(k)}^{(n+1)} + \delta\gamma_{(k)}^{(n+1)}, \qquad\qquad \textit{Equation 7.34a}$$

$$\bar{\varepsilon}^{p\,(n+1)}_{(k+1)} = \bar{\varepsilon}^{p\,(n+1)}_{(k)} + \Delta\gamma_{(k+1)}^{(n+1)}h_{(k)}^{(n+1)}, \qquad\qquad \textit{Equation 7.34b}$$

$$\boldsymbol{\varepsilon}^{p\,(n+1)}_{(k+1)} = \boldsymbol{\varepsilon}^{p\,(n+1)}_{(k)} + \delta\gamma_{(k)}^{(n+1)}\mathbf{n}_{(k)}^{(n+1)}, \qquad\qquad \textit{Equation 7.34c}$$

$$\boldsymbol{\sigma}_{(k+1)}^{(n+1)} = \boldsymbol{\sigma}_{(k)}^{(n+1)} - \delta\gamma_{(k)}^{(n+1)}\mathbf{C}^e\mathbf{n}_{(k)}^{(n+1)}. \qquad\qquad \textit{Equation 7.34d}$$

The iterative calculation continues as before during which the material is plastic deformed by the yield condition. The stress tensor differentials **m** and **n** required for stress integration are described in Appendix 11.2.

The stress integration for applying the associated and non-AFR of Yld2000-2d to the user subroutine VUMAT in Abaqus/Explicit was described so far. This allows using the material model to represent the planar anisotropy of the test materials precisely.

7.1.4 Verification of the implemented model

The planar anisotropic yield function Yld2000-2d was implemented in the user subroutine VUMAT for Abaqus/Explicit. It is now necessary to ensure that the implemented model shows accurate strains and stresses directionally for this purpose. First, the theoretical values are

compared with the numerical calculation values. The theoretical normalized stresses and the Lankford coefficients can be calculated from the yield function considering the uniaxial tensile stress tensor for each direction. This method is summarized in Appendices 11.1 and 11.2 to calculate the analytical values. Numerical analysis by VUMAT in Abaqus gives the normalized stresses and the Lankford coefficients in various directions to the rolling direction as numerical values. The material used for the validation is AA2090-T3 (Safaei et al., 2014), taking the directionally normalized stresses and Lankford coefficients. For the numerical analysis, the information about isotropic hardening from the published paper (Safaei et al., 2014) is also used. Although AA2090-T3 differs from the test materials used in this study, it has a strong anisotropic property and is a published verification data, so it can give high reliability as a reference value to confirm the implementation of the yield function with the AFR and non-AFR.
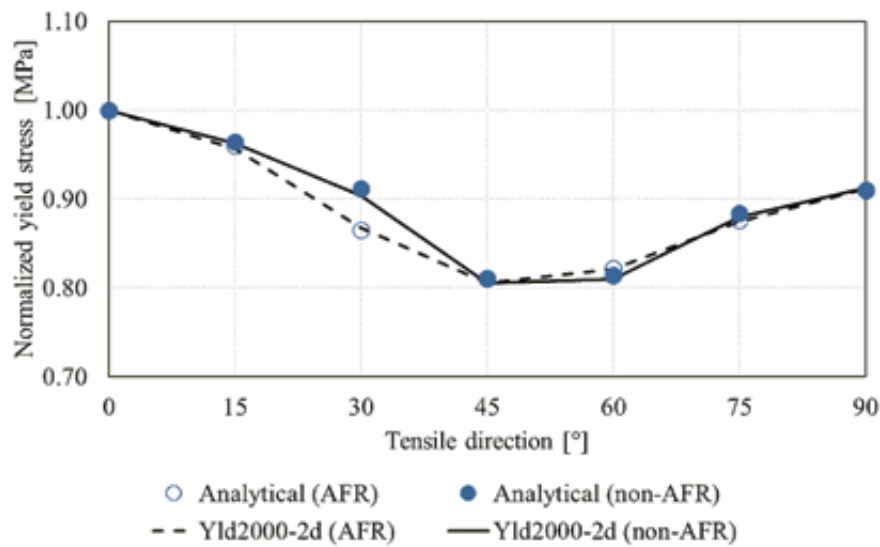
Figure 7.1: Analytical and numerical values of normalized yield stress directionality for Yld2000-2d with different flow rule

Figure 7.1 shows the calculated normalized stress values of the AFR and non-AFR compared with the analytical values in different tensile directions. The Yld2000-2d implemented with the above CCP algorithm shows a good agreement with the analytical values, the AFR and non-AFR through VUMAT. This shows that VUMAT is well implemented in Abaqus and numerical calculations calculate the anisotropic stress as intended. A note is that the anisotropic material behavior for the AFR and non-AFR stresses is different. In the AFR, the Yld2000-2d considers stress input values of 0, 45, and 90° in the uniaxial tension direction. On the other hand, the non-AFR requires additional stress input values of 15°, 30°, 60° and 75°. Because of these differences, the material inputs behave in agreement with each other for 0°, 45°, and 90°, which

are the common input values for determining the anisotropy parameters, but they are different in other tensile directions.

The Lankford coefficients also shows differences in the AFR and non-AFR compared with the analytical values in different tensile direction. As in the stress comparison, the accuracy of the VUMAT is verified, and the anisotropic material behavior differs also between the AFR and the non-AFR in the Lankford coefficients. In the tensile direction 0°, 45°, and 90°, they coincide with each other. In the other tensile directions, AFR shows higher values than non-AFR.
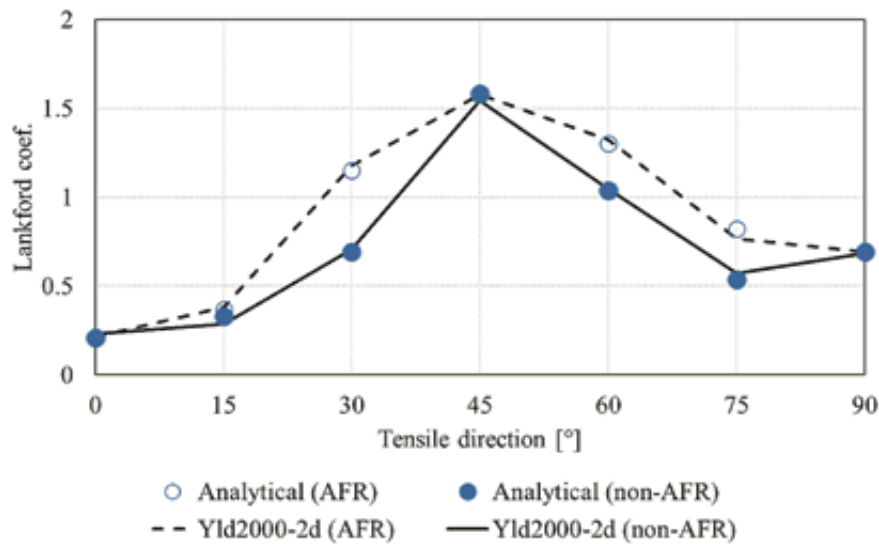
Figure 7.2: Analytical and numerical values of Lankford coefficient directionality for Yld2000-2d with different flow rule

By comparing with the analytical values, it is shown that the implementation of the yield functions succeeded whatever flow rule was used. However, depending on whether or not the potential function considered in each direction, the behavior of anisotropic materials is different even for the same material. In order to recognize which model represents the anisotropy of the material better, experiments should be performed, and the results are compared with the numerical values. Therefore, the results of the physical material anisotropy from the material test will be compared to the simulation results of the AFR and non-AFR.

The tensile specimens from 0° to 90° by 15° from the rolling direction are made by the milling process. The stresses and Lankford coefficients at tensile elongation of 10% are measured in every direction by the uniaxial tensile test in Chapter 5. The measured results are used as a reference value for comparison with the simulated values of the material model to confirm the physical accuracy.

The calculated stresses and Lankford coefficients of Hill48 (quadratic yield function) are compared with each other. Since the Hill48 is already implemented in Abaqus, the model can

be easily used to represent the anisotropic behavior of the test material compared to the Yld2000-2d. To identify the parameters of the Hill48, only the Lankford coefficients of r_0, r_{45}, and r_{90} and the uniaxial flow stress in the rolling direction are required. The Hill48 calculates the directional stresses and Lankford coefficients from 0° to 90° by 15°. Normalized stresses and Lankford coefficients are calculated by a uniaxial tensile of one element in the simulation and are shown in Figures 7.3 and 7.4 for AA6016 and HX260, respectively.
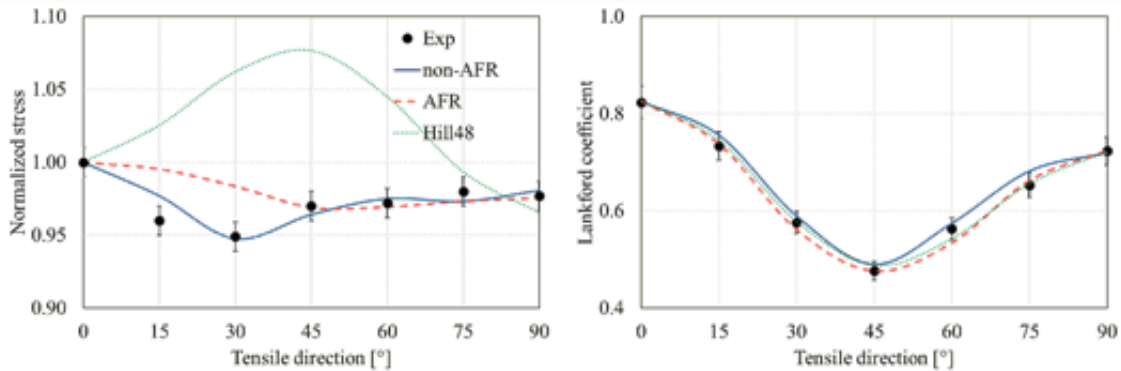
Figure 7.3: Comparison of the experimental directional stresses and Lankford coefficients with the simulative results from various material models for AA6016

In the case of AA6016, the Hill48, and the Yld2000-2d with the AFR and non-AFR agree with the Lankford coefficients measured from the uniaxial tensile test. The Hill48 as a quadratic function agrees with the experimental Lankford coefficients. It is seen that the Lankford coefficients of AA6016 have a quadratic distribution with respect to the tensile direction from 0° to 90°.

On the contrary, the comparison of each material model with the directional normalized stress values shows different aspects. The Yld2000-2d with the non-AFR are consistent with almost all measured stress values. The non-AFR calculated the normalized stress to be slightly higher than the measured stress value only at the tensile direction of 15°. However, the difference is insignificant when compared with the simulated values of other models. The AFR shows no significant difference from the experimental stress values after 45°. The stress values simulated at the tensile directions of 15° and 30° are higher than the experimental values, and the qualitative trends do not fit much. It shows that the directional stresses of the Hill 48 do not match the experimental values except for the stress at 0° in the tensile direction. The Hill48 does not qualitatively follow the stress distribution tendency with respect to the tensile direction. The comparison of the normalized stresses and Lankford coefficients shows that the non-AFR describes the most similar material behavior of AA6016.
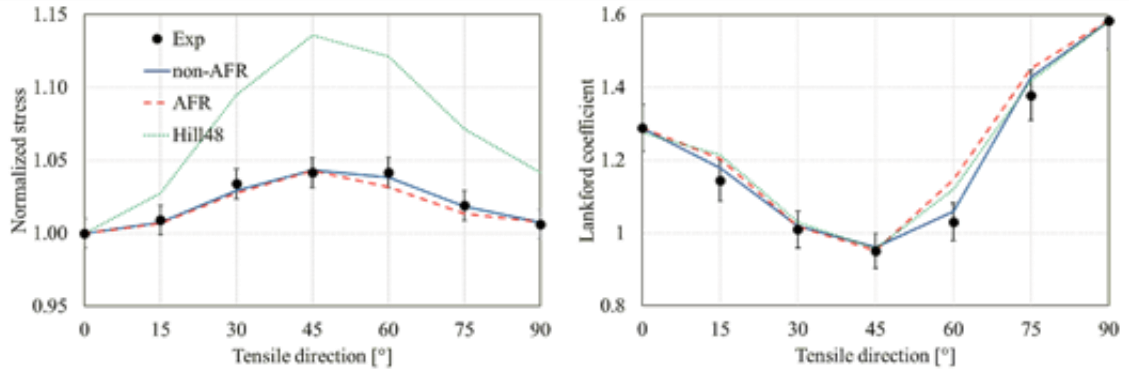
Figure 7.4: Comparison of the experimental directional stresses and Lankford coefficients with the simulative results from various material models for HX260LAD

In the case of the HX260LAD, all three models tend to be similar in quality to the measured Lankford coefficients in all tensile directions. However, the AFR and Hill48 calculated slightly higher simulated values than the experimental values at 15° and 60° in the tension direction. The difference in the tensile direction at 60° shows a large difference of about 10%. The Lankford coefficients of the non-AFR are consistent with all the measured Lankford coefficients.

The normalized stress distribution compares with the experimental results of the Yld2000-2d with the AFR and non-AFR. However, the Hill48, like AA6016, does not match the experimental values except the tensile direction of 0°. The normalized stress at 45° in the tensile direction of the Hill48 is about 10% different from the experimental value. The non-AFR shows the most accurate material behavior in the directional stresses, and the AFR shows no significant difference too.

To summarize, the directional stresses and Lankford coefficients were experimentally determined for both test materials AA6016 and HX260LAD, and these were determined as indicators of anisotropic material behavior. As a result, the non-AFR showed the highest accuracy in all aspects after comparing each model, and the AFR showed no significant difference from the experimental values except for the partial stress distribution of AA6016. However, the Hill48 is not suitable for expressing anisotropic materials because it does not properly express the anisotropic property of stress. Therefore, the use of the Yld2000-2d in this study seems reasonable.

7.2 Prediction of the forming limit

In the bead forming for the bead optimization, the strain path is usually nonlinear. The linear FLC does not predict the forming limit of the sheet including the nonlinear deformation paths.

Therefore, the Generalized Forming Limit Concept (GFLC) is used, which can consider the nonlinear deformation path for this study. In order to prepare a GFLC data, a FLC data are required from general linear FLCs and subsequent FLCs from six different pre-strains. Thus, tens to hundreds of material tests are required.

In this study, the GFLC data of materials AA6016 and HC260LAD obtained from a pre-study in utg are used to reduce the effort of material tests. The materials used in this study are the aged AA6016 and HX260LAD. The experimental materials are different from the existing materials. The properties of aged AA6016 changes than when it is manufactured after a certain time. HX260LAD and HC260LAD are commonly manufactured by cold rolling, but the chemical contents are different. HX260LAD has a chromium content of 15–19 wt% and 64–68 wt% nickel as a compound, HC260LAD has a nickel content of 26–30 wt%, max 4 wt% . In order to compare the macroscopic material behavior between the two materials by these, the obtained FLCs of aged AA6016 and HX260LAD from Section 5 is shown in Figure 7.5 and 7.6, respectively. They are compared with the conventional FLC of AA6016 and HC260LAD.
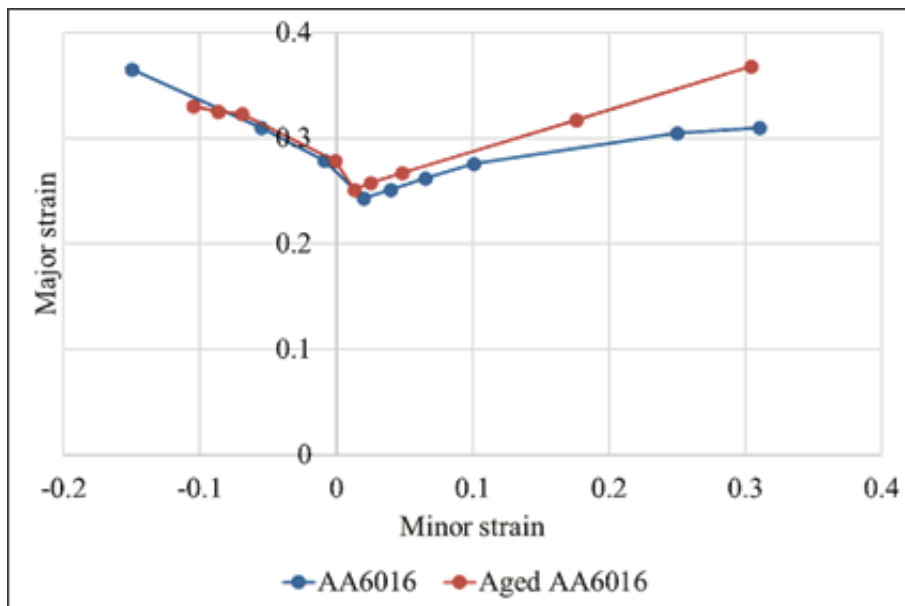
Figure 7.5: Comparison of FLC for AA6016 and old AA6016

AA6016, which was previously for the GFLC data generation, and aged AA6016 overlap in the region, where the minor strain is less than 0.01. By the uniaxial stretching region, the slope of the aged AA6016 to the deep drawing region appears to be lower than the slope of AA6016. Thus, aged AA6016 is expected to have a slightly lower formability toward the uniaxial stretching region. Based on the minor strain of 0.01, the region between the plane strain and biaxial tensile state shows the difference between each other. Since the FLC of aged AA6016 is higher than the FLC of AA6016, aged AA6016 exhibits higher formability in the biaxial

stretching region. In the biaxial tensile region, the slope of AA6016 is closer to the horizontal as it goes to the right, while the slope of the aged AA6016 shows a linear increase. It concludes that the difference between the two FLCs in the biaxial tensile region becomes larger as the minor strain increases.

It is unusual that the aged AA6016 has more ductility than the AA6016. The aging effect of the aluminum alloy leads to more strengthen and reduce the elongation. The above unusual difference is caused by the difference of the manufacturing quality depending on usage purpose of the alloy. The AA6016 was not purposed on the usage for forming technology, otherwise, the aged AA6016 was specialized for sheet metal forming. Even though the AA6016 for forming is aged, it can have more ductility comparing with no optimized AA6016 for the sheet metal forming.
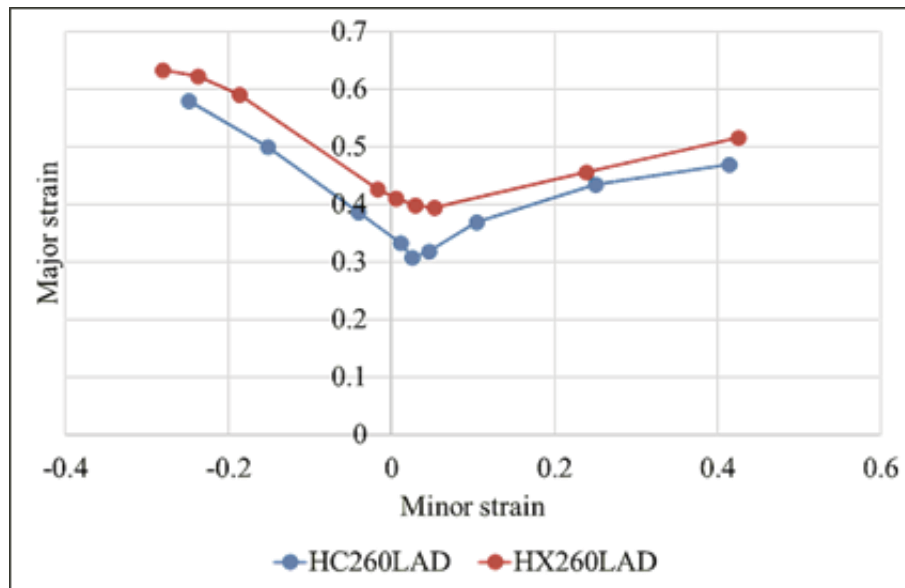
Figure 7.6: Comparison of FLC for HC260LAD and HX260LAD

HX260LAD exhibits significantly higher forming limits in all areas compared to HC260LAD. The difference is the largest in the region where the negative strain is near 0, that is, the plane strain region. That is, the FLC comparison shows a similar trend for the curves, but the formability is different.

However, subsequent FLCs based from six preforming, which are data considering nonlinear paths, are not newly obtained, and the data are scaled by the scaling factor from the difference between the existing FLC and the actual FLC. This allows the existing GFLC data to fit into the current material. The precondition of this method is the same material or is valid for the same class of material. In the case of AA6016, the GFLC data can be scaled because they are the same material and aged AA6016 changes in material property only with time. HX260LAD and HC260LAD belong to the same class. Thus, by scaling from the difference between the

FLC of each material, the existing GFLC data are proportionally scaled. These are then verified through experimental verification of the accuracy and scalability of the GFLC.

The prepared GFLC is implemented in Excel by Visual Basic. In order to calculate GFLC value regarding the forming limit, the strains are imported from the simulation result of Abaqus using the Python script. The Python script is able not only to make connection between Abauqs and Excel, but also to automate the procedure of the import and the analysis of the GFLC. The flow diagram of that is described in Figure 7.7.
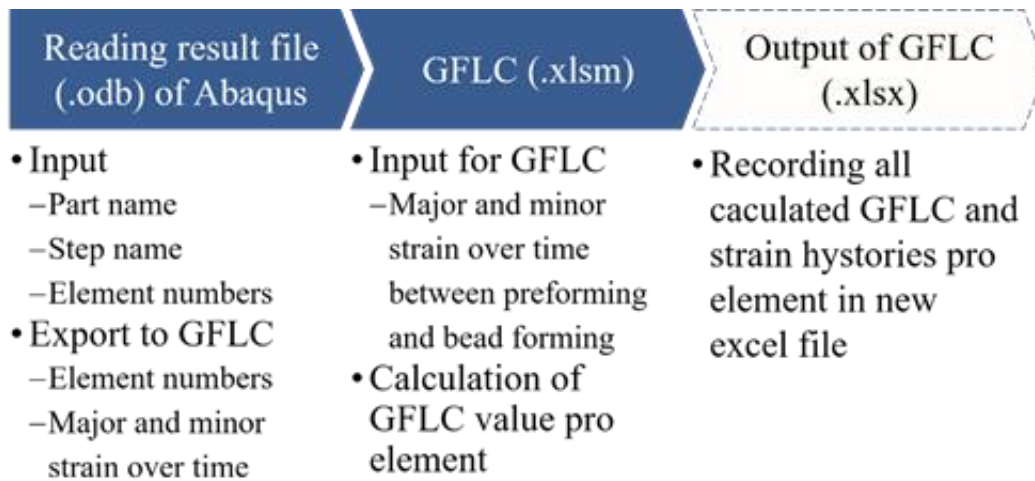
Figure 7.7: Flow diagram of the procedure for the analysis of GFLC from the Abaqus result

7.3 Forming simulation

As an example to be used in developing this bead optimization program (Figure 7.8), a punch and die tool are used. This tool is a modified Maciniak tool to represent various forming states by various initial specimen shapes (Weinschenk and Volk, 2017). Typically, three specimen geometries are used to have different deformation states after a preforming. Figure 7.9 shows the specimen geometries for the uniaxial, plane strain, and biaxial loading state, respectively. The three states represent typical deformation states to indicate the direction of a strain path. A specimen is formed in a deep drawing analysis with the tools as the preforming. The strain distribution analyzed from the preforming is used to determine the initial bead shape.
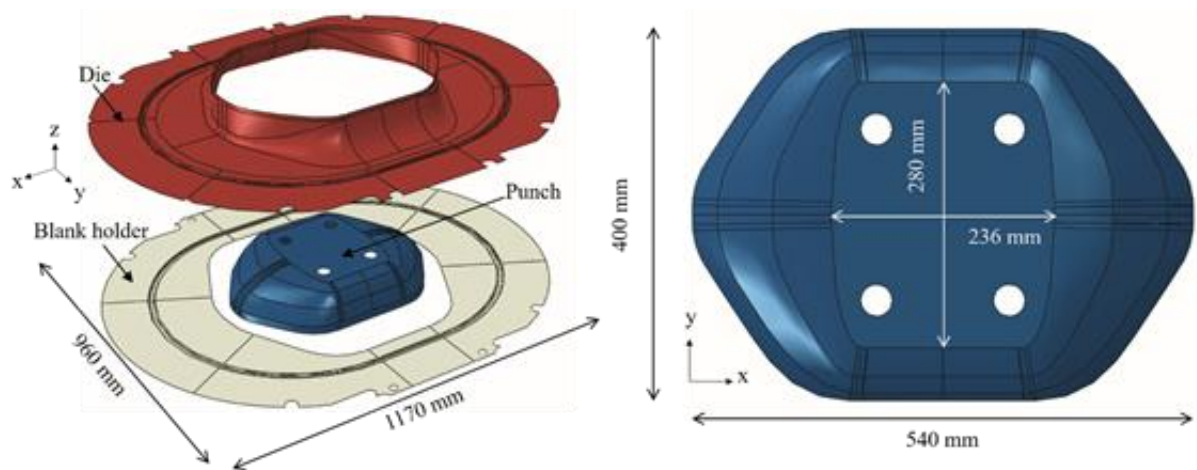
Figure 7.8: Tool geometries for preforming (Weinschenk and Volk, 2017)
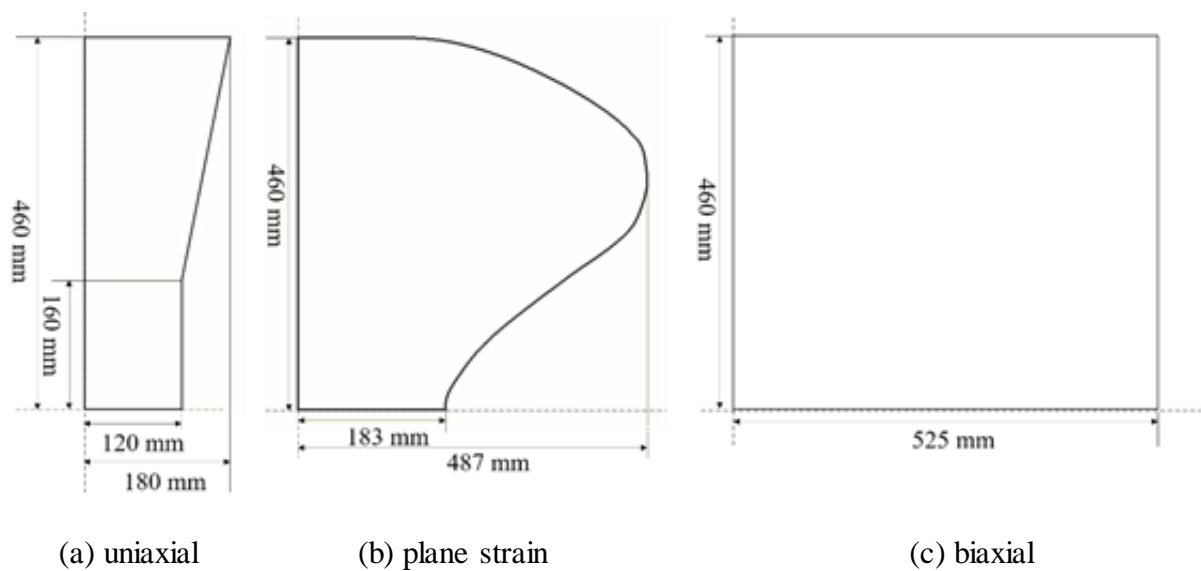
(a) uniaxial   (b) plane strain   (c) biaxial

Figure 7.9: Geometries of test specimens (Weinschenk and Volk, 2017)

The bead tools consist of two parts. One is the upper bead, and other is the lower bead. The basic shape of the lower bead mimics the punch shape used in the preforming as shown in Figure 7.8. The contact surface of the upper bead is offset by 1 mm of material thickness from the surface of the lower bead. In all tools used for preforming, the punch for preforming is replaced with bead tools. The embossed bead geometry is positioned on the upper bead, and the lower bead is constructed to make the negative bead geometry. The bead position is determined based on the trajectory determined along the direction of the principal bending stress. The stress distribution is determined after the specified load case on the preformed part. The loading case used in this study is shown in Figure 7.10.

Figure 7.10: Stiffness analysis in the forming simulation using pin loading on the middle of the part

An example load case is to apply a vertical load at the center of the preformed part by a pin with a diameter of 20 mm and a load depth of 20 mm. The bead lines of the preformed and bead-formed part are fixed during the pin loading. The resulting stress distribution provides as an input to determine the position of the bead, which can maximize stiffness of the part. The stress distribution after the load case is shown in Figure 7.11 for each material.
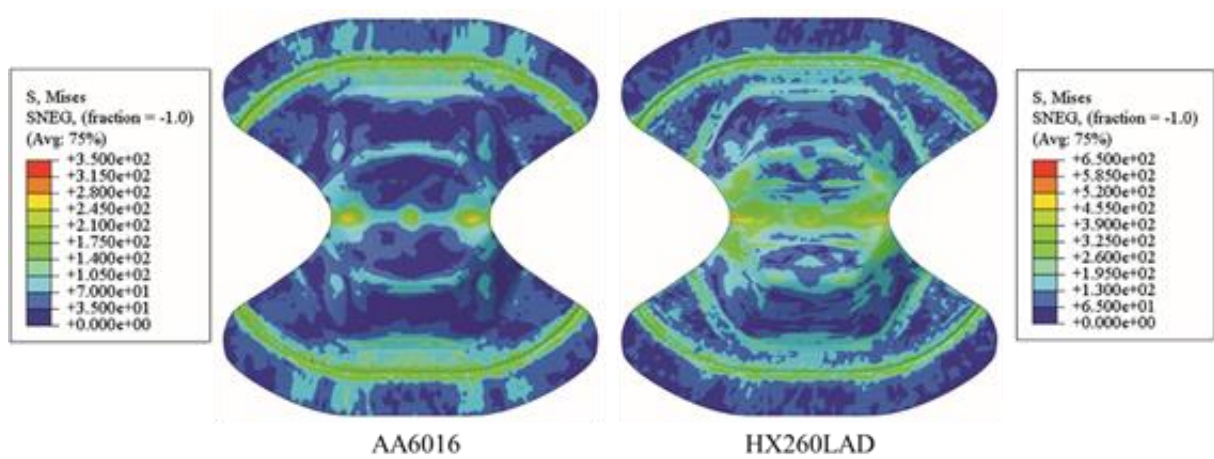
Figure 7.11: Stress distribution of AA6016 (left) and HX260LAD (right) after loading by pin

The maximum stress of AA6016 is almost half-maximum stress of HX260LAD. Middle of stress levels for each material is differently distributed, but the maximum levels are similarly distributed on the center and both side of middle position. The trajectory is generated based on AA6016 as shown in Figure 7.12. It is expected that the trajectory has a similar influence of the stiffening effect on both materials
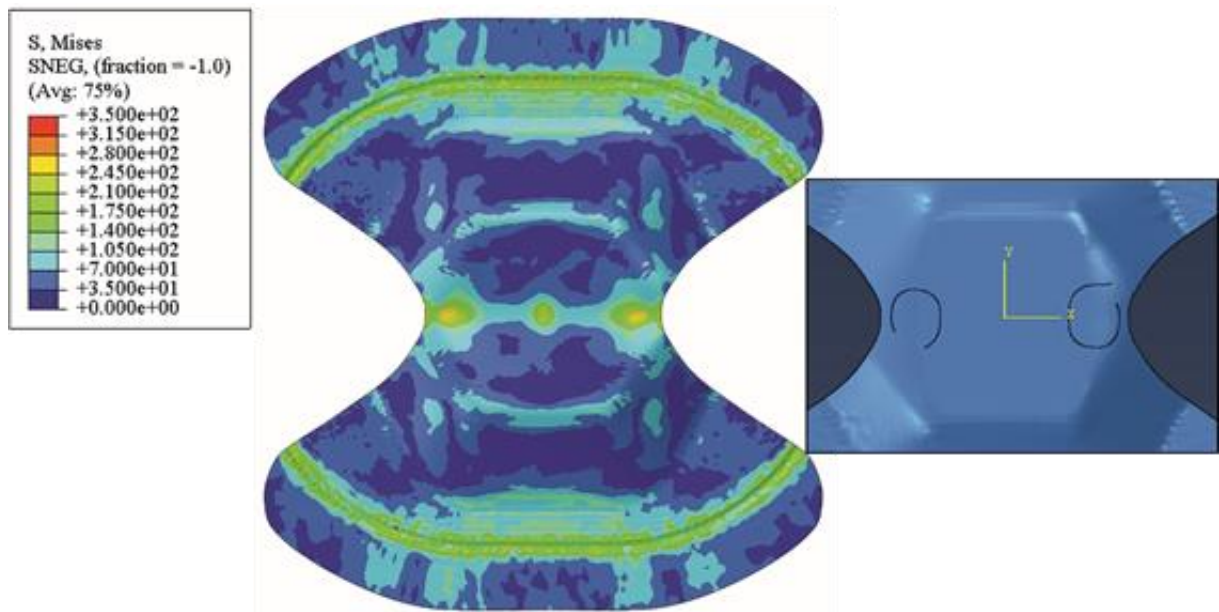
Figure 7.12: generated trajectory on the bead part based on stress distribution of AA6016

The upper bead is constructed so that the bead geometry can be inserted into the groove in the upper bead in order to have adjustable bead heights. Therefore, the bead height from 3 mm to 9 mm is adjustable in the upper die to check a bead height, which leads to material failure.

The bead locations are the trajectories on the design area in the path determined. Splines are created based on the coordinates of the trajectories. The cross-section of the bead geometry with a bead height of 5 mm, an angle of 45°, a width of 30 mm, and a radius of 5 mm is created on the created splines to construct the bead dies as shown in Figure 7.13.
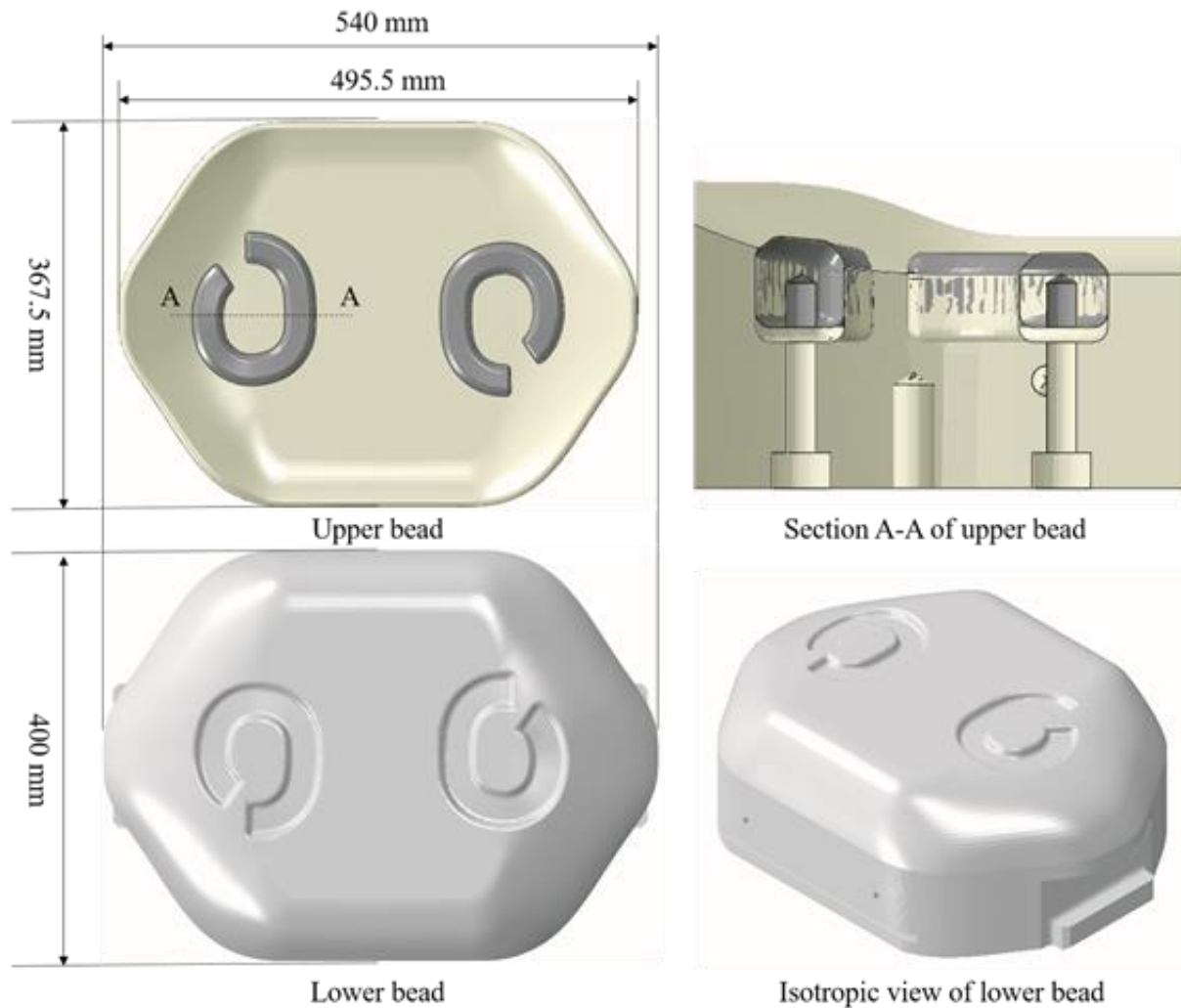
Figure 7.13: Bead tools for the experimental validation

The frictional condition and blank holding force are used as values of 0.1 and 1400 kN, respectively. The influences of friction and blank holding force was investigated (Cha et al., 2017). The bead-formed parts of the test materials were manufactured in safety with the friction coefficient of 0.1. But, the blank holding forces between 1200 and 1600 had a negligible influence on the formability.

8 Influence of preforming and bead geometry

Before proceeding with the bead optimization, the initial bead cross sections should be suggested considering the formability. The determination of the initial bead geometry may also appear as an open problem. To determine this as a quantitative value, it is useful to parameterize the cross sections of the bead geometry. The quantitative parameter values can be determined using the deformation results from the preformed deep-drawn part. The available values include coordinates, strain, and stress of the preformed part. As mentioned above, the formability of the initial bead geometry should be taken into account, and the formability prediction is based on the strain by the GFLC. Therefore, the relationship between the strains of the preformed part and the initial value of the cross-sectional parameters can be defined as a function with a maximum formability reference. Before geometry parameterization, the type of bead geometry has been investigated. The bead geometry may have different cross-sectional geometry, and four types are generally mentioned: box, trapezoidal, half-round and triangular. We define the bead geometry as shown in Figure 8.1. This geometry definition consists of four geometry parameters (top and bottom chords, flank, radius). It was investigated how these five bead geometry parameters affect stiffness and manufacturability.
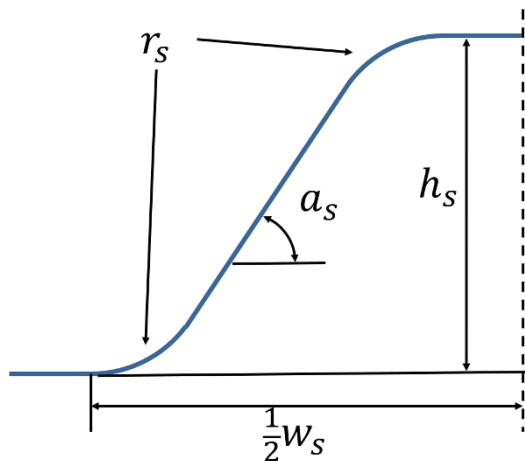
Figure 8.1: Definition of the bead geometry parameters

This geometry definition consists of four geometry parameters: radius r_s, flank angle a_s, bead width w_s, and bead height h_s. The influence on the stiffness was investigated by comparing the load sizes at different radii. It was confirmed that the difference is not large. In addition, changes in width and flank angle do not have a large influence on the stiffness and the formability. Since the height of the bead cross section has a great influence on the stiffness and formability, and the height change plays an important role in maximizing the stiffness through the bead shape. It was also confirmed that the stiffness increases due to bead geometry when the forming limit is reached. (Cha et al., 2016)

8.1   Simulation model for sensitivity analysis

In order to investigate the influence of the bead geometries on stiffness, the bead geometry is loaded after the bead forming. Figure 8.2 shows the bead-formed part, the loading pin, and the support plate for the load case. The pin giving the vertical load to the bead geometry has a contact surface with a diameter of 20 mm. Since the pin loads on the bead geometry in the z-direction, a support plate is used to prevent the rigid body movement of the bead-formed part. To load ideally, the constraints in the x- and y-directions is applied to the bead line of the part. The load calculated according to the bead geometries is used as an index of stiffness.
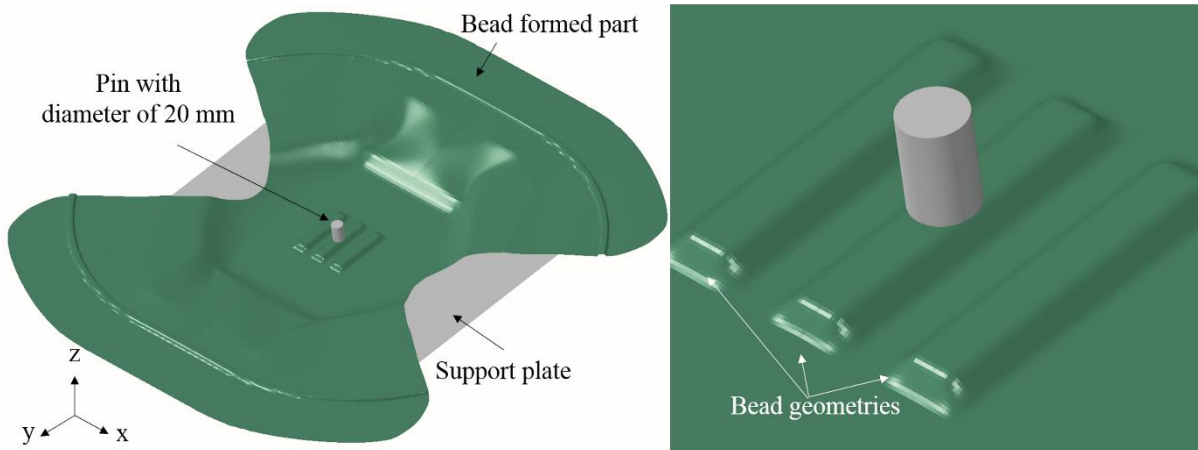
Figure 8.2: Simulation model of load case for sensitivity analysis of the bead geometry

The bead geometry has a length of 100 mm, a radius of 5 mm, and a width of 30 mm. The gap between the bead geometries is varied based on the bead rate of 1.0, when the height and flank angle are changed. The flank angle, and height will be changed to investigate the influence on the stiffness and the formability. Furthermore, the mesh test is carried out to find proper element length that gives reliable results. The element lengths of 0.75, 1.0, 1.5 and 2.0 mm are meshed in bead geometry. The different element lengths show no big difference in load curve at pin loading, but the strain results are differently calculated at an element with maximum major strain and its neighbor elements. The mean and standard deviation of strains are compared according to element length in Figure 8.3. The element length of 2.0 mm only shows a big difference with others in mean and standard deviation of strain. Other element lengths have the mean value more than 0.24 and less the standard deviation than 5 %. The converging tendency is started after the element length 1.5 mm. The difference of the element lengths of 0.75 and 1.0 mm has under 1.0 % in the mean value and the standard deviation. That difference is negligible. Therefore, the element length of 1 mm is set for the forming simulation regarding computing efficiency and precision.
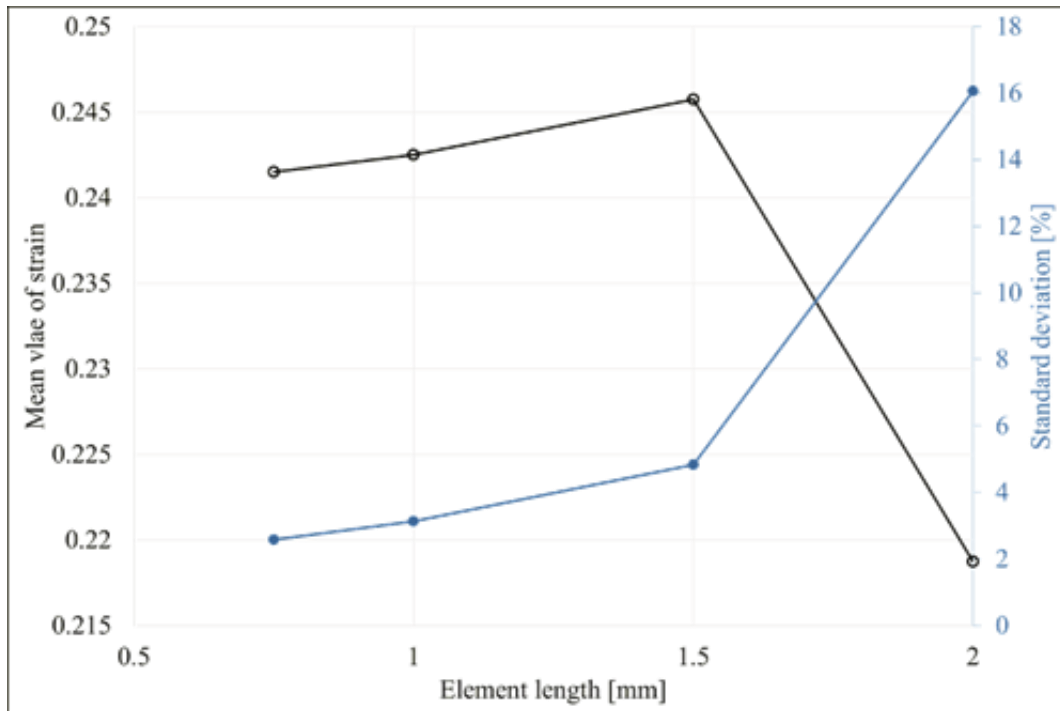
Figure 8.3: Strain mean and standard deviation according to element length

The GFLC is calculated with major and minor strains by the Python-script as mentioned in Section 7.2. The formability is evaluated by the maximum value of GFLC. The prepared forming simulation and the GFLC are used to investigate the parameters of the bead geometry regarding the stiffness and formability.

8.2 Bead flank angle

It is known that the flank angle has a higher stiffness under vertical load and lower stiffness in the horizontal load (Schwarz, 2002). As an example, a pin vertically loads the beads with the different flank angles. The beads have a height of 6 mm, and the material taken as an example is AA6016. The load-displacement curves are shown in Figure 8.4.
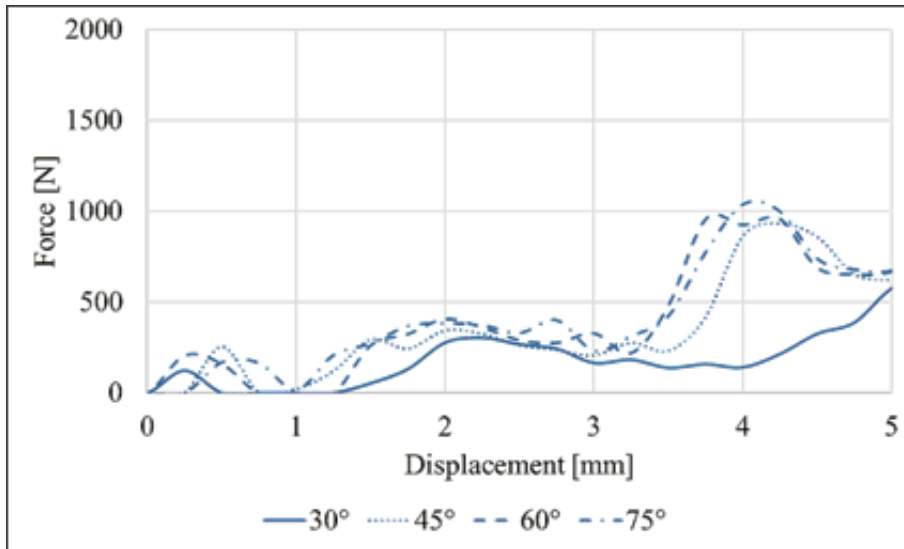
Figure 8.4: Influence of flank angle on stiffness
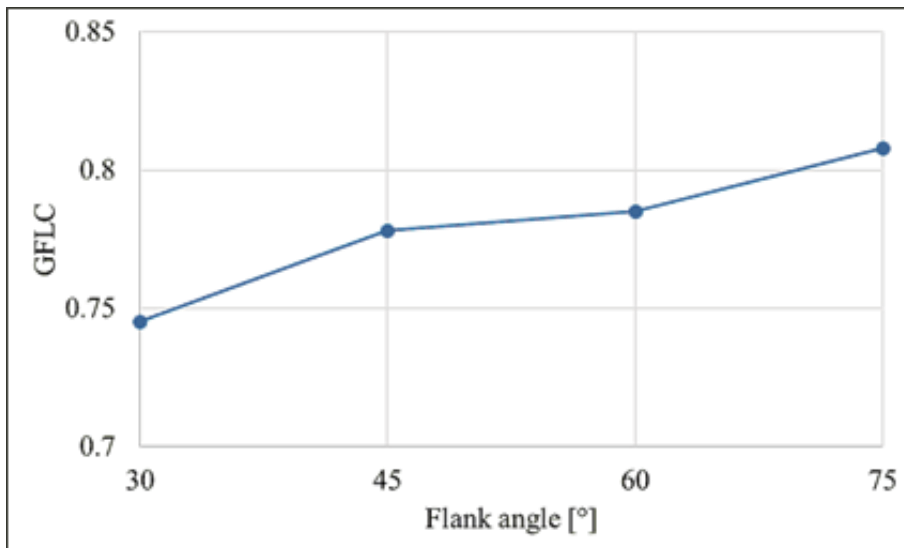
Figure 8.5: Influence of flank angle on formability

From the vertical load, the load-displacement curve does not show a large difference from 75° to 45°, but the load curve is lower at 30°. This results in an angle of more than 45° for the vertical load and a lower angle for a greater stiffness for the horizontal load.

The influence of the flank angle on the formability is also shown in Figure 8.5 according to the GFLC tendency. Generally, the GFLC value increases with the flank angle. The larger the flank angle, the lower the formability, but even if the flank angle increases, the stiffness is not significantly increased under the defined load case to identify normal stiffness. In addition, the flank angle of 45° and 60° has a minor effect on formability. It is proposed to select approximately 60° under a vertical load.

8.3 Bead height

The strains of the preformed parts can be subdivided into major and minor strains on the plane. The ratio of the major and minor strains can recognize the deformation state, and the size of the major strain can be the deformation degree in each deformation state. The influence of the bead height on the formability in the plane strain state is investigated in accordance with the change in the bead height. For this example, the flank angle is set at 60°, and the width and the radius are 30 mm and 5 mm, respectively. The drawing depth in the preforming is 70 mm, and then, the defined bead is formed at the middle of the preformed part. The highest strain values were shown at the radius of the bead, and the GFLC was calculated using the calculated strain history until the bead forming. The vertical pin load on the middle of the bead-formed part is defined as the load case. Figure 8.6 shows the influence of the bead height on the maximum load as stiffness for two test materials.
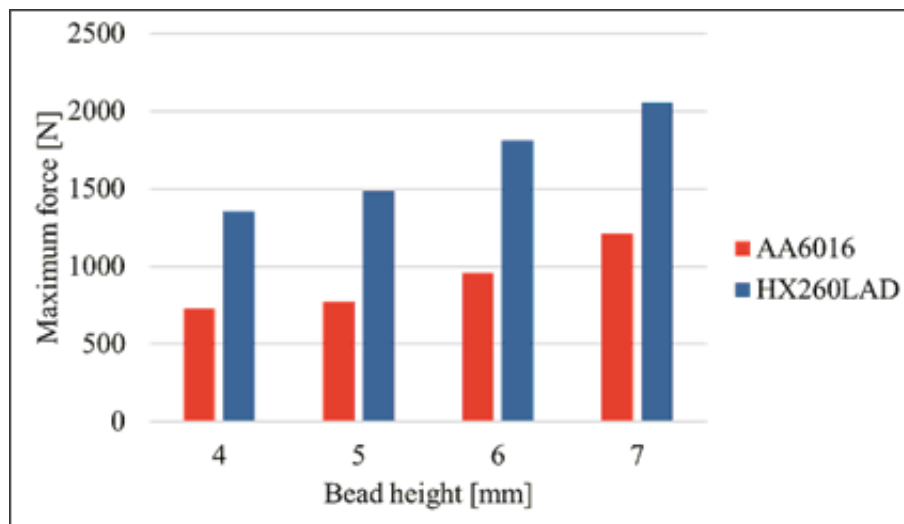
Figure 8.6: Influence of bead height on the stiffness for test material AA6016 and HX260LAD

The bead height increased from 4 mm to 7 mm by 1 mm. The maximum values at the load of the pin over the bead height are represented as a bar graph. Although the bead of the aluminum has a lower maximum load than that of the steel, the maximum load tendency of bead height is

the same. The increase in the maximum load between the bead heights of 6 mm and 7 mm is greater than the maximum load increase between the bead heights of 4 mm and 5 mm for the both test materials. The increase in the bead height has a progressive influence on stiffness. Figure 8.7 shows the influence of the bead height on the GFLC value as formability for two test materials.
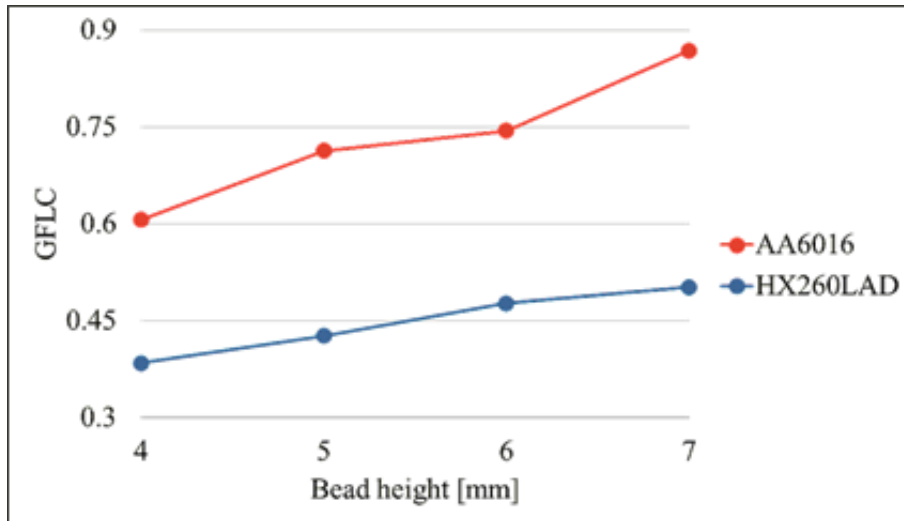
Figure 8.7: Influence of the bead height on the formability for test material AA6016 and HX260LAD

The influence of the bead height on the formability for both materials shows that the GFLC value increases almost linearly as the bead height increases from 4 mm to 7 mm. In formability, the aluminum has higher GFLC values than the steel. The steel has higher ductility and is capable of producing bead heights greater than the aluminum. The bead height needs to be considered in terms of the formability depending on the material.

When the GFLC value reaches 1.0, it means that a local necking occurs. Therefore, it can be seen that the bead height of 7 mm is still producible. If the GFLC is reliable, the stiffness effect through the maximum load is a reliable result. Obviously, the higher the bead height, the closer the material is to the forming limit. For this reason, it is an object of the bead optimization method considering the manufacturability to determine the bead height close to the forming limit.

8.4   Preforming

The bead height of 6 mm is set, the flank angle is 60°, the width is 30 mm, and the radius is 5 mm. The drawing depth of the preforming is defined the degree of the preforming and varies to

investigate the influence of the degree of the preforming on the formability according to the GFLC value. Furthermore, the investigation for the influence of the deformation state is carried out with three different geometries of the specimens as well as in the uniaxial, plane strain and biaxial state. The drawing depth of the preforming varies from 40 mm to 70 mm by 10 mm. The bead forming simulation as the subsequent forming is carried out, and the GFLC analyzes the forming limit of the bead formed parts as in the previous investigation for the influence of the bead height. Figures 8.8 and 8.9 summarize the influence of the preforming degree by varying the drawing depth on the formability of two test materials in the different deformation states.
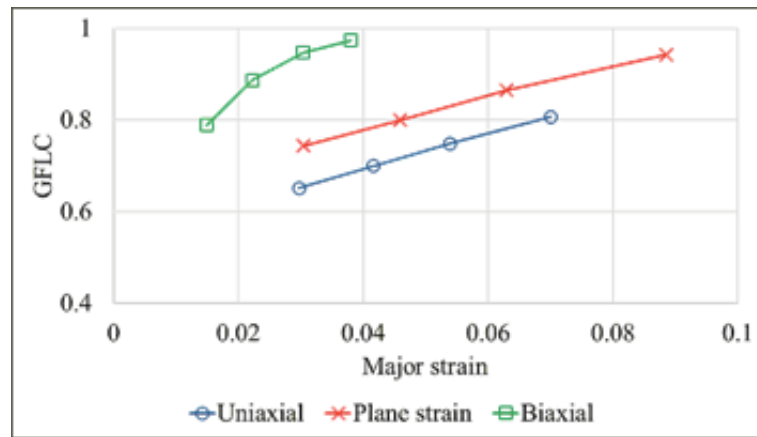
Figure 8.8: Influence of draw depth on formability for test material AA6016
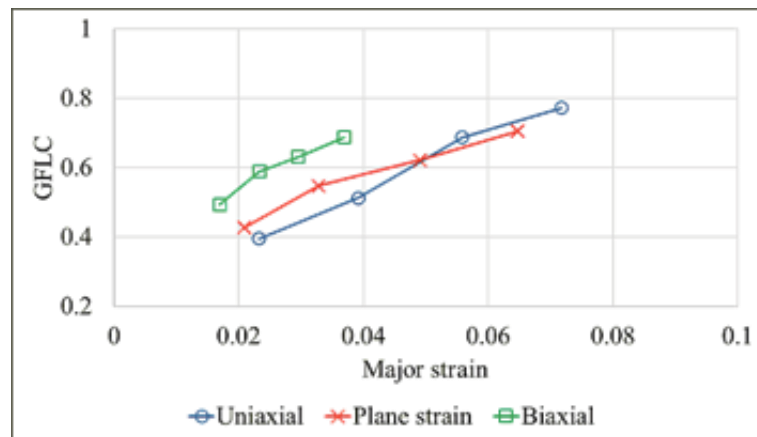
Figure 8.9: Influence of draw depth on formability for test material HX260LAD

GFLC values are shown for each material with respect to the principal major strain. The GFLC behaves in the different deformation states proportional to the major strain as the preforming degree. For the aluminum, the GFLC values obtained after the biaxial preforming are closer to the forming limit than other preforming states. On the other hand, the GFLC value in the

uniaxial state tends to be the lowest. Even if the drawing depths are all the same, the uniaxial preformed part has a higher bead height than the other cases. For the steel, the uniaxial state shows the highest GFLC value. This is different from the aluminum, which is due to the different material behavior. In general, the biaxial state has a high slope. Next, the uniaxial state has an intermediate slope, and finally, the plane strain has a lowest slope. That is, the higher degree of the biaxial preforming lead the bead forming closer to the forming limit. The influences of the bead height and the preforming on GFLC have nearly linear relations.

8.5 Initial bead height function

Every proportional relationship has been adapted to the linear polynomial. The GFLC linear polynomial of the bead height is superimposed on the GFLC linear polynomial of the preforming degree according to the uniaxial, plane and biaxial strain state. The superposed equations are transformed to the bead height function of the preforming degree, respectively, and the GFLC value is set to a constant of 1.0. It is then possible to derive the bead height with the GFLC values of 1.0 depending on the preforming state and degree.

Based on these results, two axes are built in the plane. An axis is the major strain as preforming degree. The other axis forms the ratio of minor strain to the major strain corresponding to the forming state. The bead height, which represents the GFLC value of 1.0, becomes the vertical axis. The maximum deformable bead height is shown as 3D area of the degree of preforming (φ_1^{vor}) and of the forming state ($\frac{\varphi_2^{vor}}{\varphi_1^{vor}}$) in Figure 8.10 for AA6016 and Figure 8.11 for HX260LAD, respectively.
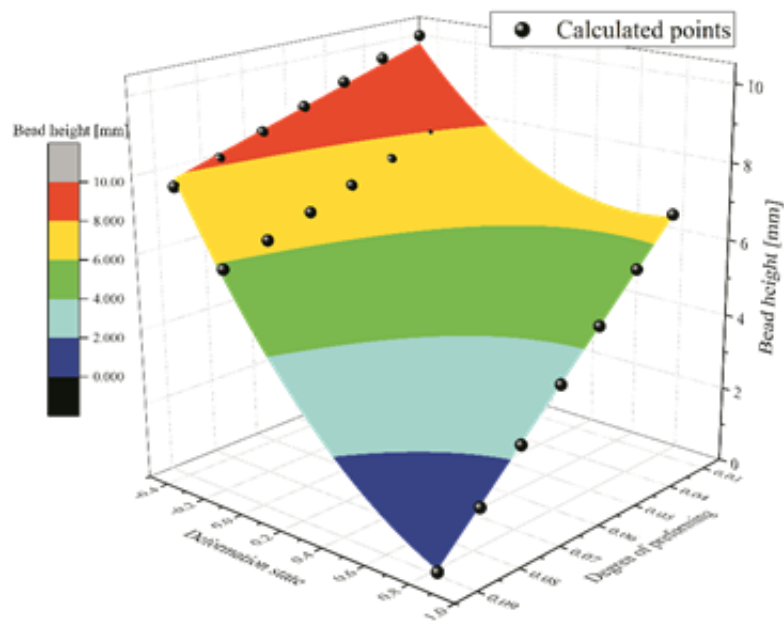
Figure 8.10: Maximum deformable bead height as a 3D surface of the preforming degree (ε_1^{vor}) and the deformation state $(\frac{\varepsilon_2^{vor}}{\varepsilon_1^{vor}})$ for the test materials AA6016
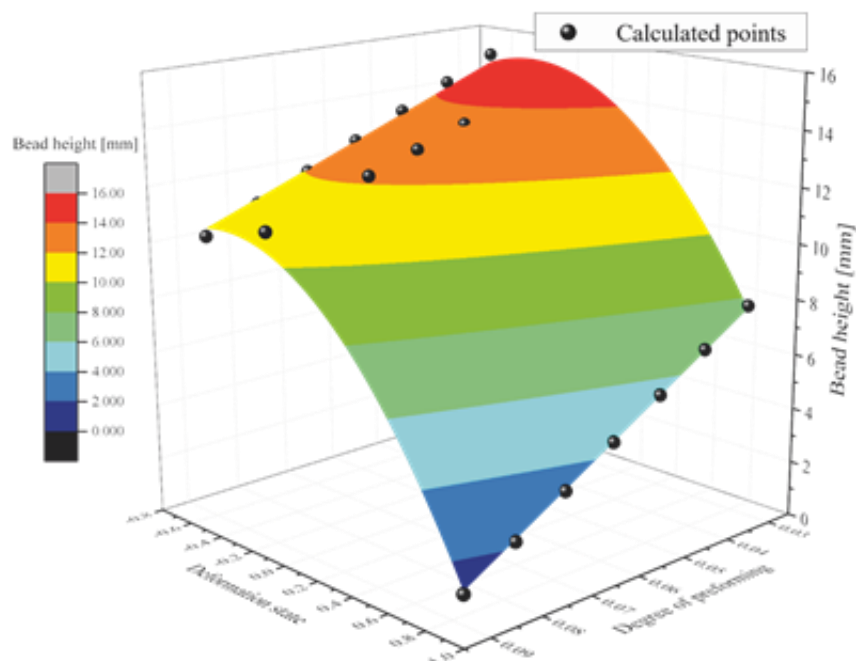
Figure 8.11: Maximum deformable bead height as a 3D surface of the preforming degree (ε_1^{vor}) and the deformation state $(\frac{\varepsilon_2^{vor}}{\varepsilon_1^{vor}})$ for the test materials HX260LAD

The strain distribution of the preformed part in the above 3D surface can determine the deterministic initial bead height near the forming limit. In addition, the 3D surface can only approximate the deformable bead height since each relationship is linearized using the principle of linear superposition. In practice, the determined bead height may have different probabilities of material failure. Therefore, a safety factor (f^{sicher}) is adopted to account for the stochastic influence. The producible bead height, which is 0.9 or 0.8 in the GFLC, can be also determined using the safety factor. The 3D surfaces are adapted to the second polynomial equation. As a result, the maximum producible bead height function of the pre-strains for each material is derived as the following equations:

$$h^{alu}(\varepsilon_1^{vor},\varepsilon_2^{vor}) = 3.14\left(\frac{\varepsilon_2^{vor}}{\varepsilon_1^{vor}}\right)^2 - 59.5(\varepsilon_1^{vor})\left(\frac{\varepsilon_2^{vor}}{\varepsilon_1^{vor}}\right)$$
$$-57.7(\varepsilon_1^{vor}) - 2.33\left(\frac{\varepsilon_2^{vor}}{\varepsilon_1^{vor}}\right) + 10.6(f^{sicher}) - 0.21,$$

Equation 8.1

$$h^{stahl}(\varepsilon_1^{vor},\varepsilon_2^{vor}) = 0.68(\varepsilon_1^{vor})^2 - 5.66\left(\frac{\varepsilon_2^{vor}}{\varepsilon_1^{vor}}\right)^2$$
$$-26.77(\varepsilon_1^{vor})\left(\frac{\varepsilon_2^{vor}}{\varepsilon_1^{vor}}\right) - 74.1(\varepsilon_1^{vor})$$
$$-2.64\left(\frac{\varepsilon_2^{vor}}{\varepsilon_1^{vor}}\right) + 20(f^{sicher}) - 2.71.$$

Equation 8.2

This makes it possible to determine the initial bead height near the forming limit only based on the preform simulation without the exact formability prediction. The determination of the initial bead height reduces greatly the number of iterations in bead optimization using an accurate formability analysis.

The radius and bead width are defined by the design constraint of the user, and the flank angle is determined according to the load case. If the bead path is adjacent, the spacing between the beads may not be closer to the same value as the overburden width. Since the bead height that a parameter has a strong influence on formability and stiffness, it is important to determine the initial height in the optimization procedure.

9 Experimental validation

9.1 Experiment of bead forming

Based on the bead construction, the bead tools were fabricated of die material 1.2312 without tempering, because the bead forming requires no more force than force in the deep drawing and the test materials have no high strength. The lower bead replaces the punch for the preforming in Figure 7.8. The upper bead is assembled on the upper die to perform the bead forming. The entire dies are installed in a hydraulic press DXU320B of Dieffenbacher GmbH & Co. KG to carry out the preforming and the bead forming as shown in Figure 9.1.

Figure 9.1: installed entire tools for preforming and bead forming in hydraulic press

Before manufacturing of parts, the pattern was engraved on a surface of sheets by the electrolytic marking device EU CLASSIC 300 in order to measure strains with ARGUS. The electrolytic fluid with number 76 for the electrolytic marking device was used for two materials. The marking power of the device was set as 16. The manufacturer of the device ÖSTLING GmbH confirmed the setting of the fluid and the marking power.

The preformed and bead-formed parts are manufactured as shown in Figures 9.2 and 9.3, respectively, to perform the validations of strain, material failure and stiffness. The strain comparison validates the accuracy of the FE model and the material model. The location of the material failure at certain bead heights validates the accuracy of the GFLC as forming limit prediction. The load curves are recorded and calculated for the stiffness validation, and then the bead location based on the determined trajectory and the material model are validated.

Figure 9.2: a preformed part for HX260LAD as example
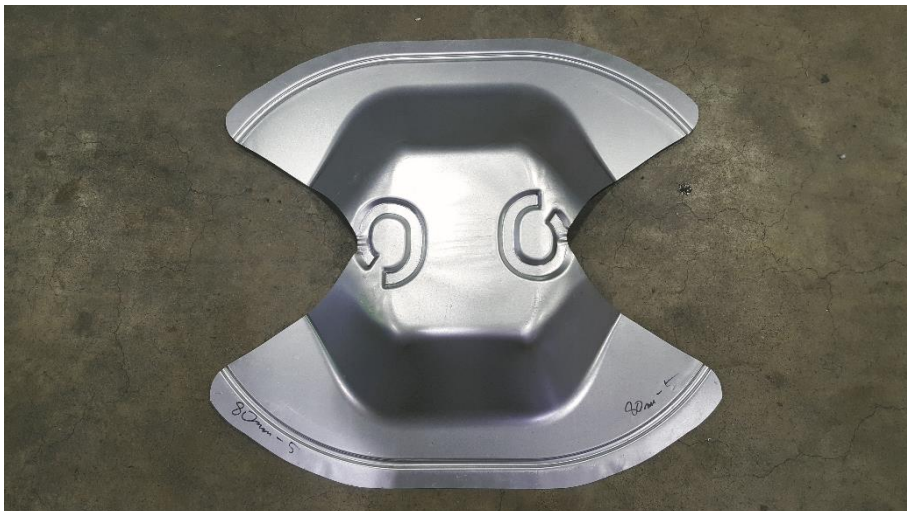
Figure 9.3: a bead-formed part for HC2620LAD as example

9.2   Strain comparison

The measured strain distributions after the preforming and bead forming are compared with simulation results. The strain is calculated using the simulation model described above. The experimental measurements are carried out using the ARGUS optical measuring system. The experimental condition for the preforming was a drawing depth of 70 mm, and the bead forming is carried out with the bead height of 5 mm. The locations of the beads were determined based on the stress distribution generated under the defined load case. Figures 9.4 and 9.5 show the comparison of the logarithmic strains from the simulation and the experiment at various specific locations in according to materials and each forming.

The main and minor strains on the sheet surface after each forming were compared at the determined positions. The average value was calculated from ten data in the range of 5 mm radius per position. The error range was determined based on the maximum and minimum values. Overall, the simulative values in the major strain grade are slightly overestimated compared to the experiment. However, since the simulative values are all within the experimental measurement error range, the simulation model correctly describes the experiment. There was no noticeable difference in the minor strain. Generally, the measurement errors of the experimental values are large because the clarity of the printed pattern for the ARGUS detection is finely degraded by the printability and the lubricant influence. Since the strain distributions of the simulation and the experiment are consistent, it is nevertheless possible to guarantee the reliability of the strain results in the created simulation model. Thus, the strain, which is the input to the GFLC, can be used in the simulation.
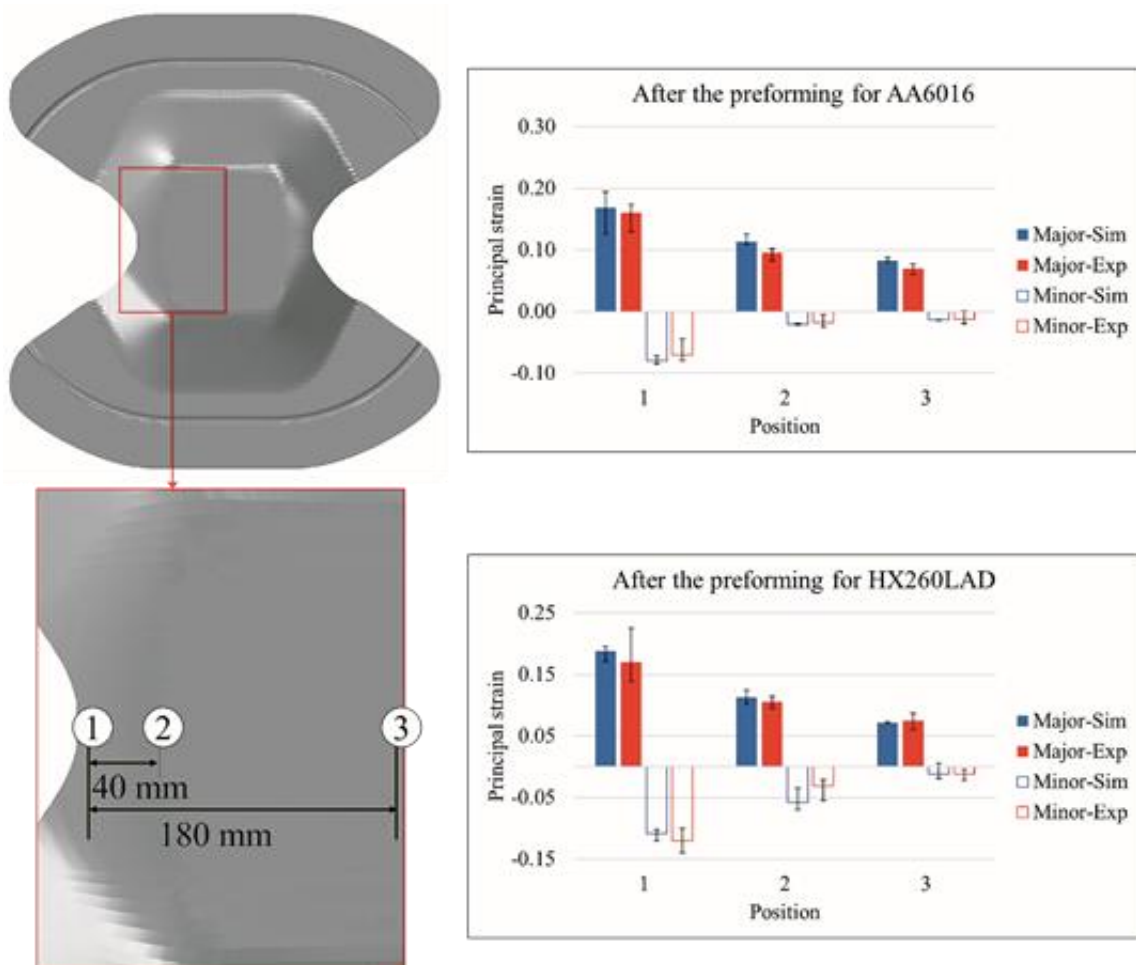
Figure 9.4: Comparison of the strains from the preformed parts between simulation and experiment at defined positions
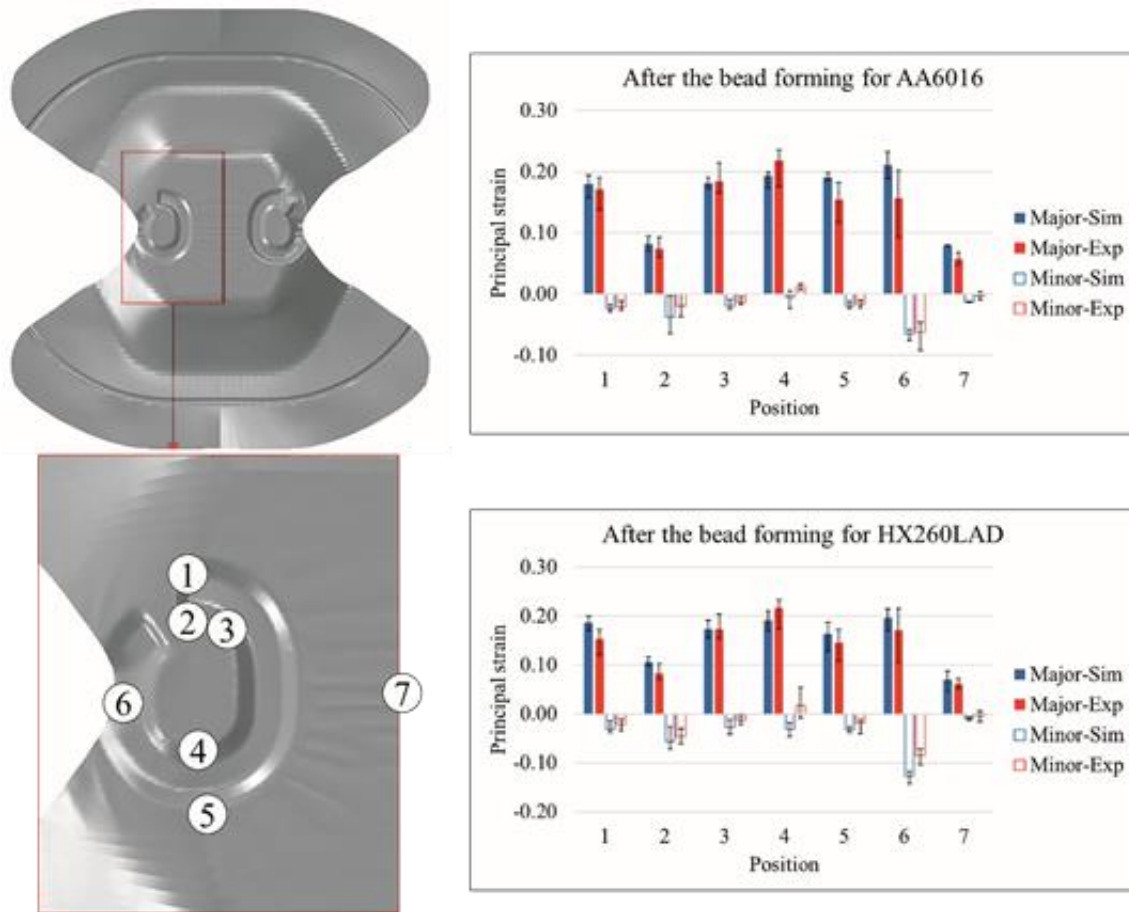
Figure 9.5: Comparison of the strains from the bead-formed parts between simulation and experiment at defined positions

9.3   Formability analysis

The accuracy of the strain calculation in the validated simulation model has been confirmed and the strain from the forming simulation is used as the input value for the GFLC to allow a formability prediction. In order to predict the material failure correctly, the GFLC should also be validated. The state of the bead-formed part is thus compared at the material failure in the simulation and the experiment. Preforming is carried out to a drawing depth of 70 mm for AA6016 and 80 mm for HX260LAD, respectively. The bead height varies depending on the material until the material failure occurs. The material failures were detected after the bead forming. The material failures are compared with the simulation results in Figure 9.6.
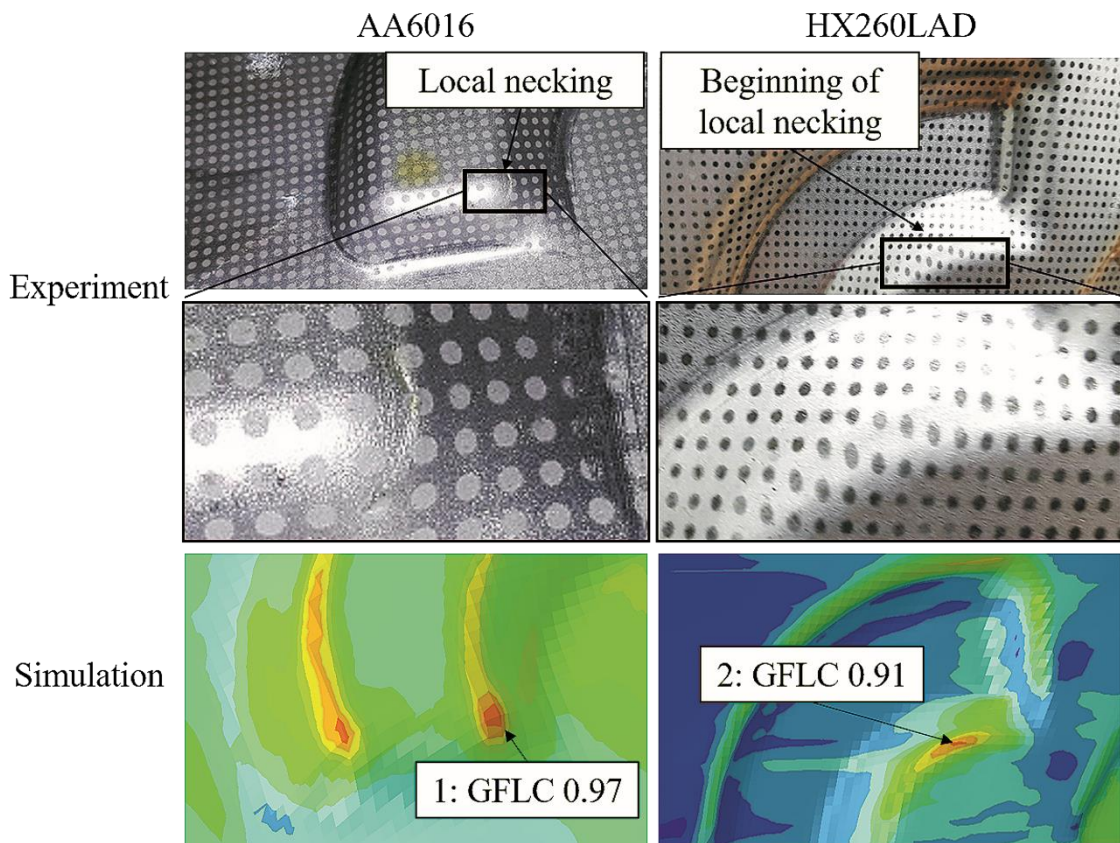
Figure 9.6: Comparable forming limit prediction of GFLC with experimental material failures

In the simulation, it was predicted that local necking would occur in aluminum at a bead height of 7.3 mm near the GFLC of 0.97. In the experiment, it was confirmed that local necking occurs at the same position when the part is formed by the bead height with 7.3 mm as shown in Figure 9.6. The local necking at the corner of the bead geometry appears to be just before the fracture. The shape of the local necking represents a brittle behavior as a thin length of about 5-6 mm.

In the case of steel, bead forming was carried out with a bead height of 9 mm in the preformed sample. It is shown in the experiment of Figure 9.6 that a local necking for HX260LAD begins, since the necking looks ductile deformation and diffuse necking. The failure occurred at the edge of the bead geometry. The position 2 that has the maximal value of the GFLC has good agreement with the experiment. The GFLC with the value of 0.91 is close to the beginning of the local necking in agreement with the experiment.

The necking shape of AA6016 is different from that of HX260LAD due to the different anisotropic material behavior. Two materials have also the different flow curve, but the hardening behavior affects a magnitude of forming load and the ductility has an influence on the bead height. Hence, the higher bead formed the material HX260LAD that has more

elongation from the uniaxial test. The different locations of the necking can be attributed to the material anisotropy. The necking of the AA6016 occurred on the outside and on the upper surface of the bead geometry, and the necking of the HX260LAD was confirmed on the opposite side and on the under radius of the bead geometry. The implemented Yld2000-2d with the non-AFR described the accurate anisotropy of the test materials. Based on that, the GFLC achieved the reliable forming limit. In order to confirm that a nonlinear strain path is shown in a bead forming, the stain path at the failure is shown in Figure 9.7 for AA6016 and 9.8 for HX260LAD, respectively. Furthermore, the GFLC point that is away from the FLC according to the normalized GFLC-value is shown together to know that the GFLC takes the nonlinear strain path into account.

Figure 9.7 shows the strain path at the necking location from the simulation and the GFLC point with the FLC of AA6016. The first point of the strain path from zero means the strains after the preforming. The subsequent points are the recorded strains each time the path direction changed in the bead forming. The strain path by the bead forming shows the nonlinear path. Thus, the nonlinear strain path can be represented in the bead forming.
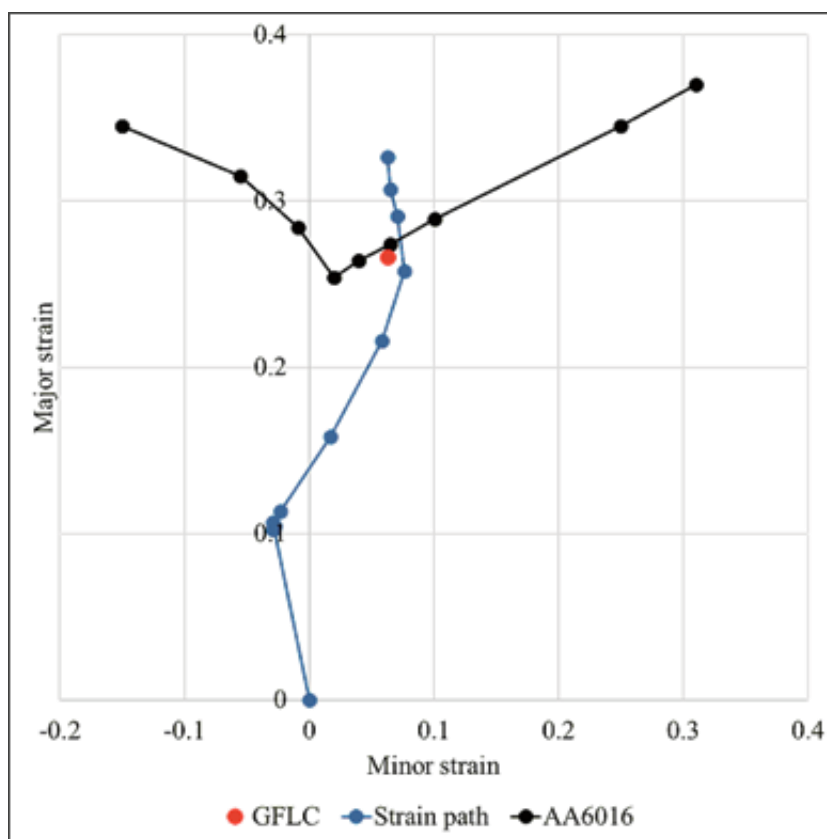
Figure 9.7: Accuracy of the GFLC considering nonlinear strain path for AA6016

The local necking would have already occurred and a crack could be predicted according the end strain of the strain path and the FLC. The conventional FLC needs only strains after end forming not strain path. However, the GFLC takes the strain path as input and analyzed the accurate time of the local necking. The GFLC could analyze that a deeper bead can be formed under these strain paths. Thus, it is confirmed in advance that it is possible to predict a producible bead geometry with a higher stiffness effect.

The major and minor strain after the preforming were calculated 0.106 and -0.029, respectively. The strain ratio of the minor to major strain has -0.27. The derived function for initial bead height in Equation 8.1 can calculate an initial bead height of 6.9 mm. Assuming linear relation, the relative error between the limit bead height of 7.3 mm and the suggested initial bead height of 6.9 mm is 5.4%. The object of the function for initial bead height is that suggestion of an initial bead height by the database will reach 80 % of the optimization step corresponding to forming limit. The initial bead height function as database was also validated by comparison of the suggested initial bead height with the practical limit bead height.

Figure 9.8 shows the strain path at the necking location from the simulation and the GFLC point with the FLC of HX260LAD.
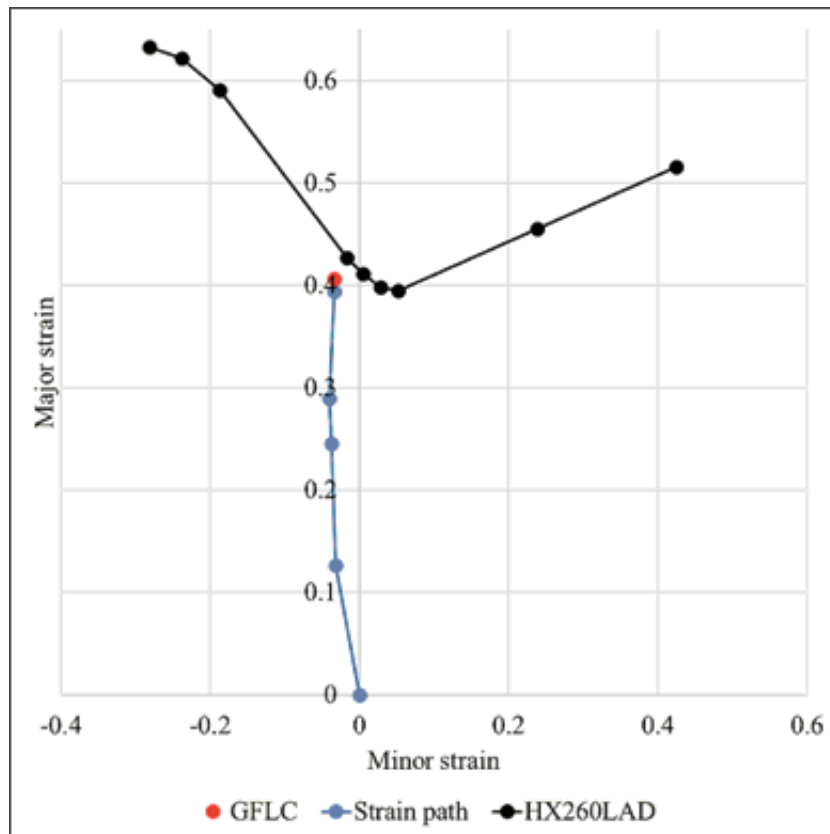
Figure 9.8: Accuracy of the GFLC considering nonlinear strain path for HX260LAD

The strain path in HX260LAD also shows nonlinear path. The direction of the strain is not much changed after the preforming. In addition, the almost linear path in the bead forming is represented. Thus, the analysis of the FLC and the GFLC shows similar the formability predictions. The GFLC calculates a little bit closer to the forming limit than the analysis of the FLC using the end strain of the strain path. This difference is regarded to be a characteristic of GFLC, which predicts formability regardless of strain path.

The major and minor strain after the preforming for HX260LAD are 0.126 and -0.031, respectively. The strain ratio of minor and major strain is -0.246. The derived function in Equation 8.2 calculates an initial bead height of 9.1 mm. The relative error between the limit and the initial bead height suggested from the database is approximately calculated 1.1%. Thus, In the HX260LAD, the suggested initial bead height is offset by 1.1% from the forming limit. For the HX260LAD, the initial bead height was close to the forming limit of 1.1%, so the derived function in Equation 8.2 was also validated.

The comparison of the direct strain at a local area proved difficult because the local necking area was smaller than the minimum distance of the pattern for the optical measurement system ARGUS (GOM). However, it was discovered that the difference between the local necking position and the bead height causing the material failure was small.

Even if the existing data of the GFLC is only scaled by updating the FLC, there is no major error in the formability prediction and the manufacturability could be determined taking the nonlinear strain path into account. This validation guarantees the model of the formability prediction for the bead optimization program and supports the determination of the bead geometry based on a consideration of the manufacturability.

9.4 Stiffness

The forming simulation should be able accurately to calculate not only the manufacturability of the bead geometry, but also the stiffness of the parts. To confirm that, tests for stiffness evaluation are carried out on the parts before and after the bead forming and the force-displacement curves are recorded. The measured load-displacement curves show the validity of the forming simulation compared to the simulation results. A load sensor with a contact area of 20 mm diameter is applied to the center on the upper side of the parts by the universal testing machine (Zwick & Roell, 200 kN) under the previously defined load case. The testing machine has no enough surface to place the part. Thus, one blank as support plate was placed to put the part on it. The part slides on the support plate while receiving the vertical loading on the center of the part. In the defined load case, the blanking holding line of the part was fixed. Four clampers were used in order to avoid slip of the part on the support plate. Each clamper fastens at each corner of the part. The pin loading was carried out with the speed of 6 mm/min. The loading speed under 10 mm/min has no significant change of load curves for the test materials. The test setting is shown in Figure 9.9.

Figure 9.9: Stiffness test for loading on the middle of the part

The stiffness is identified up to the path where the reversible force-displacement curves appear at the same position. If the load-displacement curve irreversibly differs from the previous curve after a repeat test under the same conditions, this is evidence that plastic deformation occurred in the previous experiment. Since the stiffness is effective only in the elastic deformation, the elastic deformation range showing a reversible load-displacement curve is confirmed. As a result, it is confirmed that the elastic deformation is in the stiffness tests up to 7 mm for the aluminum and 4 mm for the steel, respectively.

The simulation for the load-case based on the experiment conditions is carried out to obtain the load curve. Since the simulation was carried out by the dynamic/explicit and the material model was only implemented for the dynamic/explicit method as Abaqus/VUMAT, The load curve has an oscillation. The load oscillation is not physical but is caused by the characteristics of the numerical analysis. The load curve was expressed as the median of the load values calculated using the FFT (Fast Fourier Transform) algorithm in the OriginPro 2017 program (OriginLab Corporation, 2017). The raw simulation and smoothed curve for AA6016 and for HX260LAD are shown in Figure 9.10 and Figure 9.11, respectively.
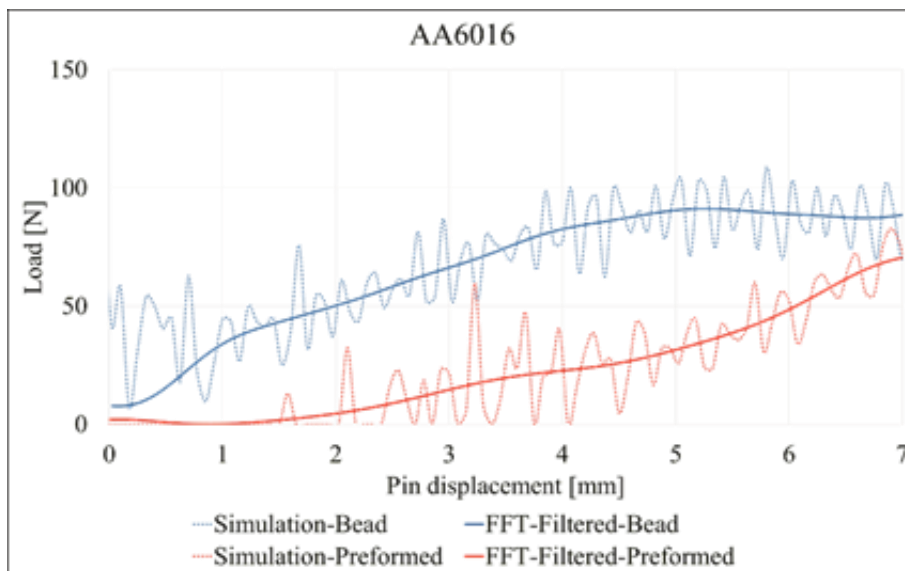
Figure 9.10: the raw and smoothed load-displacement curves in the simulation of the load case test for AA6016
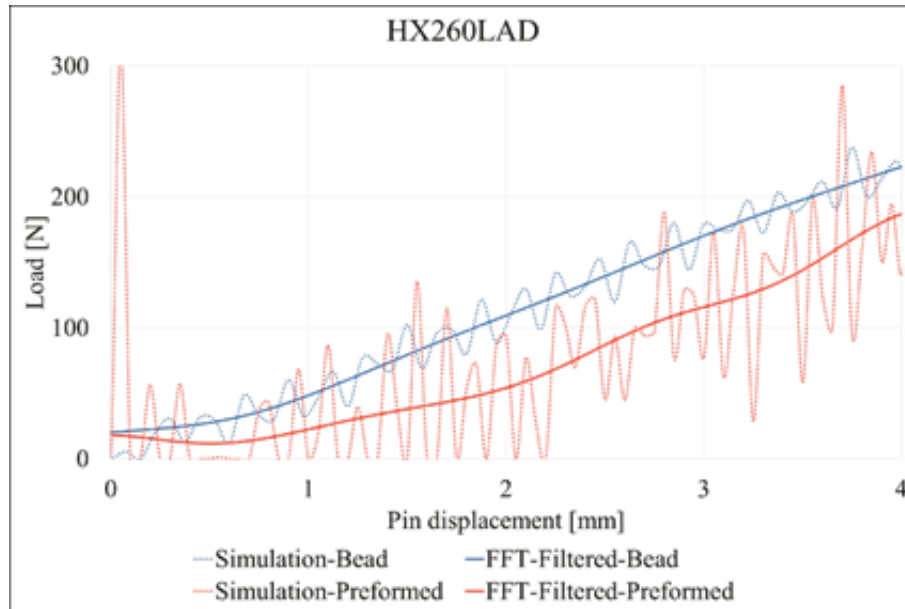
Figure 9.11: the raw and smoothed load-displacement curves in the simulation of the load case test for HX260LAD

In contrast to the simulation, the experimental load curves do not have the oscillation due to the quasi-static loading and condition. The experimental load curves are directly compared with the filtered load curves of the simulation. Figures 9.12 and 9.13 show the comparison according to the material, the preformed and bead-formed parts.
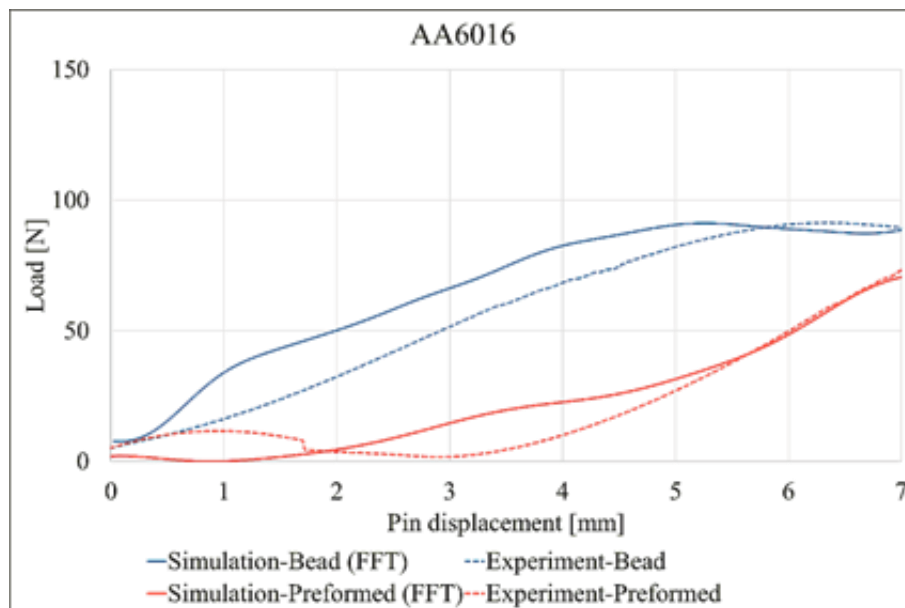
Figure 9.12: the load-displacement curves from the stiffness test for AA6016

The load-displacement curve of the preformed part for AA6016 recorded a small increase up to 1 mm displacement and a decrease of load up to 3 mm displacement. Thereafter, the load increases sharply. The simulation result for the preformed part shows that the load has values

under 10 N from 0 mm to 2 mm displacement. The load increases up to 5 mm displacement and more rapidly after 5 mm displacement. The simulation showed a small difference from the experiment before 4 mm, but the experimental and simulation results were consistent after 5 mm. For this reason, the small difference is shown but the simulation load is comparable with the experiment.

The experiment and the simulation of the bead-formed part for AA6016 show that the load increases up to 6 mm displacement in the load-displacement curve. The both load has stationary curve after 6 mm displacement. The load curve of the simulation for the bead-formed part has more about 5 to 10 N than that of the experiment. The both results are consistent after 6 mm displacement. The difference is also caused by the simulation characteristic and the filter technique like FFT. Nevertheless, the simulation shows a good qualitative load curve.

The load values and the slope of the bead-formed part are absolutely higher than the preformed component. The load slope of the preformed part has similar to that of the bead-formed part after 4 mm displacement. However, the load reduction of the preformed part after 1 mm is regarded as a defect called Oil-Canning. Thus, the determined bead location stiffened the deep drawn part for AA6016 and prevented the defect of the Oil-Canning.
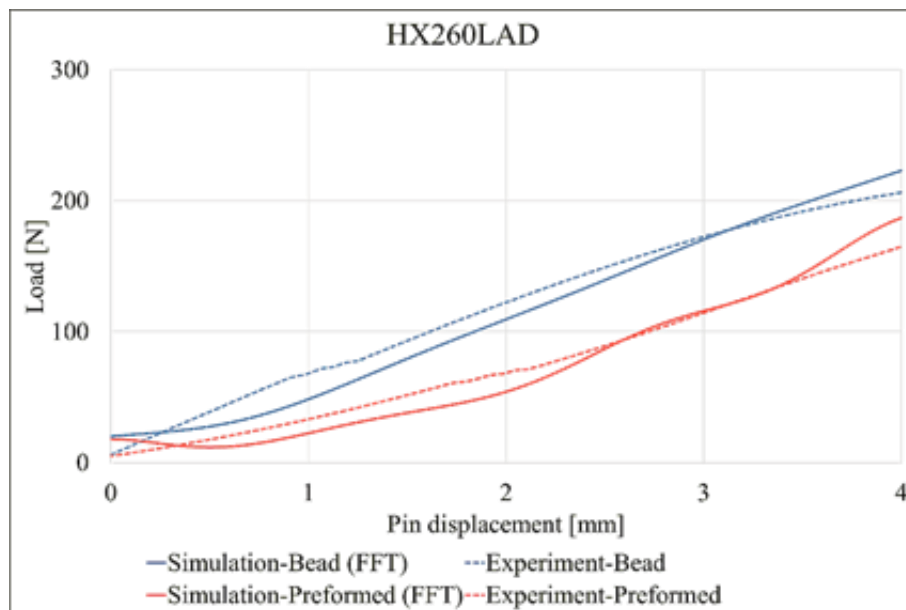
Figure 9.13: the load-displacement curves from the stiffness test for HX260LAD

The load-displacement curve of the preformed part for HX260LAD increased almost linearly. The bead-formed part had also a linear load curve with a higher slope. The simulation results

have a good consistency with the experimental in aspect of quality and quantity, even if the load curves with the vibration were filtered by FFT.

The load slope of the bead-formed part increased about 33 % more than that of the preformed part. The bead location and geometry well stiffened the deep drawn part of HX260LAD, since the stiffness is regarded as the slope of the load-displacement curve. The load values of HX260LAD has more about twice than that of AA6016, because the load difference caused by the stiffness of two materials. The different anisotropy differently and slightly affected the deformation and the stress distribution and caused that the tendencies of the load curve for two materials are different each other. In addition, a similar stiffness effect was observed for both materials because the main locations with high stress distribution were similar, even if the trajectory generated based on the stress distribution of AA6016 in Section 7.3 was applied to HX260LAD.

The stiffening effect was confirmed by the determined bead locations based on direction of major bending stress, and the results of the stiffness simulation are consistent with the experimental test results. Consequently, the stiffness analyzer is validated and can be applied to the bead optimization program.

10   Summary and outlook

As framework of the research, a method was developed for the optimization of cambered sheet metal components taking into account critical production conditions. The goal is to provide a numerical method as a tool, which helps to optimize a virtually constructed component in terms of stiffness and under consideration of manufacturing constraints. For the simplest possible use and the good interfaces, the commercial finite element software Abaqus forms the basis for the method.

To consider the manufacturing conditions in the bead optimization program, the forming limit prediction model GFLC was used. The forming simulation was modeled with the anisotropic material model Yld2000-2d with the non-AFR to obtain the accurate strain history per forming step as an input value for GFLC. The forming simulation was validated for the strain calculation by the measured strain distribution from the experiment. The existing data for the GFLC were adapted to the current experimental materials from the difference in the FLC of the previous material and the current material. The optimal trajectories, which stiffen the component based on direction of the major bending stress, were generated from the stress distribution of the forming simulation. The beading tool with the identified optimization bead position was made which can change the bead height and made the bead formed parts experimentally. Subsequently, the GFLC calculation agreed with the experimental material failure. This makes it possible to account for the manufacturing in the bead optimization program using the forming simulation and the GFLC model. In addition, the stiffness of the components without and with beads was also measured as a force-displacement using a pin loading. The simulative force-displacement curve was consistent with the experiment. From this, the accuracy of the stiffness analysis and the algorithm for determining the optimum bead location was verified.

The forming simulation and GFLC investigated the influence of the preforming on the formability of the bead. Based on this, the maximum producible bead height function of the strain distribution was derived from the preforming. This is a database in the bead optimization process that provides an input value that allows efficient optimization calculation. Moreover, not only a 2 step forming but also a multi-stage forming history can be taken account due to the GFLC that consider any nonlinear loading paths. Sheet metal parts produced by a multi-stage forming can be also stiffened without material failure by the bead optimization.

A bead optimization program, taking the manufacturability into account, was developed by the forming simulation and GFLC. Since the simulative accuracy of each module is also physically verified, it is expected that this optimizer will be able to design the bead efficiently.

In this study, a method was presented to consider the bead formability of sheet metals. The demand for a high stiffness and lightweight structure is still high. As electric or hybrid cars are increasingly trying to take up a large part in the automotive market. There are also problems with a battery packing technology. The battery packing structure by a lithium-ion battery swelling that volume of battery cells expand has to withstand a lot of force, so a composite material of carbon fiber and metal can be used to strengthen it. Thus, a technique of combining the carbon fiber with the bead geometry to increase the maximum stiffness again can be developed. A new consideration for the bead geometries to prevent separation of the two materials will be required. In the bead optimization of new materials, an attempt is made to adapt an additional model that predicts delamination, or to extend the existing model to predict not only metal failure but also delamination in a single model. Finally, the bead optimization can be extended to an optimization program considering composite materials and can overcome limit of the maximum stiffness made of only metal.

11   Appendix

11.1 Identification procedure for parameters of Yld2000-2d

The determination method of the anisotropy parameters for the AFR and the non-AFR of the yield function Yld2000-2d are introduced respectively. In the case of the AFR, the number of anisotropic coefficients is 8 and the equilibrium equation for the value and slope of the yield function is relatively easy to obtain. In the case of a non-AFR, 16 anisotropic coefficients are required by adding a potential function, and it is easy to minimize the error function using the weight according to the number of unknown unknowns.

11.1.1 Identification method for AFR

The six input values from a total of eight input values are the measured yield stresses and Lankford coefficients of 0°, 45° and 90° from the rolling direction in the uniaxial tensile test. The other two are the yield stress and the biaxial anisotropy coefficient of the biaxial tensile stress state. To solve the unknown eight anisotropy coefficients, eight equations are required. The equilibrium equations are expressed as the follows:

$$F_i = |\alpha_1 \gamma_i - \alpha_2 \delta_i|^a + |\alpha_3 \gamma_i + 2\alpha_4 \delta_i|^a$$
$$+|2\alpha_5 \gamma_i + \alpha_6 \delta_i|^a - 2(\bar{\sigma}/\sigma_i)^a = 0, \qquad \text{\textit{Equation 11.1}}$$

$$G_i = q_{x\,i} \frac{\partial \phi_y}{\partial s_{xx}} - q_{y\,i} \frac{\partial \phi_y}{\partial s_{yy}} = 0, \qquad \text{\textit{Equation 11.2}}$$

where

$$\frac{\partial \phi_y}{\partial s_{xx}} = a\{\alpha_1 |\alpha_1 \gamma_i - \alpha_2 \delta_i|^{a-1} \text{sign}(\alpha_1 \gamma_i - \alpha_2 \delta_i)$$
$$+ \alpha_3 |\alpha_3 \gamma_i + 2\alpha_4 \delta_i|^{a-1} \text{sign}(\alpha_3 \gamma_i + 2\alpha_4 \delta_i) \qquad \text{\textit{Equation 11.3a}}$$
$$+ 2\alpha_5 |2\alpha_5 \gamma_i + \alpha_6 \delta_i|^{a-1} \text{sign}(2\alpha_5 \gamma_i + \alpha_6 \delta_i)\},$$

where F_i and G_i as the equilibrium equations satisfies the yield stress σ_0, σ_{90} and σ_b, and the Lankford coefficient r_0, r_{90} and r_b, respectively. The deviatoric stresses are related to the

$$\frac{\partial \phi_y}{\partial s_{yy}} = a\{-\alpha_2 |\alpha_1 \gamma_i - \alpha_2 \delta_i|^{a-1} \text{sign}(\alpha_1 \gamma_i - \alpha_2 \delta_i)$$

$$+ 2\alpha_4 |\alpha_3 \gamma_i + 2\alpha_4 \delta_i|^{a-1} \text{sign}(\alpha_3 \gamma_i + 2\alpha_4 \delta_i)$$

Equation 11.4b

$$+ \alpha_6 |2\alpha_5 \gamma_i + \alpha_6 \delta_i|^{a-1} \text{sign}(2\alpha_5 \gamma + \alpha_6 \delta_i)\},$$

normal stresses with the constants according to the stress state. The relation is shown in the following equations:

$$s_{xx} = \gamma \sigma,$$

Equation 11.4a

$$s_{yy} = \delta \sigma.$$

Equation 11.4b

The values of the constants for the stress relation and the equilibrium equations are represented in Table 11.1.

Table 11.1 the values of constants for the equilibrium equations F_i and G_i

	Index i	γ_i	δ_i	q_{xi}	q_{yi}
0° tension	1	2/3	-1/3	$1 - r_0$	$2 + r_0$
90° tension	2	-1/3	2/3	$2 + r_{90}$	$1 - r_{90}$
Balanced biaxial tension	3	1/3	1/3	$1 + 2r_b$	$2 + r_b$

The equilibrium equations are expressed as the following in order to satisfy the yield stress σ_{45} and the Lankford coefficient r_{45}.

$$F_4 = \left|\frac{\sqrt{k'^2_1 + 4\alpha_7^2}}{2}\right|^a + \left|\frac{3k''_1 - \sqrt{k''^2_2 + 4\alpha_8^2}}{4}\right|^a$$

Equation 11.5

$$+ \left|\frac{3k''_1 + \sqrt{k''^2_2 + 4\alpha_8^2}}{4}\right|^a - 2(\bar{\sigma}/\sigma_{45})^a = 0$$

where

$$k'_1 = \frac{\alpha_1 - \alpha_2}{3}, \qquad\qquad \textit{Equation 11.6a}$$

$$k''_1 = \frac{2\alpha_5 + \alpha_6 + \alpha_3 + 2\alpha_4}{9}, \qquad\qquad \textit{Equation 11.6b}$$

$$k''_2 = \frac{2\alpha_5 + \alpha_6 - \alpha_3 - 2\alpha_4}{3}. \qquad\qquad \textit{Equation 11.6c}$$

$$G_4 = \frac{\partial \phi_y}{\partial \sigma_{xx}} + \frac{\partial \phi_y}{\partial \sigma_{yy}} - \frac{2a(\bar{\sigma}/\sigma_{45})^a}{(1 + r_{45})} = 0, \qquad\qquad \textit{Equation 11.7}$$

where

$$
\begin{aligned}
\frac{\partial \phi''}{\partial \sigma_{xx}} = \frac{a}{2} [&\{|\phi''_1|^{a-1}\mathrm{sign}(\phi''_1) \\
&+ 2|\phi''_2|^{a-1}\mathrm{sign}(\phi''_2)\}\{(1 + \Gamma)L''_{11} \\
&+ (1 - \Gamma)L''_{21}\} \\
&+ \{2|\phi''_1|^{a-1}\mathrm{sign}(\phi''_1) \\
&+ |\phi''_2|^{a-1}\mathrm{sign}(\phi''_2)\}\{(1 - \Gamma)L''_{11} \\
&+ (1 + \Gamma)L''_{21}\}],
\end{aligned}
\qquad \textit{Equation 11.8a}
$$

$$
\begin{aligned}
\frac{\partial \phi''}{\partial \sigma_{yy}} = \frac{a}{2} [&\{|\phi''_1|^{a-1}\mathrm{sign}(\phi''_1) \\
&+ 2|\phi''_2|^{a-1}\mathrm{sign}(\phi''_2)\}\{(1 + \Gamma)L''_{12} \\
&+ (1 - \Gamma)L''_{22}\} \\
&+ \{2|\phi''_1|^{a-1}\mathrm{sign}(\phi''_1) \\
&+ |\phi''_2|^{a-1}\mathrm{sign}(\phi''_2)\}\{(1 - \Gamma)L''_{12} \\
&+ (1 + \Gamma)L''_{22}\}],
\end{aligned}
\qquad \textit{Equation 11.8b}
$$

$$\phi''_1 = \frac{3k''_1 - \sqrt{k''^2_2 + 4\alpha_8^2}}{4} \qquad\qquad \textit{Equation 11.8c}$$

$$\phi''_2 = \frac{3k''_1 + \sqrt{k''^2_2 + 4\alpha^2_8}}{4} \qquad\qquad \textit{Equation 11.8d}$$

$$\Gamma = \frac{k''_2}{\sqrt{k''^2_2 + 4\alpha^2_8}} \qquad\qquad \textit{Equation 11.8e}$$

The components of $\mathbf{L}''$ are already defined in Equation 7.9.

The eight equilibrium equations with the material characteristics obtained from the material tests are solved by the Newton-Raphson method. Subsequently, the anisotropy parameters of Yld2000-2d with the AFR are identified.

11.1.2 Identification method for non-AFR

The parameters of yield and potential functions are optimized, simultaneously. The normalized yield stresses are used in the Yld2000-2d. The directional tensile stresses σ_θ are obtained by the uniaxial tensile test at θ degrees. The corresponding stress tensor can be represented by the following vectors of rank 3 for plane stress case [BARL05].

$$S = \sigma_\theta S_\theta \qquad\qquad \textit{Equation 11.9}$$

where

$$S_\theta = [\cos^2\theta \quad \sin^2\theta \quad \cos\theta \sin\theta]^T \qquad\qquad \textit{Equation 11.10}$$

where θ is 0°, 15°, 30°, 45°, 60°, 75° and 90° considering the non-AFR Yld2000-2d.

The deviatoric stress should be directly given to the model. The Equation 11.9 and 11.10 are changed in the following equations:

$$S = \sigma_\theta S'_\theta, \qquad\qquad \textit{Equation 11.11}$$

where

$$S'_\theta = \left[\left(\cos^2\theta - \frac{1}{3}\right) \quad \left(\sin^2\theta - \frac{1}{3}\right) \quad (\cos\theta \sin\theta)\right]^T. \qquad \textit{Equation 11.12}$$

The directional tensile stresses are normalized with respect to the tensile stress at the rolling direction.

$$\|\sigma_\theta\| = \frac{\sigma_\theta}{\sigma_0} = \frac{1}{\bar{\sigma}(S_\theta)} = \left(\frac{2}{\phi_y(S_\theta)}\right)^{\frac{1}{a}}, \qquad \textit{Equation 11.10}$$

where

$$\bar{\sigma} = \left(\frac{1}{2}\phi_y\right)^{\frac{1}{a}}, \qquad \textit{Equation 11.51}$$

where $\|\sigma_\theta\|$ is the normalized yield stress, ϕ_y is the yield function in the Equation 7.1 and 7.14. For the balanced biaxial tension, the stress is expressed as the follows:

$$S = \sigma_b S_b, \qquad \textit{Equation 11.12}$$

where

$$S_\theta = [1 \quad 1 \quad 0]^T. \qquad \textit{Equation 11.13}$$

The deviatoric biaxial stress is expressed as the follows:

$$S = \sigma_b S_b', \qquad \textit{Equation 11.14}$$

where

$$S_b = \left[\frac{1}{3} \quad \frac{1}{3} \quad 0\right]^T, \qquad \textit{Equation 11.15}$$

The normalized biaxial stress σ_b is

$$\|\sigma_b\| = \frac{\sigma_b}{\sigma_0} = \frac{1}{\bar{\sigma}(S_b)} = \left(\frac{2}{\phi_y(S_b)}\right)^{\frac{1}{a}}. \qquad \textit{Equation 11.16}$$

The theoretical Lankford coefficient r_θ at the directional uniaxial direction is

$$r_\theta = \frac{d\varepsilon_{22}^p}{d\varepsilon_{33}^p}, \qquad \textit{Equation 11.17}$$

where $d\varepsilon_{22}^p$ and $d\varepsilon_{33}^p$ are the increment of the plastic strain in transverse and thickness direction, respectively. $d\varepsilon_{33}^p$ is calculated based on the volume constant during the plastic deformation as the follows:

$$d\varepsilon_{33}^{p} = -\left(d\varepsilon_{11}^{p} + d\varepsilon_{22}^{p}\right). \qquad \textit{Equation 11.18}$$

The calculation of r_θ is changed by the substitution of Equation 11.18 into Equation 11.17:

$$r_\theta = -\frac{d\varepsilon_{22}^{p}}{\left(d\varepsilon_{11}^{p} + d\varepsilon_{22}^{p}\right)}, \qquad \textit{Equation 11.19a}$$

$$r_\theta = -\frac{n_{22}(S_\theta)}{\left(n_{11}(S_\theta) + n_{22}(S_\theta)\right)}, \qquad \textit{Equation 11.19b}$$

where n_{11} and n_{22} are components of the direction vector for the plastic strain increment **n** in Equation 7.29.

For the balanced biaxial tension, the Lankford coefficient is expressed as the follows:

$$r_\theta = \frac{n_{22}(S_b)}{n_{11}(S_\theta)}. \qquad \textit{Equation 11.20}$$

The error function with the experimental and calculated stresses and Lankford coefficients should be minimized. The error function is expressed as the follows:

$$E(\alpha_i, \beta_i) = \sum_p w_p \left(\frac{\|\sigma_p^{cal}\|}{\|\sigma_p^{exp}\|} - 1 \right) + \sum_q w_q \left(\frac{r_q^{cal}}{r_q^{exp}} - 1 \right). \qquad \textit{Equation 11.21}$$

The superscripts *exp* and *cal* indicate experimental and calculated values, respectively. The subscript p is the number of all experimental yield stresses, the subscript q is the number of experimental Lankford coefficients, and w is a weighting factor. The subscripts p and q have eight to identify the parameters α_i and β_i of the non-AFR Yld2000-2d (Barlat et al., 2005).

11.2 Derivation of Yld2000-2d

To implement the stress integration of Yld2000-2d with AFR and non-AFR based on the algorithm CCP, only the first derivation of yield and potential function is required. The effective stress of Yld2000-2d is already defined in Equation 11.11. The derivation of the effective stress to the stress tensor is expressed by the chain rule as follows:

where k (= 1 ~ 3) is the number of the tensor components for the plane stress condition. ϕ_y can be replaced by ϕ_p for non-AFR.

$$\frac{\partial \bar{\sigma}}{\partial \sigma_k} = \left\{2a\bar{\sigma}^{(a-1)}\right\}^{-1}\frac{\partial \phi_y}{\partial \sigma_k}$$

$$= \left\{2a\bar{\sigma}^{(a-1)}\right\}^{-1}\sum_{a}^{2}\sum_{b}^{3}\left(\frac{\partial \phi_y}{\partial X_a'}\frac{\partial X_a'}{\partial \tilde{X}_b'}\frac{\partial \tilde{X}_b'}{\partial \sigma_k} + \frac{\partial \phi_y}{\partial X_a''}\frac{\partial X_a''}{\partial \tilde{X}_b''}\frac{\partial \tilde{X}_b''}{\partial \sigma_k}\right),$$

Equation 11.22

Here,

$$\frac{\partial \phi_y}{\partial X_i'} = \begin{bmatrix} a\{(X_1' - X_2')|X_1' - X_2'|^{(a-1)}\} \\ -a\{(X_1' - X_2')|X_1' - X_2'|^{(a-1)}\} \end{bmatrix};$$

Equation 11.23a

$$\frac{\partial \phi_y}{\partial X_i''} = \begin{bmatrix} a\begin{cases} (2X_2'' + X_1'')|2X_2'' + X_1''|^{(a-1)} \\ +2(2X_1'' + X_2'')|2X_1'' + X_2''|^{(a-1)} \end{cases} \\ a\begin{cases} 2(2X_2'' + X_1'')|2X_2'' + X_1''|^{(a-1)} \\ +(2X_1'' + X_2'')|2X_1'' + X_2''|^{(a-1)} \end{cases} \end{bmatrix},$$

Equation 11.23b

and

$$\frac{\partial X_i'}{\partial \tilde{X}_j'} = \begin{bmatrix} \frac{1}{2}\left(1 + \frac{\tilde{X}_1' - \tilde{X}_2'}{\sqrt{\Delta'}}\right) & \frac{1}{2}\left(1 - \frac{\tilde{X}_1' - \tilde{X}_2'}{\sqrt{\Delta'}}\right) & \frac{\tilde{X}_3'}{\sqrt{\Delta'}} \\ \frac{1}{2}\left(1 - \frac{\tilde{X}_1' - \tilde{X}_2'}{\sqrt{\Delta'}}\right) & \frac{1}{2}\left(1 + \frac{\tilde{X}_1' - \tilde{X}_2'}{\sqrt{\Delta'}}\right) & -\frac{\tilde{X}_3'}{\sqrt{\Delta'}} \end{bmatrix},$$

Equation 11.24a

$$\Delta' = \left(\tilde{X}_1' - \tilde{X}_2'\right)^2 + 4\tilde{X}_3'^2,$$

Equation 11.24b

$$\frac{\partial X_i''}{\partial \tilde{X}_j''} = \begin{bmatrix} \frac{1}{2}\left(1 + \frac{\tilde{X}_1'' - \tilde{X}_2''}{\sqrt{\Delta''}}\right) & \frac{1}{2}\left(1 - \frac{\tilde{X}_1'' - \tilde{X}_2''}{\sqrt{\Delta''}}\right) & \frac{\tilde{X}_3''}{\sqrt{\Delta''}} \\ \frac{1}{2}\left(1 - \frac{\tilde{X}_1'' - \tilde{X}_2''}{\sqrt{\Delta''}}\right) & \frac{1}{2}\left(1 + \frac{\tilde{X}_1'' - \tilde{X}_2''}{\sqrt{\Delta''}}\right) & -\frac{\tilde{X}_3''}{\sqrt{\Delta''}} \end{bmatrix},$$

Equation 11.24c

$$\Delta'' = \left(\tilde{X}_1'' - \tilde{X}_2''\right)^2 + 4\tilde{X}_3''^2,$$

Equation 11.24d

where subscripts 1,2, and 3 are corresponding to subscripts *xx*, *yy*, and *xy* in Equation 7.3 and 7.4.

where $\mathbf{L}'$ and $\mathbf{L}''$ are already explained in Equation 7.8 and 7.9, respectively.

$$\frac{\partial \tilde{X}_i'}{\partial \sigma_j} = \begin{bmatrix} L_{11}' & L_{12}' & 0 \\ L_{21}' & L_{22}' & 0 \\ 0 & 0 & L_{66}' \end{bmatrix}, \qquad \textit{Equation 11.25a}$$

$$\frac{\partial \tilde{X}_i''}{\partial \sigma_j} = \begin{bmatrix} L_{11}'' & L_{12}'' & 0 \\ L_{21}'' & L_{22}'' & 0 \\ 0 & 0 & L_{66}'' \end{bmatrix}, \qquad \textit{Equation 11.25b}$$

11.3 Numerical differentiation

The yield function derivation emerging in Yld2000-2d (11.2) may alternatively be calculated by means of numerical differentiation methods. In (Aretz, 2003) a central, as well as a forward difference scheme, has been presented for this purpose. It was shown that the computing effort of the central difference scheme for 3D stress states is approximately 1.7 times larger in comparison to the forward difference scheme. However, the accuracy of two difference schemes represented no significant differences. Thus, the forward difference scheme can be used to calculate the yield function derivation alternative to the analytical computation of the yield function derivation. It was also indicated in (Aretz, 2003) that the singularities in the analytical expressions of the derivation are easily avoided and that the implementation of anisotropic yield functions can be simplified significantly if numerical differentiation is employed.

The forward difference expressions for the yield function gradient components are as follows:

$$\frac{\partial \phi}{\partial \boldsymbol{\sigma}} \approx \frac{\partial \phi(\boldsymbol{\sigma} + \Delta \boldsymbol{\sigma}) - \partial \phi(\boldsymbol{\sigma})}{\Delta \boldsymbol{\sigma}}, \qquad \textit{Equation 11.22}$$

where the module of $\Delta\boldsymbol{\sigma}$ is $\|\Delta\boldsymbol{\sigma}\| = \Delta\sigma$. It was found that $\Delta\sigma$ of approximately 10^{-5} is reasonable for general metal forming.

A List of figures

B List of tables

C Literatures

Albers, A., Majic, N., Krönauer, B. and Hoffman, H., 2010. Manufacturing aspects in simulation based bead optimization. Conference: 10. Internationales Stuttgarter Symposium "Automobil- und Motorentechnik" in Stuttgart

Altair Computing User's Manual, Version V5.0 (2000)

Aretz, H., 2003. Modellierung des anisotropen Materialverhaltens von Blechen mit Hilfe der Finite-Elemente-Methode [Dissertation]. RWTH Aachen University, Shaker-Verlag (2003), Germany. ISBN 3-8322-1136-5

Armstrong, P.J. and Frederick, C.O., 1966. A mathematical representation of the multiaxial Bauschinger effect. CEGB internal research report in Materials at High temperature. 24(1), P. 1-26

Arrieux, R., 1981. Contribution to the determination of forming limit curves of titanium and aluminum [Dissertation]. Proposal of an intrinsic criterion. INSA, Lyon (in French)

Banabic, D., Balan, T. and Comsa, D.S., 2000. A new yield criterion for orthotropic sheet metals under plane-stress conditions. Proceedings of the 7th Conference 'TPR2000'. Cluj Napoca, Romania. P. 217-224

Banabic, D. and Wagner, S., 2002. Anisotropic behaviour of aluminium alloy sheets. Aluminium **78**, P. 926- 930

Banabic, D., Cazacu, O., Barlat, F., Comsa, D.S., Wagner, S. and Siegert, K., 2002. Recent anisotropic yield criteria for sheet metals. Proceedings of the Romanian Academy. **3**(3), P. 91–9

Banabic, D., Aretz, H., Comsa, D.S. and Paraianu, L., 2005. An improved analytical description of orthotropy in metallic sheets. International Journal of Plasticity. **21**, P. 493- 512

Barlat, F. and Lian, K., 1989. Plastic behavior and stretchability of sheet metals. Part I: A yield function for orthotropic sheets under plane stress conditions. International Journal of Plasticity. **5**(1), P. 51-66

Barlat, F., Brem, J.C., Yoon, J.W., Chung, K., Dick, R.E., Lege, D.J., Pourboghrat, F., Choi, S.-H. and Chu, E., 2003. Plane stress yield function for aluminum alloy sheets — part 1: theory. International Journal of Plasticity. **19**(9), P. 1297-1319

Barlat, F. and others, 2005. Linear transfomation-based anisotropic yield functions. International Journal of Plasticity. **21**, P. 1009-1039

Barlat, F., Yoon, J.W. and Cazacu, O., 2006. On linear transformations of stress tensors for the description of plastic anisotropy. International Journal of Plasticity. **23**, P. 876-896

Belytschko, T., Liu, W.K. and Moran, B., 2000. Nonlinear finite elements for continua and structrues. Chichester: John Wiley & Sons, Ltd.

Bendsøe, M.P. and Kikuchi, N., 1988. Generating optimal topologies in structural design using a homogenization method. Computer Methods in Applied Mechanics and Engineering. **71**, P. 197-224

Bilik, C., Pahr, D.H. and Rammerstorfer, F.G., 2012. A bead laying algorithm for enhancing the stability and dynamic behavior of thin-walled structures. Acta Mechania **223**(8), P. 1621-1631

Bragard, A., Baret, J.C. and Bonnarens, H. 1972. A simplified technique to determine the FLD at onset of necking. Centre for Research in Metallurgy. **33**, P. 53-63

Cardoso, R.P.R. and Yoon, J.W., 2009. Stress integration method for a nonlinear kinematic/isotropic hardening model and its characterization based on polycrystal plasticity. International Journal of Plasticity. **25**, P. 1684-1710.

Cao, J., Yao, H., Karafillis, A. and Boyce, M.C., 2000. Prediction of localized thinning in sheet metal using a general anisotropic yield criterion. **16**, P. 1105-1129

Cha, W.-G., Vogel, S., Bursac, N., Albers, A. and Volk, W., 2016. Determination of the bead geometry considering formability and stiffness effect using generalized forming limit concept (GFLC). Journal of Physics: Conference series **734**, 32077

Cha, W.-G., Müller, S., Bursac, N., Albers, A. and Volk, W., 2017. Influence of process parameters on the formability of bead stamping part using advanced models. Journal of Physics: Conference series **896**, 012005

Cha, W.-G., Müller, S., Albers, A. and Volk, W., 2018. Formability consideration during bead optimisation to stiffen deep drawn parts. Production Engineering. **12**(6), P. 691-702

Chaboche, J.L., 1986. Time-independent constitutive theories for cyclic plasticity. International Journal of Plasticity. **2**(2), P. 149-188

Chen, M.H., Gao, L., Zuo, D.W. and Wang, M., 2007. Application of the forming limit stress diagram to forming limit prediction for the multi-step forming of auto panels. Journal of Materials Processing Technology. **187-188**, P. 173-177

Chen, J., Zhou, X. and Chen, J., 2010. Sheet metal forming limit prediction based on plastic deformation energy. Journal of Materials Processing Technology. **210**(2), P. 315-322

Chung, K., Lee, M.-G., Kim, D., Kim, C., Wenner, M.L. and Barlat, F., 2005. Springback evaluation of automotive sheets based on isotropic-kinematic hardening laws and non-quadratic anisotropic yield functions: Part I: theory and formulation. International Journal of Plasticity. **21**, P. 861-882.

Chung, K., Kim, H. and Lee, C., 2014. Forming limit criterion for ductile anisotropic sheets as a material property and its deformation path insensitivity. Part I: Deformation path insensitive formula based on theoretical models. International Journal of Plasticity. **58**, P. 3-34

Clift, S.E. and others, 1990. Fracture prediction in plastic deformation processes. International Journal of Mechanical Sciences. **32**, P. 1-17

Considère, M., 1885. L'emploi du fer et Lacier Dans Les Constructions. Annales Des Ponts et Chansses. **9**, P. 574-775

Crisfield, M.A., 1991. Nonlinear finite element analysis of solids and structures: Essentials. Chichester: John Wiley & Sonds Ltd. ISBN 0471929565

Dassault System, 2012. Abaqus 6.12 documentation. Providence, RI, USA: Dassault Systèmes Simulia Corp.

Dick, R.E., Yoon, J.W. and Stoughton, T.B., 2016. Path-independent forming limit models for multi-stage forming process. International Journal of Material Forming. **9**(3), P. 327-337

DIN 50125, 2004. Testing of metallic materials – Tensile test pieces. Berlin

DIN EN 573-3, 2009. Aluminium and aluminium alloys – Chemical composition and form of wrought products – Part 3: Chemical composition and form of products. Berlin

DIN EN ISO 6892-1, 2014. Metallic materials – Tensile testing – Part 1: Method of test at room temperature. Berlin

DIN 8584-3, 2003. Manufacturing processes forming under combination of tensile and compressive conditions - Part 3: Deep drawing; Classification, subdivision, terms and definitions. Berlin

DIN EN ISO 12004-1, 2008. Metallic materials – Sheet and strip - Determination of forming-limit curves – Part 1: Measurement and application of forming-limit diagrams in the press shop. Berlin

DIN EN ISO 12004-2, 2008. Metallic materials – Sheet and strip - Determination of forming-limit curves – Part 2: Determination of forming-limit curves in the laboratory. Berlin

DIN EN ISO 16808, 2014. Metallic materials – Sheet and strip – Determination of biaxial stress-strain curve by means of bulge test with optical measuring systems. Berlin

Dietrich, J. and Tschätsch, H., 2013. Praxis der Umformtechnik: Umform- und Zerteilverfahren, Werkzeuge, Maschinen. 11th Edition. Wiesbaden: Springer. ISBN 978-3-658-01995-2

ELG Carbon Fibre Ltd., 2017. Practical Developments in the Use of Recycled Carbon Fibre for Automotive Structures. Birmingham: Global Automotive Lightweight Materials. 25. – 27.04.2017

Emmrich, D., 2005. Development of a FEM based method for the design of bead patterns for channel and support structures under bending load in the design process [Dissertation]. University Karlsruhe. ISSN 1615-8113

EN 10268:2006+A1, 2013. Cold rolled steel flat products with high yield strength for cold forming - Technical delivery conditions.

EN 10346: 2009, 2009. Continuously hot-dip coated steel flat products – Technical delivery conditions

Fritz, A.H. and Schulze, G., 2004. Fertigungstechnik. 6th Edition. Berlin Heidelberg: Springer. ISBN 3-540-00598-6

Goede, M., 2009. Sustainable Production Technologies of Emission reduced Lightweight car concepts (SuperLIGHT-CAR). European Commission. Wolfsburg:Volkswagen AG

Goodwin, G.M., 1968. Application of strain analysis to sheet metal forming problems in the press shop. SAE Technical Paper. **680093**, P. 380-387

Harzheim, L. and Lieven, W., 2007. Panel bead optimization methods and applications [PowerPoint-Presentation]. Berlin: GME Engineering, 23.10.2007

Hashemi, R., Assempour, A. and Abad, E.M.K., 2009. Implementation of the forming limit stress diagram to obtain suitable load path in tube hydroforming considering M–K model. Materials and Design. **30**, P. 3545-3553

Hashemi, R. and Abrinia, K., 2014. Analysis of the extended stress-based forming limit curve considering the effects of strain path and through-thickness normal stress. Materials and Design. **54**, P. 670-677

Hecker, S., 1975. Simple technique for determining forming limit curves. Sheet Metal Industries. 52(11), P. 671-676

Herrmann, F., 1997. Rechnerische Untersuchung von ausgesteiften Karosserieblechen hinsichtlich ihres Steifigkeitsverhaltens und der auftretenden Spannungskonzentration unter Last [Dissertation]. RWTH Aachen, Institut für Kraftfahrwesen, Schriftenreihe Automobiltechnik. **4097**, ISBN 3-925194-40-1.

Heuss, R., Müller, N., van Sintern, W., Starke, A. and Tschiesner, A., 2012. Lightweight, heavy impact: How carbon fiber and other lightweight materials will develop across industries and specifically in automotive. McKinsey & Company.

Hill, R., 1948. A theory of the yielding and plastic flow of anisotropic metals. Proceedings of the Royal Society A. **193**(1033), P. 281-297

Hill, R., 1952. On discontinuous plastic states with special reference to localized necking in thin sheets. Journal of the Mechanics and Physics of Solids. **1**, P. 19-30

Hill, R., 1979. Theoretical plasticity of textured aggregates. Mathematical Proceedings of the Cambridge Philosophical Society. **85**, P. 179-191

Hill, R., 1990. Constitutive modeHing of orthotropic plasticity in sheet metals. Journal of the Mechanics and Physics of Solids **38**(3), P. 405-417

Hora, P., Tong, L. and Reissner, J., 1994. Prediction methods for ductile sheet metal failure using FE-simulation. In: Proceeding of the IDDRG Congress, Porto, P. 363-375

Hora, P., Tong, L. and Reissner, J., 2003. Mathematical prediction of FLC using macroscopic instability criteria combined with micro structural crack propagation models. In: Proceeding of Plasticity'03 Conference, Quebec, Canada, P. 364-366

Hosford, W.F., 1972. A generalized isotropic yield criterion. Journal of Applied Mechanics. **39**(2), P. 607-609

Hutchinson, J.W. and Neale, K.W., 1978. Sheet necking-II. In: Time-Independent behavior. In: Koistinen, D., Wang, N.-M. (Eds.), Mechanics of sheet metal forming, Bosten: Springer. P. 127-153. ISBN 978-1-4613-2882-7

Jaamialahmadi, A. and Kadkhodayan, M., 2012. A Modified Storen-Rice Bifurcation Analysis of Sheet Metal Forming Limit Diagrams. Journal of Applied Mechanics. **79**(6), P. 061004

Jocham, D., Gaber, C., Böttcher, O., Wiedemann, P. and Volk, W., 2017. Experimental prediction of sheet metal formability of AW-5754 for nonlinear strain paths by using a cruciform specimen and a blank holder with adjustable draw beads on a sheet metal testing machine. International Journal of Material Forming. **10**(4), P. 597-605

Keeler, S.P., 1961. Plastic instability and fracture in sheets stretched over right punches [Dissertation]. Massachusetts Institute of Technology. Boston

Kolasangiani, K., Shariati, M. and Farhangdoost, K., 2015. Prediction of forming limit curves (FLD, MSFLD and FLSD) and necking time for SS304L sheet using finite element method and ductile fracture criteria. Journal of Computational and Applied Research in Mechanical Engineering. **4**(2), P. 121-132

Krönauer, B., Marjic, N., Golle, M., Hoffmann, H. and Albers, A., 2010. Automated bead design considering production constraints. AIP Conference Proceedings **1252**, P. 1247-1255

Lankford, W.I., Snyder, S.C. and Bauscher, J.A. 1950. New criteria for predicting the press performance of deep-drawing sheets. Transaction ASM. **42**, P. 1196-1232

Leiva, J.P., 2011. Structural optimization methods and techniques to design efficient car bodies. International Automotive Body Congress. Michigan, USA, P. 41-55

Levy, B.S. and Van Tyne, C.J., 2016. An approach to predicting the forming limit stress components frommechanical properties. Journal of Materials Processing Technology. **229**, P. 758-768

Lubarda, V.A., 2000. Elastoplasticity theory. CRC Press. ISBN 0-8493-1138-1

Luo, J.H. and Gea, H.C., 1998. Optimal bead orientation of 3D shell/plate structures. Finite Elements in Analysis and Design. **31**(1), P. 55-71

Majić, N., Albers, A., Kalmbach, M. and Clausen, P.M., 2013. Development and statistical evaluation of manufacturing-oriented bead patterns. Advances in Engineering Software. **57**, P. 40-47

Majić, N., 2014. Development of a FEM-based method for the design of production-oriented bead patterns for bending loaded support structures [Dissertation]. Karlsruhe Institute of Technology. ISSN 1615-8113

Marciniak, Z. and Kuckzynski, K., 1967. Limit strains in the process of stretch-forming sheet metal. International Journal of Mechanical Sciences. **9**(9), P. 609-620

Maressa, A., Pluymers, B., Donders, S. and Desmet, W., 2010. NVH optimization methodologies based on bead modification analysis in vehicle body design. Proceeding of ISMA2010. Leuven, Belgium, 20.-22.9.2010, P. 4319-4336

Min, H.E., Fuguo, L.I. and Zhigang, W., 2011. Forming limit stress diagram prediction of aluminum alloy 5052 based on GTN model parameters determined by In Situ tensile test. Chinese Journal of Aeronautics. **24**, P. 378-386

Nakazima, K. and Kikuma, T. 1967. Forming limits under biaxial stretching of sheet metals. Testu-to Hagane **53**, P. 455-458 (in Japanese)

OriginLab Corpoation, 2017. OriginPro 2017G SR1. Northampton, MA, USA: OriginLab Corporation. Available under http://www.OriginLab.com

Ortiz, M. and Simo, J.C., 1986. An analysis of a new class of integration algorithms for elastoplastic constitutive relations. International Journal for Numerical Methods in Engineering. **23**, P. 353-366

Panich, S., Barlat, F., Uthaisangsuk, V., Suranuntchai, S. and Jirathearanat, S., 2013. Experimental and theoretical formability analysis using strain and stress based forming limit diagram for advanced high strength steels. Materials and Design. **51**, P. 756-766

Park, T. and Chung, K., 2012. Non-associated flow rule with symmetric stiffness modulus for isotropic-kinematic hardening and its application for earing in circular cup drawing. International Journal of Solids and Structures. **49**, P. 3582-3593.

Prager, W., 1956. A new method of analyzing stresses and strains in work-hardening plastic solids. Journal of Applied Mechanics. **23**, P. 493-496

Reddy, J.N., 1993. An introduction to the finite element method. 2nd Edition. Boston: McGraw-Hill

Safaei, M., Yoon, J.W. and Waele, W.D., 2014. Study on the definition of equivalent plastic strain under non-associated flow rule for finite element formulation. International Journal of Plasticity. **58**, P. 219-238

Safaei, M., Yoon, J.W. and Waele, W.D., 2015. Evaluation of stress integration algorithms for elastic–plastic constitutive models based on associated and non-associated flow rules. Computer Methods in Applied Mechanics and Engineering. **295**(1), P. 414-445

Schmidt, W. and Puri, W., 2000. Systematische Entwicklung Gewichtsoptimierter Bauteile. 11. SYMPOSIUM „DESIGN FOR X. Schnaittach, 12. and 13. October 2000.

Schuler GmbH: Handbuch der Umformtechnik, Springer Verlag, 1996

Schwarz, D., 2002. Auslegung von Blechen mit Sicken (Sickenatlas). FAT-Schriftenreihe. **168**. ISSN 0933-050 X

Simo, J.C. and Hughes, T.J.R., 1998. Computational Inelasticity. New York: Springer-Verlag. ISBN 0-387-97520-9

Stören, S. and Rice, J.R., 1975. Localized necking in thin sheets. Journal of the Mechanics and Physics of Solids. **23**(6), P. 421-441

Swift, H.W., 1952. Plastic instability under plane stress. Journal of the Mechanics and Physics of Solids. **1**(1), P. 1-18

Stoughton, T.B., 2000. A general forming limit criterion for sheet metal forming. International Journal of Mechanical Sciences. **42**(1), P. 1-27

Stoughton, T.B., 2002. A non-associated flow rule for sheet metal forming. International Journal of Plasticity. **18**, P. 687-714.

Stoughton, T.B. and Yoon, J.W., 2004. A pressure-sensitive yield criterion under a non-associated flow rule for sheet metal forming. International Journal of Plasticity. **20**, P.705-731.

Stoughton, T.B. and Zhu, X., 2004. Review of theoretical models of the strain-based FLD and their relevance to the stress-based FLD. International Journal of Plasticity. **20**(8), P. 1463-1486

Stoughton, T.B. and Yoon, J.W., 2009. Anisotropic hardening and non-associated flow in proportional loading of sheet metals. International Journal of Plasticity. **25**, P. 1777-1817

Stoughton, T.B. and Yoon, J.W., 2012. Path independent forming limits in strain and stress spaces. International Journal of Solids and Structures. **49**, P. 3616-3625

Taylor, G.I. and Quinney, H., 1931. The plastic distortion of metals. Proceedings of the Royal Society: London A. **230**(1931), P. 323-362

Tresca, H. 1864. On the yield of solids at high pressures. Comptes Rendus Academie des Seiences. **59**, P. 754 (in French)

Volk W., Heinle I. and Grass, H., 2011. Accurate determination of plastic yield curves and approximation point for the plastic yield locus with the bulge test. Aachen: ICTP 2011 Proceedings, P. 799-804, ISBN 978-351400784-0

Volk, W. and Hora, P., 2011. New algorithm for a robust user-independent evaluation of beginning instability for the experimental FLC determination. International Journal of Material Forming. **4**(3), P. 339-346

Volk, W. and others, 2012. Failure prediction for nonlinear strain paths in sheet metal forming. CIRP Annals – Manufacturing Technology. **61**, P. 259-262

Volk, W. and Suh, J., 2013. Prediction of formability for nonlinear deformation history using generalized forming limit concept (GFLC). AIP Conference Proceedings. **1567**(1), P. 556-561. DOI:10.1063/1.4850035

Von Mises, R., 1913. Mechanics of solid bodies in the plastically-deformable state. Göttinger Nachrichten Mathematical Physics. **4**, P. 582-892 (in German)

Weinschenk, A. and Volk, W. 2017. FEA-based Development of a new tool for systematic experimental validation of nonlinear strain paths and design of test specimens. AIP Conference Proceedings **1896**, P. 020009

Werber, A., Liewald, M., Nester, W., Grünbaum, M., Wiegand, K., Simon, J., Timm, J. and Hotz, W., 2013. Assessment of forming limit stress curves as failure criterion for non-proportional forming processes. Production Engineering **7**, P. 213-221. DOI 10.1007/s11740-013-0446-6

Yang, R.J., Chen, C.J. and Lee, C.H. 1996. Bead pattern optimization. Structural Optimization. **12**, P. 217-221

Yoon, J.W. and others, 2004. Plane stress yield function for aluminum alloy sheets—part II: FE formulation and its implementation. International Journal of Plasticity. **20**, P. 495-522

Yoon, J.W., Stoughton, T.B. and Dick, R.E., 2007. Earing prediction in cup drawing based on non-associated flow rule. AIP Conference Proceedings. **908**, P. 685-690

Yoshida, K., Kuwabara, T. and Kuroda, M., 2005. Forming Limit Stresses of Sheet Metal under Proportional and Combined Loadings. AIP Conference Proceedings **778**, P. 478-483

Yoshida, K., Kuwabara, T. and Kuroda, M., 2007. Path-Dependence of the Forming Limit Stresses in a sheet metal. International Journal of Plasticity. **23**(3), P. 361-384

Yoshida, K. and Kuroda, M., 2012. Comparison of bifurcation and imperfection analyses of localized necking in rate-independent polycrystalline sheets. International Journal of Solids and Structures. **49**(15), P. 2073-2084

Yoshida, F. and Uemori, T., 2002. A model of large-strain cyclic plasticity describing the Bauschinger effect and workhardening stagnation. International Journal of Plasticity. **18**, P. 661-686

Zeng, D. and others, 2008. A Path Independent Forming Limit Criterion for Sheet Metal Forming Simulations. SAE International Journal of Materials and Manufacturing. **1**, P. 809-817

Ziegler, H., 1959. A modification of Prager's hardening rule. Quarterly of Applied Mechanics. **17**, P. 55-65

Zienkiewicz, O.C., Taylor, R.L. and Fox, D.D., 2014. The finite element method for solid & structural mechanics. 7. Edition. Elsevier. ISBN 978-1-85617-634-7